Physics – Uspekhi **62** (11) 1063 – 1095 (2019)

REVIEWS OF TOPICAL PROBLEMS PACS numbers: **07.85. – m**, **41.50. + h**, 42.79.Dj, **42.88. + h**, 61.05.cp, 78.20.Bh, 78.67.Pt, 95.55.Ka

Multilayer X-ray interference structures

V V Lider

DOI: https://doi.org/10.3367/UFNe.2018.10.038439

Contents

1. Introduction **1063**
2. General information. Regularities and problems **1064**
3. Choice of materials for multilayer interference structures (MISs) **1065**
3.1 Two-component MISs; 3.2 Three-component MISs
4. Calculation of MIS parameters **1069**
5. MIS deposition methods **1070**
6. MIS investigation methods **1070**
7. MIS improvement methods **1071**
7.1 Methods for reducing mutual diffusion; 7.2 Methods for reducing interface roughness; 7.3 Methods for reducing stress; 7.4 Methods for increasing the radiative, temporal, and corrosion stability
8. Methods providing spectral purity **1076**
9. Applications of periodic MISs **1077**
9.1 Monochromators; 9.2 Focusing; 9.3 Normal-incidence optical instruments; 9.4 Polarization properties
10. Aperiodic MISs **1080**
10.1 Depth-gradient MISs; 10.2 Lateral-gradient MISs; 10.3 γ-gradient MISs
11. Narrowband multilayer optical devices **1083**
12. Multilayer reflection diffraction gratings (MDGs) **1083**
12.1 Lamellar MDGs; 12.2 Profiled MDGs; 12.3 Truncated MDGs; 12.4 Phase MDGs; 12.5 Alternative MDG; 12.6 Spectral purity function MDG
13. Multilayer transmission diffraction gratings **1088**
13.1 Multilayer Fresnel zone plate; 13.2 Multilayer Laue lens
14. Conclusions and outlook **1090**
References **1090**

Abstract. Functional principles, current status, and problems of multilayer X-ray optics are reviewed. Methods to optimize planar multilayer interference structures and multilayer diffraction gratings and their application in academic research and technology are discussed.

Keywords: multilayer systems, diffraction gratings, X-rays, X-ray optics, diffraction, interference, spectral resolution

1. Introduction

Progress in modern science is based to a great extent on the observation and manipulation of matter at the molecular or atomic scale. This requires probing tools with the appropriate spatial, energy, and time resolution. The term 'X-ray radiation' is applied at present to a broad spectral range of electromagnetic waves from 0.01 to 120 nm. According to the generally accepted terminology, although somewhat conventionally, this range includes the hard X-ray (0.01–0.3 nm), soft X-ray (0.3–10 nm), and extreme UV (EUV, 10–120 nm) ranges.

In the hard X-ray region, the reflection or diffraction of X-rays is performed from single crystals using the constructive interference of waves reflected from the planes of a crystal lattice (Bragg reflection). For soft X-rays and the extreme UV range, the interplane distances d of most crystals used are too small to satisfy the constructive interference criterion determined by Bragg's law $2d\sin\theta = m\lambda$ (where λ is the radiation wavelength, θ is the Bragg angle, and m is the reflection order). This restriction can be removed by producing a stack of thin alternating layers of materials with the stack periodicity (or the d interval) equal to the parameter d in Bragg's formula.

The waves reflected from all the interfaces of alternating layers of two materials with a high contrast between their optical indices are added constructively, resulting in a high reflection coefficient. A multilayer interference structure (MIS) obtained in this way can be treated as an artificial crystal reflecting radiation like crystals. A great advantage of these 'synthetic' multilayer systems is that the layer thickness

V V Lider Federal Scientific Research Center
"Crystallography and Photonics," Russian Academy of Sciences,
Shubnikov Institute for Crystallography,
Leninskii prosp. 59, 119333 Moscow, Russian Federation
E-mail: lider@ns.crys.ras.ru, vallider@yandex.ru

Received 12 July 2018, revised 24 September 2018
Uspekhi Fizicheskikh Nauk **189** (11) 1137 – 1171 (2019)
DOI: https://doi.org/10.3367/UFNr.2018.10.038439
Translated by M Sapozhnikov; edited by A M Semikhatov

and therefore the periodicity can be readily tuned to the wavelength that must be reflected at a certain angle [1].

Problems with MIS physics and the interfaces of layers, methods for deposition and diagnostics of such structures, and their applications were discussed in detail in monographs [2, 3] and reviews [4–14].

Due to the combination of a number of unique properties, MISs (which are sometimes called multilayer mirrors) are universal elements of modern X-ray optics. The flexibility of MIS properties, the availability and universality of their manufacturing technology, and the possibility of obtaining high X-ray optical parameters of mirrors are attracting increasing interest in their practical applications as dispersion and reflection elements for X-ray spectroscopy problems and diffraction measurements, elemental fluorescent analysis, X-ray plasma diagnostics, X-ray microscopy, astronomy, EUV lithography for microelectronics, and biomedicine [2–4, 7, 12, 13, 15, 16].

The aim of this review is to describe the structural features, the main properties, and possibilities of using multilayer synthetic structures for fundamental studies and developments in the field of high technologies.

2. General information. Regularities and problems

Standard mirrors are of little use for X-ray radiation. In the case of nearly normal incidence ($\theta \approx 90°$), the intensity ratio for reflected and incident radiation is

$$\frac{I}{I_0} = \frac{\delta^2 + \beta^2}{4} . \tag{1}$$

The parameters δ and β determining the refractive index $n = 1 - \delta + i\beta$ are described by the expressions [17]

$$\delta = \frac{\rho\lambda^2 r_e N_A Z}{2\pi A} , \tag{2}$$

$$\beta = \frac{\mu\lambda}{4\pi} , \tag{3}$$

where δ is the refractive index decrement, λ is the radiation wavelength, N_A is the Avogadro number, r_e is the classical electron radius, ρ is the matter density, Z and A are respectively the order number and atomic weight of a sample material, and μ is the linear absorption coefficient. Because the values of δ and β are small (from 10^{-3} in the EUV region to 10^{-6} in the hard X-ray region [1]), the reflection of X-rays is extremely weak.

The situation drastically changes in the case of an MIS consisting of alternating layers of materials with contrast optical parameters of absorbers A, usually with a high absorption, and separating layers (spacers) B with a low absorption (Fig. 1). We note that the separation of layers into absorbing and separating is somewhat conventional because all of them are involved in producing interference reflection. Due to interference of the incident and reflected waves, a standing wave is produced in the MIS with the modulation amplitude of the permittivity [18]

$$B_m = \frac{2(\varepsilon_A - \varepsilon_B)\sin(\pi m\gamma)}{\pi m\gamma} . \tag{4}$$

Here, m is the reflection order, $\gamma = d_A/(d_A + d_B) = d_A/d$, and d_A and d_B are the thicknesses of layers A and B. The

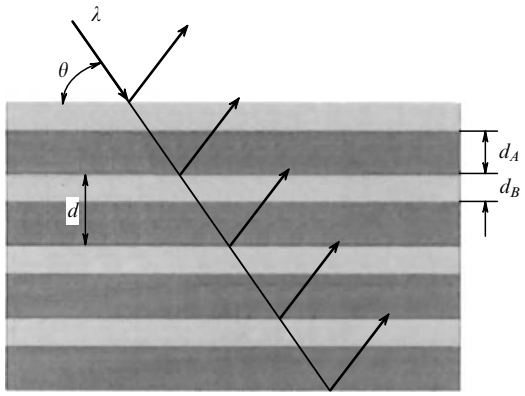

Figure 1. MIS structure. d_A and d_B are the respective absorber and spacer layer thicknesses, d is the bilayer period, θ is the Bragg angle and λ is the X-ray wavelength.

permittivity ε is related to the polarizability χ of a material and the refractive index b as $\varepsilon = 1 - \chi = n^2$ and $\chi = 2(\delta + i\beta)$, i.e., it has real (Re) and imaginary (Im) parts ($\chi = \mathrm{Re}\chi + \mathrm{Im}\chi$), the latter corresponding to the absorption of X-rays in the medium.

Thus, the reflection structure is modulated by the function $\sin(\pi m\gamma)$, which means that the factor γ determines the relative peak reflectivity and, in particular, suppresses diffraction peaks with $m = \gamma^{-1}$. For $\gamma = 0.5$, for example, the even Bragg peaks are suppressed, whereas the odd peaks are amplified: multilayer structures with $\gamma = 0.5$ are called quarter-wavelength, because each layer covers exactly $\lambda/4$ of the incident wave.

Periodic X-ray MISs are characterized by their reflectivity or the reflection coefficient at the maximum of the diffraction reflection curve R and by the curve width $\Delta\lambda$. The latter determines the transmission band width $\Delta\lambda/\lambda$ or its reciprocal value $\lambda/\Delta\lambda$, called the spectral resolving power. The transmission band is determined by the number N of bilayers involved in the formation of the diffracted beam [19]:

$$\frac{\Delta\lambda}{\lambda} = \frac{1}{mN} . \tag{5}$$

With the refraction of X-rays taken into account, Bragg's law is modified to [1]

$$m\lambda = 2d\sin\theta\left(1 - \frac{2\delta_{\mathrm{eff}}}{\sin^2\theta}\right)^{1/2} . \tag{6}$$

Here, $\delta_{\mathrm{eff}} = \gamma\delta_A + (1 - \gamma)\delta_B$ is the mean real part of the refractive index decrement. If Bragg's condition is satisfied, the peak value of the reflection coefficient and the spectral resolving power of the MIS for $m = 1$ are given by the expressions [3, 18, 20]

$$R = \frac{1 - w}{1 + w} ,$$

$$w = \left(\frac{1 - C^2y^2}{1 + C^2y^2\left(\mathrm{Re}\,\Delta\chi/\mathrm{Im}\,\Delta\chi\right)^2}\right)^{1/2} , \tag{7}$$

where $y = \sin(\pi\gamma)/\pi[\gamma + \mathrm{Im}\,\chi_B/\mathrm{Im}\,\Delta\chi]$, $\Delta\chi = \chi_A - \chi_B$, and $C = 1$ and $C = \cos(2\theta)$ for the respective p(π) and s(σ) polarizations of X-rays.

A problem inherent in soft X-ray and EUV regions is that all useful materials absorb radiation to some extent. For this

reason, quarter-wavelength MISs are rarely used as optical elements. The absorber thickness in quarter-wavelength structures is so large that the absorption of X-rays is often too large to obtain a high reflectivity. Because absorption in a thin strongly absorbing material can be insignificant if it is located at a node of the field of a standing wave, the influence of absorption on the MIS reflectivity can be minimized by decreasing the absorber thickness ($\gamma < 0.5$). In this case, the optimal value of the parameter γ^* is found by equating the derivative $\partial y/\partial\gamma$ to zero and is given by [3, 18, 21]

$$\tan(\pi\gamma^*) = \pi\left(\gamma^* + \frac{\operatorname{Im}\chi_B}{\operatorname{Im}\Delta\chi}\right). \tag{8}$$

Then the maximum reflectivity $R_{\max}$ is described by the expression

$$R_{\max} = \frac{1-w^*}{1+w^*},$$
$$w^* = \left(\frac{1 - C^2\cos^2(\pi\gamma^*)}{1 + C^2\cos^2(\pi\gamma^*)(\operatorname{Re}\Delta\chi/\operatorname{Im}\Delta\chi)^2}\right)^{1/2}. \tag{9}$$

Therefore, the maximum MIS reflection coefficient is completely determined by two parameters, $\operatorname{Re}\Delta\chi/\operatorname{Im}\Delta\chi$ and $\operatorname{Im}\chi_B/\operatorname{Im}\Delta\chi$, while the increase in the reflection coefficient achieved by choosing the optimal value of γ is the result of a compromise between the constructive interference of waves successively reflected from interfaces and absorption losses.

If absorption is minimized, the number N_{eff} of used layers is increased and therefore the resolving power increases [3, 19]:

$$\frac{\lambda}{\Delta\lambda} \approx \frac{\pi}{2} N_{\text{eff}} = \frac{\sin^2\theta}{\operatorname{Im}\chi}\left\{(1 - C^2y^2)\left[1 + C^2y^2\left(\frac{\operatorname{Re}\Delta\chi}{\operatorname{Im}\Delta\chi}\right)^2\right]\right\}^{-1/2}, \tag{10}$$
$$\chi = \gamma\chi_A + (1-\gamma)\chi_B.$$

As $\gamma \to 0$, i.e., when absorbing material layers become gradually thinner, $(\lambda/\Delta\lambda)_{\max} = \sin^2\theta/\operatorname{Im}\chi_B$.

Criteria for the choice of parameters of layer materials can be reduced to three rules [2, 3, 18]:

(1) Intermediate layers should be made of materials with the lowest absorption coefficient.

(2) The strongly absorbing MIS component should be chosen to provide the greatest $\operatorname{Re}\Delta\chi/\operatorname{Im}\Delta\chi$ ratio.

(3) The interface between the chosen materials should be physically and chemically stable. One of the most important problems is the compatibility of materials, which ideally should not chemically interact or diffuse into each other.

3. Choice of materials for multilayer interference structures (MISs)

Materials for the separating and reflecting layers are usually chosen by analyzing the absorption spectra of various materials. In this connection, of interest are the absorption edges of elements corresponding to the ionization potentials of the K, L, M, ... electron shells. The K shell is occupied by two electrons, while the L shell has three sublevels (Fig. 2) and can contain up to eight electrons. The M shell has five sublevels and can contain up to 18 electrons.

The absorption of X-rays by matter occurs due to their interaction with inner-shell electrons in atoms. When the photon energy exceeds the electron binding energy in a nucleus (the excitation threshold), the electron can be removed from the atom, which is accompanied by a sharp increase (jump) in absorption of X-rays (see Fig. 2). The wavelength corresponding to the excitation threshold energy is called the absorption edge of the given element.

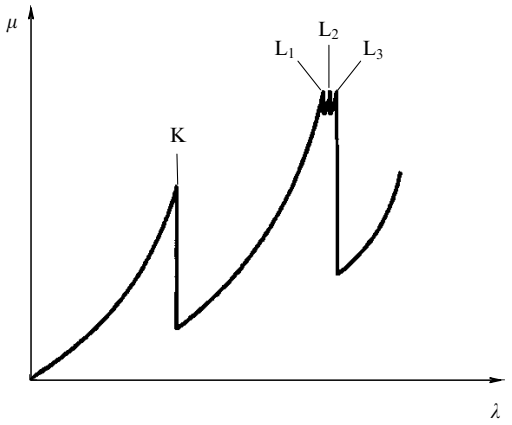

Figure 2. Schematic presentation of the X-ray absorption coefficient μ as a function of the wavelength λ of a primary photon for four X-ray absorption edges (K, L_1, L_2, and L_3).

Slightly above the absorption edge of the element (at a longer wavelength), the absorption coefficient can be quite low and the refractive index can be close to unity. Therefore, this element can be used as a material for the separating layer. Such materials are the elements of the second period of the periodic table: beryllium (Be), boron (B), and carbon (C), which are used for operation at wavelengths located directly behind their absorption K-edges; elements of the third and fourth periods: magnesium (Mg), aluminum (Al), silicon (Si), scandium (Sc), and titanium (Ti) — slightly above their absorption $L_{2,3}$ edges; and elements of the fifth period: strontium (Sr) and yttrium (Y) — slightly above their absorption $M_{4,5}$ edges [22].

The use of different materials to separate layers makes it possible to cover different X-ray spectral regions.

3.1 Two-component MISs

'Thematic' EUV and soft X-Ray spectra can be conventionally separated into several ranges: the water window (2.3–4.4 nm), carbon window (4.4–5.0 nm), lithographic (6–13 nm), 9–14 nm, astronomic (17–35 nm), 35–50 nm, and hard X-ray ranges.

3.1.1 Water window range (2.3–4.4 nm). The water window is located between the absorption K edges of oxygen and carbon, where the absorption coefficient of water is very low, and at the same time X-rays are absorbed by organic or biological materials containing carbon. Therefore, living cells can be observed *in vivo* in their natural environment.

The water window range can be covered by MISs based on Ca ($\lambda_{L3} = 3.55$ nm), Sc ($\lambda_{L3} = 3.11$ nm), Ti ($\lambda_{L3} = 2.73$ nm), V ($\lambda_{L3} = 2.43$ nm), and Sb ($\lambda_{M5} = 2.35$ nm) (Fig. 3) [23]. However, information on using Cs and Sb to separate layers are scarce in the literature [24, 25].

The most suitable pair of materials in the low spectral region of the water window is chromium (Cr) and scandium (Sc) [24–30]. Chromium is used together with scandium because of their weak interaction. The combination of these

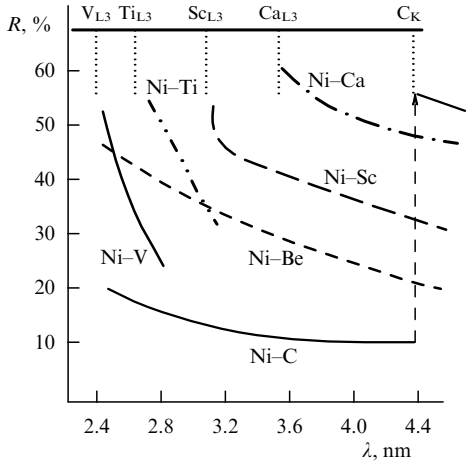

Figure 3. Calculation of the spectral dependences of the peak reflectance for MISs based on different pairs of materials in the spectral range $\lambda = 2.4-4.5$ nm [23].

materials does not overlap in the phase diagram, and therefore they do not form alloys, which alleviates theoretically the production of sharp boundaries. Multilayer Cr/Sc mirrors with high reflection coefficients reaching 14.5% and 20.7% in the normal incidence geometry ($90^\circ - \theta < 10^\circ$) were manufactured in [31] and [32].

The authors of [33] replaced chromium with vanadium to obtain a reflection coefficient equal to 18.4%.

Multiayer interference structures based on titanium and vanadium have received little attention [34–37]. It was shown in [35] that Me/Ti structures can provide reflection coefficients of up to 2.4% in the normal incidence geometry. The best results were obtained for a Cr/Ti pair due to the weak roughness of interfaces obtained with chromium.

3.1.2 Carbon window range (4.4–5.0 nm). The carbon window supplements water window microscopy and occupies a special place in the soft X-ray range. This is because carbon-containing materials, including biological and medical devices, polymers, carbon fibers, and nanotube conglomerates, are most transparent in this spectral region due to the K-jump of carbon absorption at a wavelength of 4.4 nm. In this case, the radiation penetration depth in carbon-containing materials exceeds 10 μm. The absorption of radiation by carbon atoms is tens to hundreds of times weaker than by atoms of other chemical elements. Such a difference in the absorption provides an acceptable contrast in the X-ray images of materials and biological structures, even for small additions of various elements to materials consisting mainly of carbon [38, 39].

Carbon-based MIS optics ($\lambda_K = 4.37$ nm) (Fig. 3) demonstrate the reflectivity measured at the carbon line $K\alpha = 4.47$ nm and nearly normal incident angles equal to 6–13% for Fe/C and Co/C [25, 40], 8.5% for V/C, and 7% [41] and 12.2% [23] for Cr/C. In the carbon window region, a standard multilayer Co/C optical system provides the peak reflectivity $R \approx 15\%$ for planar and $R \approx 6\%$ for bent substrates [42].

3.1.3 Lithographic range (6–13 nm). The X-ray lithography method, in which the template image is transferred to the surface of a silicon plate by a system of normal-incidence multilayer mirrors, is now considered the most probable basis for technology of manufacturing next-generation integrated microcircuits. EUV lithography is the leading candidate for optical lithography for manufacturing integrated circuits. The choice of the spectral range for EUV lithography is determined by the prospects of obtaining a spatial resolution of 10–15 nm and by the presence of highly reflecting multilayer coatings.

The density of transistors in an integrated circuit is determined to a great extent by the ability of the lithographic process to print more and more narrow details with sharp boundaries. The basic lithographic system contains multilayer mirrors as the main and most important components of illumination and projection optical devices. Because the output reflection coefficient of a lithographic system is equal to the product of reflection coefficients of each optical element, these mirrors should reflect at least 70% of the incident radiation to provide the sufficient EUV transmission for manufacturing integrated circuits [43, 44]. This condition can be theoretically satisfied for La/B, Mo/Be, and Mo/Si MISs (Fig. 4). The maximum reflectivity achieved at present for the well-studied Mo/Si MIS [46–52] at a soft X-ray wavelength of 13.4 nm is 71% [50], which makes this optical device the most in-demand for modern lithography.

The authors of [53] believe that to minimize risks, it is necessary to think about lithography at other wavelengths different from the generally accepted 13.4 nm. The most promising weakly absorbing materials can be Be ($\lambda_K = 11.1$ nm) and B ($\lambda_K = 6.6$ nm). Multilayer interference systems consisting of Mo/Be, Ru/Be, and Rh/Be were synthesized and studied in [54]. The peak reflection coefficient of Mo/Be MISs at a wavelength of 11.3 nm was 68.7% [55] and 69.4% [56]. Experimental data suggest that the efficiency of beryllium-based optical systems can be higher than that of Mo/Si MISs.

An alternative approach can be the use of shorter wavelengths. Calculations performed for an La/B nanolithographic system at a wavelength of 6.7 nm revealed advantages of this system in efficiency and spatial resolution over the Mo/Si system operating at 13.4 nm. The results in [57, 58] confirmed that the maximum reflectivity at a wavelength of 6.7 nm is obtained by using multilayer mirrors with lanthanum as a reflector and boron as a separating material. Boron is a preferable separating material for this wavelength because it is close to the absorption K-edge.

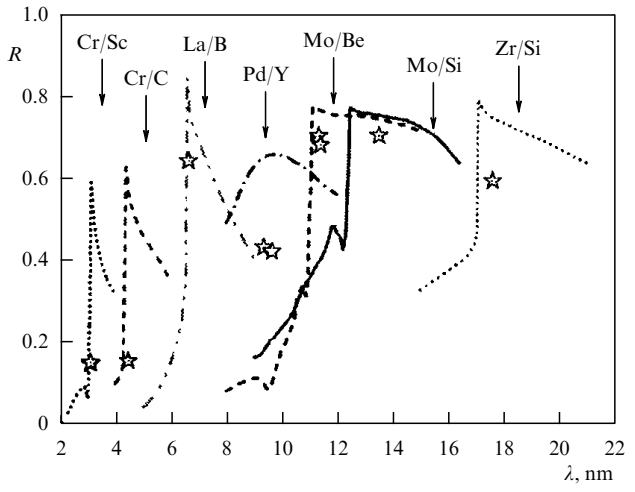

Figure 4. Calculated (lines) and experimental (stars) reflectance of the most promising normal-incidence MISs [45].

Because the magnetron-sputtering rate for pure boron is very low, some boron carbides such as B_4C and B_9C are used instead of boron in practice. Systematic studies of multilayer La/B, La/B_4C, La/B_9C, and La_2O_3/B_4C mirrors have shown that multilayer La/B_4C structures have the best reflection coefficients [57, 59–62]. For example, the maximum reflectivity of the La/B_4C MIS at 6.58 nm was 48.9%. The reflectivity of the La_2O_3/B_4C MIS at the same wavelength was 39.2%, whereas the reflectivity at 6.63 nm was 42.7% [60]. The high reflectivity of 57.3% [62] and 58.6% [61] was measured at a wavelength of 6.6 nm for almost normal incidence on a multilayer La/B mirror containing 175 bilayers and on an La/B_4C MIS, respectively.

Along with applications in lithography, La-based multilayer structures seem to be especially interesting for detecting boron [63–66]. The reflectivity of a multilayer La/B_4C mirror exceeds that of a multilayer Mo/B_4C mirror, which was earlier the most efficient multilayer element for detecting boron, with the reflectively of 53% at 6.8 nm (38% for Mo/B_4C). In addition, La/B_4C better suppresses the undesired fluorescence of Si. This is important in studies of Si-containing samples, for example, in the semiconductor industry. Similarly, La/B_4C better suppresses the fluorescence of O_K [64, 65]. Both effects reduce the background signal in samples containing great amounts of silicon and oxygen [67].

Apparently, the La/B_4C MIS has the highest theoretically achievable reflection in the 6.7–9 nm range [60]. However, a strong mixing of the La and B_4C layers prevents the formation of sharp boundaries and reduces the reflection coefficient by a factor of 1.5–2 compared to its theoretical value [68]. The Sb/B_4C MIS is one of the most promising systems due to the favorable combination of the optical properties of Sb and B_4C. The low absorption of EUV radiation in both materials and a quite substantial difference between the real part of the refractive index and unity in the range $\lambda > 8$ nm in antimony [69, 70] should result in the high reflectivity of the multilayer mirror in the wavelength range 6.7 – 9 nm. Sb/B_4C multilayers also have one of the highest theoretically achievable reflection coefficients. At the same time, no mixing is expected for the Sb/B_4C MIS because it consists of noninteracting materials: Sb does not form compounds with carbon or boron and is very weakly soluble in both of them. This should lead to the formation of sharp boundaries resulting in high reflectivity. The production of multilayer Sb/B_4C mirrors, measurements of their reflectivity, and some data on the production of aperiodic Sb/B_4C multilayers were first reported in [70]. The Sb/B_4C MISs manufactured in [71] had the reflection coefficient 19–28% measured for almost normal incidence in the wavelength range 6.64 – 8.5 nm. The reflectivity proved to be higher than for multilayers based on many pairs of conventional materials optimized for wavelengths from 6.6 to 9 nm. However, it was lower than the reflectivity of the La/B_4C MIS [71].

3.1.4 The 9–14 nm range. This range is also of special interest for experiments with free-electron lasers [72] and for solar physics because of the bright coronal 9.4-nm Fe XVIII line, bright Fe VIII, Fe XXII, and Fe XXIII lines near 13.1 nm, and other weak emission lines [73].

The most promising absorbing material in the spectral region from 8 to 12 nm is palladium, whose absorption ability is almost the same as that of Mo, whereas the real part of the polarizability at 9.5 nm is 1.5 times greater. As a result, the calculated reflectivity of the Pd/B_4C mirror is higher than that of Mo- and La-containing MISs in the range 8 – 11 nm [58, 74]: the theoretical peak reflection for linearly polarized X-rays for $\theta = 45^\circ$ was 58%, while the experimental value was 42%. This discrepancy can be related to the interface quality [72].

The replacement of a B_4C spacer by Y ($\lambda_{M5} = 8.0$ nm) with lower absorption additionally increases the reflectivity up to 65% for the Pd/Y MIS at 9.5 nm [75, 76] (see Fig. 4).

The authors of [77] compared the Mo/Y, Ru/B_4C, and Ru/Y MIS prototypes for detecting the solar spectrum FeXVIII line. In this study, the Mo/Y MIS does provide the highest reflection coefficient $R = 34\%$, to be compared to 28.3% for the Ru/B_4C MIS studied earlier [78] and equal to only 77% of the theoretical reflection coefficient [79]. The Mo/Y MIS was first manufactured in [80, 81] and had a reflection coefficient of up to 46% at 11.4 nm for almost normal incidence.

To fill the spectrum 'gap' between boron- and beryllium-based MISs more efficiently (see Fig. 4), strontium ($\lambda_{M5} =$ 9.2 nm) [82] and phosphorus ($\lambda_{L3} = 9.2$ nm) [22, 83] were proposed as elements for the spacer. For an Mo/Sr mirror, the reflection coefficient of 48.3% at 10.5 nm that was obtained in [82], also lower than the theoretical limit of 65%, looks promising.

The direct use of P in MISs is unlikely because of the high reactivity of phosphorus, which forms solid compounds (phosphides) with almost all chemical elements. It is believed that boron phosphide (BP) can be used as a separating material in reflection multilayer optics operating slightly above the absorption L edge of P. As reflecting materials, Mo, Ag, Ru, Rh, and Pd were considered. Calculations performed for multilayer structures with perfect interfaces have shown that the Pd/BP combination of materials provides higher reflectivity, exceeding 70% in the 9.2–10.0 nm spectral range [22]. The authors of [84] have also shown that the maximum reflectivity of Pd/BP and Pd/Sr MISs can exceed 70%.

3.1.5 Astronomic range (17–35 nm). The 17–35 nm EUV range is one of the most interesting for modern astrophysics. Telescopes, spectrometers, and chronographs operating in this range are used to study white dwarfs and interstellar media, the Sun, and the atmosphere of the Solar System planets [85, 86]. The 17–35 nm range of the solar spectrum is the most informative for diagnostics of the coronal plasma because it contains the main spectral lines of the plasma, such as the 17.1 nm Fe IX, 19.5 nm Fe XII, 21.1 nm Fe XIV, 28.4 nm Fe XV, 30.4 nm He II, and 33.5 nm Fe XVI lines. The X-ray spectral imaging of the solar disk and corona in the radiation of iron and helium ions corresponding to monotemperature layers of the solar atmosphere plasma in a broad temperature interval with high spatial, spectral, and temporal resolution provides a basis for the observation and studies of the Sun.

In particular, Al-based multilayers ($\lambda_{L3} = 17.1$ nm) have potential applications for the fabrication of layers operating in the 17–19 nm range because many aluminum-based multilayer combinations have a high reflectivity in this range [87].

Two multilayer Al-based structures (SiC/Al and Zr/Al) were studied for use at wavelengths exceeding the absorption L-edge of Al [88–92]. Notably, the Al/Zr system still provides the highest reflectivity. The Al/Zr coating with a period of

8.85 nm provides a reflectivity of about 60% at 17.3 nm. Al/Zr multilayers have a very low film strain and good temporal stability: the reflectivity of the Al/Zr MIS prototype has barely changed in several years [93].

Multilayer Y/Al structures have also been studied experimentally. However, it was found that the peak reflection of Y/Al MISs at 19 nm was only about 18%, which is considerably lower than the theoretical value. Moreover, the peak reflection of these coatings gradually decreased to 1% or lower after storage in air for $\sim$ 300 days [88].

The reflectivity of an Mo/Al MIS at a wavelength of 18.5 nm was 33.5% [94]. However, due to its optical constants, the most efficient material for separating layers in the 25–35-nm range is magnesium ($\lambda_{L3} = 25.1$ nm) [95].

The 30.4 nm He II emission line used in solar physics, for example, for solar corona imaging, requires highly reflecting multilayer mirrors. Mirrors operating at 30.4 nm were developed by studying several combinations of magnesium-based materials, including SiC/Mg, B_4C/Mg, C/Mg, Co/Mg, and Si/Mg [96, 97]. The maximum reflectivity of Co/Mg and SiC/Mg MISs reached 40.3 and 44.6%, respectively, for almost normal incidence. These results show that multilayer SiC/Mg and Co/Mg mirrors are promising for use at a wavelength of 30.4 nm.

The Mg/SiC MIS has attracted the attention of researchers due to the unique combination of high reflectivity (more than 40% [98, 99]), good spectral selectivity, thermal stability up to 350 °C, and the almost total absence of stresses [99–102]. However, the SiC/Mg system undergoes very strong degradation due to Mg corrosion. This problem made SiC/Mg coatings impractical for applications requiring long-term stability, for example, in experiments with synchrotron radiation or space telescopes [102].

The thermal stability of Mg/Co is better [103]. In addition, it was shown in [104] that interfaces in the Co/Mg system are sharp and the mutual diffusion between Co and Mg layers is absent. This example emphasizes the importance of choosing the material to be used together with magnesium, such that it does not interact with the latter and provides high reflectivity. Zirconium is one such material. Magnesium and zirconium do not interact with each other. The authors of [105] showed that the thermal stability of Zr/Mg mirrors during annealing at up to 600 °C was higher than that of Y_2O_3/Mg, SiC/Mg, and Co/Mg. The reflectivity of Zr/Mg is 30.6% at 30.4 nm. The reflection coefficient slightly decreases upon increasing the annealing temperature to no higher than 500 °C and finally drops to 15.1% at 600 °C. This degradation is explained by the roughness of interfaces caused by the relaxation of stresses.

3.1.6 The 35–50 nm range. The EUV region above 40 nm contains a few important lines of the solar spectrum, including the 46.5 nm Ne VII, 63.9 nm O V, and 83.50 nm O III lines. The radiation penetration depth in the 35–50 nm range is minimal for the entire range of electromagnetic waves. This has so far prevented the development of good multilayer coatings, because radiation is absorbed in the external layer and the efficiency considerably depends on the surface contamination. In addition, knowledge of the optical constants of reflecting materials is strongly restricted due to the same reason, which complicates the systematic development and optimization of multilayer coatings.

In transition metals (Sc, Ti, V, Cr, Mn, Fe, Co, Ni, Cu, Zn), competition between the occupation of the 3d and 4s shells occurs. Because the 3d shell in all these elements is unfilled, the 3p–3d optical transition from the inner 3p shell is allowed. It is known that this transition produces strong resonance in the absorption spectra of all transition metals. The ideal combination of excitations of valence and conduction electrons makes the first element of this series, Sc, the most promising for MISs operating in the 35–50 nm range, while analysis of absorption spectra and calculations of optical constants [106] shows that the Sc/Si pair is the best coating [7, 77, 107].

The normal-incidence reflection coefficient of Sc/Si mirrors is 30–54% [108]. These values are not the upper bound for Sc/Si coatings however. Theoretical estimates and electron-microscopy studies of Sc/Si interfaces demonstrate a great potential for further increasing their reflectivity [108, 109].

Normal-incidence Sc/Si MISs are used in important fields such as X-ray lasers, X-ray microscopy, and astrophysics.

At present, the number of MISs operating in the 50–115 nm range is very limited. Recently, lanthanides and elements close to them have attracted the attention of researchers because of their relatively low absorption in the EUV band [110]. These studies revealed lanthanides with the lowest absorption in the 50–115 nm range. Multilayer structures based on Tb [111, 112], Gd [113, 114], and Nd [113] in combination with Si and SiC were developed. Multilayer structures based on La and B_4C for wavelengths exceeding 69 nm with the maximum reflectivity at 90 nm were developed in [115]. La/B_4C MISs for the 70–115 nm range have been fabricated, and the production of more efficient multilayer films is expected.

Reflectivity exceeding 20% for almost normal incidence was measured for the Si/Tb (SiC/Tb) MIS at a wavelength of 60 nm [111]. Si/Gd MISs operating at 62 nm had the maximum reflection coefficient of 26.2% for the incidence angle of 5° [114].

3.1.7 Hard X-ray range. For normal-incidence optical devices, a wavelength of 3 nm is the current limit for inclined (grazing) incidence, but multilayer devices are successfully used in the hard X-ray range as well [7].

Because of the weak absorption of X-rays in the hard X-ray spectral region, chemical elements with a large atomic number Z can be used as materials for the absorbing layer. Therefore, a pair of materials with a high density contrast and low absorption should be chosen here. The density ratio is a good indicator of the reflectivity of each interface. Other important characteristics for manufacturing multilayer mirrors are the time stability and compatibility of materials. In the ideal case, the chosen materials should not chemically react or mix with each other, avoiding the formation of second phases, thereby increasing the smoothness of interfaces and the reflectivity of optics.

These requirements are satisfied for W/Si [116–119], W/B_4C [116, 120–123], W/SiC [116, 124, 125], Pt/C [117, 119, 124, 126], Pt/SiC [124], Ni/C [119, 123, 127], Ni/B_4C [123, 127], and Cu/Si [123] MISs intended for applications in astrophysics. However, the use of tungsten-based MISs is restricted by the energy below the absorption K-edge of W (69.5 keV). For a number of scientific goals, it is necessary to use spectral ranges up to 100 keV or even above, and hence proper pairs of materials (without the absorption K-edge in the required energy range) should be found. Cu/Si, Mo/Si, Ni/C, Ni/B_4C, Pt/C, and Pt/SiC multilayers can be used

instead of the W/Si MIS. Except the Pt/C (Pt/SiC) MISs restricted by the absorption K-edge of Pt (78.4 keV), all these materials have rather good reflectivity in the energy range from 20 to 100 keV and above. Multilayer structures based on W, Pt, and Ni give excellent results. The higher silicon deposition rate compared to that of carbon could probably make the Cu/Si MIS the best choice for mirrors reflecting X-rays beyond the absorption K-edge of W, but this MIS proved to be unstable [118] and therefore unsuitable for use in X-ray telescopes. The Mo/Si MIS, although popular for the EUV range, poorly operates above 20 keV because of its high absorption [119].

Despite their high absorption, W/Si MISs can be efficiently used in mirrors operating at energies considerably exceeding 100 keV [118, 125].

3.2 Three-component MISs

Three- or four-component MISs have been studied theoretically and experimentally in the wavelength range from 1.3 to 6.8 nm in [129]. The authors demonstrated that the addition of a third material can improve the reflectivity and proposed criteria for selecting materials. The principle for improving reflection is based on the optimization of the refractive-index distribution in the period taking both the reflection coefficient of separate layers and absorption of radiation in the whole structure into account [130].

As regards wavelengths above 50 nm, Larruquert has developed a theory for quasiperiodic multicomponent MISs made of highly absorbing materials and proposed a selection rule for materials for reflectivity optimization [130, 131]. Unfortunately, this theory does not work for $\lambda < 50$ nm because most of the materials moderately absorb X-rays. Nevertheless, Larruquert proposed several multicomponent multilayer systems (for $\lambda = 30.4$ and 50 nm) using his selection rule. These strictures theoretically provide an increase in reflectivity, this increase being most efficient when a third material is added to a 'classical' MIS [131].

Multicomponent MISs have more interfaces per constant optical path $\lambda/2$ (two-layer period for standard multilayers) than standard two-component MISs. Thus, the greater number of interfaces near the external surface provides additional contributions to the reflection strength.

Materials are selected by mapping the refractive indices ($\mathrm{Re}\, n$, β) of all available materials in the $\mathrm{Re}\, n$–β complex plane and connecting the extreme refractive indices to form a closed polygon (Fig. 5). The minimal polygon is one with the minimum number of vertices encompassing the optical constants of all materials. The choice of materials with optical constants located inside the minimal polygon reduces the reflection coefficient, independent of the number of materials. The choice of a material and its deposition order can be made by going around the minimal polygon clockwise (see Fig. 5) [132].

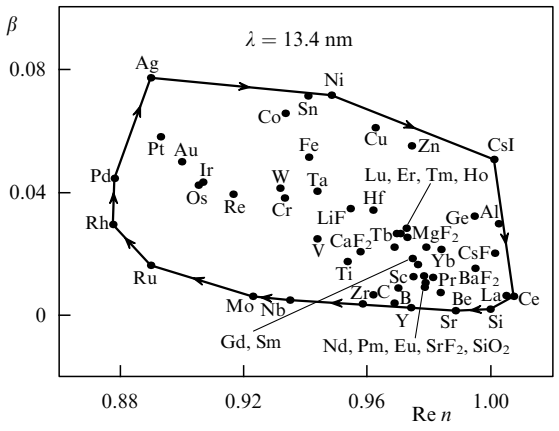

Figure 5. Optical constants of materials at $\lambda = 13.4$ nm. The minimal polygon (solid curve) includes all materials [132].

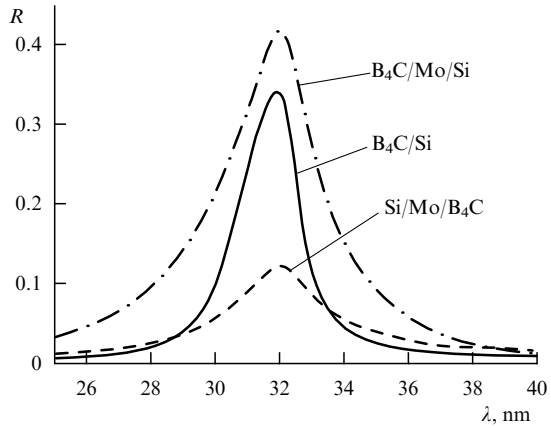

Figure 6. Normal-incidence reflectance spectra calculated for the optimized B_4C/Si MIS (solid curve), $B_4C/Mo/Si$ MIS (dashed-dotted curve), and the $Si/Mo/B_4C$ MIS with the reverse order of layers (dashed curve) [133].

As predicted by theory [130, 131], the material deposition order is decisive when three or more materials are used. The spectral responses of three MISs are compared in Fig. 6. The solid curve represents a simulation of the standard B_4C/Si MIS optimized for $\lambda = 32$ nm. The dashed-dotted curve is the simulation of the $B_4C/Mo/Si$ MIS. The dashed curve is the reflectivity of the same three-component MIS with the same thickness but deposited in the reverse sequence: $Si/Mo/B_4C$. A relative increase in the reflectivity by 23% is observed for the optimal sequence $B_4C/Mo/Si$ and a decrease by 63% is observed for the inverted MIS deposition [133].

However, the Larruquert selection rules cannot always be applied [133, 134]. One of the reasons can be the instability of materials and interfaces ignored by the theory. Nevertheless, these selection rules for materials can be used as a guide to find the optimal structure [133].

4. Calculation of MIS parameters

The main optimization parameters for two-component MISs are the materials of layers A and B, their thickness, the order of layers ($ABAB...$ or $BABA...$), the total number of bilayers N, and the multilayer structure period d. In general, the optimization process uses a merit function, which is determined by the project task. The choice of appropriate multilayer materials based on optical constants and stability of materials is the starting point of the projecting process. The optimization of individual constructions is a complex problem, which can be solved only by using various computer algorithms. The important technological constraint is that the optimal structure should be as simple as possible, i.e., ultrathin layers and sharp variations in the layer thickness should be avoided [135].

In all cases, the optimization problem involves the multiparametric minimization or maximization of the merit

function [136]. The merit function (general in the optimal control theory) is the root-mean-square error between the calculated reflection coefficient and its goal value [137]. Optimization assumes finding the global minimum of the merit function or, at least, a minimum deep enough where the root-mean-square error is so small that the calculated profile of the reflection coefficient is very close to the desired profile. The search for the global minimum is an extremely complex problem of minimizing a function of many variables. Most of the existing approaches to the problem of synthesis of multilayer mirrors are based on complex computer software requiring time-consuming calculations.

The corresponding optimization algorithms allow finding the optimal multilayer structure and its design and determining the most realistic multilayer structure. Most such algorithms are based on the recurrent Parratt formulas [138]. The optimization algorithms are divided into local and global [135, 139]. The local algorithms concern situations in which the approximate range of optimal values is known before optimization. The general local algorithms are mainly based on the least gradient methods, in particular, the quasi-Newtonian method [140, 141], the saddle-point method [142], and the Levenberg–Marquardt (LM) algorithm [143, 144]. The last method works better when the initial values lie near the global minimum, for example, initial values can be calculated analytically from the experimental reflectivity curve [145], and can be used to refine the calculated values of parameters [146]. The simplex algorithm [147] finds the nearest local minimum. A more global minimum can be found using an iterative procedure.

Global algorithms have a large search space. Therefore, the search for the optimal structure always requires more time than in the case of local algorithms, but also local results that 'miss' the global optimum are prevented. Global algorithms play a more important role than local algorithms because of their wider ranges and greater searching possibilities. Global algorithms are often based on natural phenomena and processes. Genetic algorithms are a very powerful class of minimization algorithms [148]. They were successfully used by several authors (see, e.g., [149, 150]). The annealing imitation algorithm uses an ordered random search based on an analogy with the process of crystal structure formation by matter with the minimal energy during cooling [151, 152]. This algorithm is realized in a program for analyzing a multilayer structure [153]. The random search (RS) algorithm [154], the topographic optimization algorithm [155], the particle swarm optimization (PSO) algorithms [156], and the ant colony optimization (ACO) algorithm [157] are also well known.

To handle a great number of parameters characterizing a multilayer structure and to obtain the values of parameters providing the best fit of experimental data, a number of computer programs have been developed, such as the PPM (Pythonic Program for Multilayers) for the rapid multiparametric optimization of MIS reflectivity for one or simultaneously several X-ray energies [158, 159].

The optical properties of MISs can be simulated using IMD software [160], which allows simultaneously simulating up to eight independent variables and estimating parameters (including the formation of the confidence interval).

The advantages and disadvantages of a particular algorithm are estimated according to the various requirements for the optical parameters of MISs. In addition, in choosing the appropriate optimization algorithm, it is necessary to maintain a balance between the computation time and the search accuracy.

5. MIS deposition methods

The next stage of MIS manufacturing is the deposition of multilayer coatings on a mirror surface. Considerable progress in the development and studies of multilayer structures has been achieved in recent years [2, 5, 11, 161, 162]. Many combinations of materials and deposition technologies can be regularly used in the industrial manufacturing process.

Most of the research groups producing multilayer coatings use magnetron sputtering [5, 47, 163–166] as a very reliable and efficient method of deposition of nanometer high-quality multilayer films for EUV and X-ray applications [167]. The very high stability of the deposition process, along with the possibility of controlling the microstructure of the layers, provides the high repeatability of the layer thickness along a stack with a large number of periods [168]. The magnetron scattering method is apparently the best deposition method [169].

Along with the magnetron spattering method, ion-beam deposition [170, 171], electron-beam evaporation [49, 172, 173], and pulsed laser deposition technologies [174–176] are used. Pulsed laser deposition is successfully used to manufacture high optical quality MISs. The excellent possibilities of this method provide film thickness uniformity, a high accuracy of the deposition process, the formation of smooth interfaces, and the suppression of the columnar growth of thin films. The synthesis of large-area X-ray optical multilayers by the laser deposition method was demonstrated in [176].

Each method has its own disadvantages and advantages. In many cases, the optimized composition allows choosing a suitable deposition technology for obtaining the most efficient MIS.

6. MIS investigation methods

The Table presents the parameters of some MISs grown for use in normal-incidence mirrors: the bilayer period ($d \approx \lambda/2$), the number N of bilayers, the parameter γ, the calculated (R_{theor}) and measured (R_{exp}) reflection coefficients, and the spectral resolution $\lambda/\Delta\lambda$. In all examples presented in the

Table. Optical characteristics (calculation and experiment) of normal-incidence MISs in the wavelength range 3 – 17.4 nm.

λ, nm	MIs	d, nm	N	γ	R_{theor}	R_{exp}	$\lambda/\Delta\lambda$	References
3.14	Cr/Sc	1.56	–	–	0.46	0.15	–	[28]
4.47	Cr/Sc	2.21	200	–	0.24	0.075	186	[177]
4.47	Co/C	2.26	200	–	0.38	0.148	153	[178]
6.7	La/B_4C	3.39	150	–	0.65	0.44	120	[179]
8.5	Sb/B_4C	–	300	–	0.378	0.18	–	[70]
9.5	Mo/Y	–	120	0.42	–	0.384	–	[79]
11.34	Mo/Be	5.74	70	–	0.750	0.702	38	[180]
13.2	Mo/Si	6.8	50	0.41	0.76	0.66	26	[90]
17.35	Zr/Al	8.7	50	0.37	0.63	0.56	29	[90]

Table, the value of R_{exp} is lower than R_{theor}. Among a variety of observed defects (impurities, deviation of the layer density from tabulated values, MIS surface quality, etc.), the most important role in the deterioration of the optical characteristics of MISs is played by the roughness of interfaces and the intermediate layers.

An intermediate layer at the interface between films is the result of both complex physicochemical growth processes of ultrathin films and the interplane roughness inherited from the initial substrate roughness. The size of islets, the film uniformity, and the initial substrate roughness form the geometrical profile of interfaces whose influence on X-ray scattering can be characterized by the roughness σ_r. The mixing of layers caused by mutual diffusion during the growth process results in the spread of the electron density jump and can be represented by the mean mixing depth σ_d. The determination of parameters σ_r and σ_d, the minimal film thickness at which their uniformity is preserved, is important for understanding the MIS growth physics and optimizing the MIS manufacturing process [181].

If the mean gradient of the composition at the layer interface is represented by the Gaussian half-width σ, the reflection coefficient R_σ in the mth order is [182]

$$R_\sigma = R_0 \exp\left(-\frac{16\pi^2\sigma^2 n_A n_B \sin\theta_A \sin\theta_B}{\lambda^2}\right), \qquad (11)$$

where R_0 is the reflection coefficient for the ideal MIS with $\sigma = 0$, n_A and n_B are the refractive indices, and θ_A and θ_B are grazing angles for the two components of the multilayer structure. The total width σ can be calculated as the quadratic sum

$$\sigma^2 = \sigma_r^2 + \sigma_d^2 . \qquad (12)$$

To properly understand the bilayer structure, it is necessary to use more complicated structural models describing gradient interdiffusion layers. This inevitably increases the number of parameters, which can be determined only after the combined analysis of MISs by several experimental methods. The MIS structure was studied in a number of papers [30, 104, 177, 183–187] by using a combination of two or more noninvasive methods, such as X-ray reflectometry [188, 189], X-ray emission spectroscopy (EXAFS) [190], nuclear magnetic resonance (NMR) spectroscopy [191], the X-ray standing wave technique (spectral fluorescence analysis) [192], diffuse scattering [193, 194], atomic force microscopy [195, 196], X-ray emission spectroscopy [197], and invasive methods such as time-of-flight secondary-ion mass spectrometry (ToF-SIMS) [198] and transmission electron microscopy (TEM) [199].

The most efficient method for studying the structural characteristics of MISs is X-ray reflectometry. This method gives the thickness and electron density of layers, thickness fluctuations, the width σ of intermediate layers, and their asymmetry [52, 59, 200]. In addition, X-ray reflectometry can be efficiently used for *in situ* monitoring of the thickness of deposited layers during MIS growth [201].

The layer thickness, roughness, and density parameters of the upper layers of grown multilayer films determining the MIS properties considerably differ from the parameters of lower layers due to the reaction of the upper layers with the environment. The X-ray reflectometry method is not very sensitive to the parameters of the upper layer, especially in the case of multilayer samples. Surface layers are characterized by the method of X-ray photoelectronic spectroscopy [187].

To know the type of defects (σ_r or σ_d), reducing the reflectivity is important for a number of reasons. First of all, this knowledge allows introducing corrections to the MIS manufacturing technology required for eliminating this defect. In addition, the roughness, unlike mixed zones, considerably affects not only the reflectivity but also the spectral resolution of the MIS [202]. Therefore, it is important to be able to separate the contributions of σ_r and σ_d to the total width σ of the interface. X-ray fluorescence experiments based on the X-ray standing wave method provide the measurement of the diffusion layer thickness σ_d [30], while angular dependences of diffuse X-ray scattering give information on the correlation function of the roughness profile and allow finding the parameter σ_r [181].

During the deposition of layers, other factors can also be involved, which can affect the reflectivity in different ways. For example, the crystallization of the film material, on the one hand, should increase the roughness of layer boundaries, implying that this effect is negative. On the other hand, the matter density increases upon crystallization, which is obviously a positive factor for strongly absorbing layer materials, because this results in an increase in the permittivity jump. The negative effect of the polycrystalline structure is diffusion along grain boundaries with typically a high velocity, which can destroy the uniformity of layers [181]. The microstructure of layers and intermediate regions can be studied by the method of transmission electron microscopy.

Another invasive method, time-of-flight secondary-ion mass spectrometry, is used to study the depth distributions of various elements contained in MISs.

The NMR spectra give the distributions of atoms depending on their resonance frequency. The NMR frequency is sensitive to the local environment of the atoms probed: their number, nature, and symmetry [203].

The two remaining noninvasive methods, X-ray emission spectroscopy and atomic force microscopy, are used to determine the chemical state of atoms in multilayers and the presence of some interphase compound, as well as to study the roughness of the substrate and MIS surfaces.

Thus, the experimental methods briefly considered above ensure a comprehensive structural analysis of MISs.

7. MIS improvement methods

MISs are key optical components in the soft X-ray and EUV wavelength ranges. However, because all solid materials strongly absorb X-rays in these spectral regions, EUV mirrors can be strongly heated. With the increasing power of soft X-ray and EUV sources (synchrotrons [204], free-electron lasers (FELs) [205], high-harmonic generators [206], discharge capillary lasers [207]), the stability of multilayer optics becomes the decisive factor. Thus, it is necessary to increase the temporal, thermal, and mechanical stability of MISs.

7.1 Methods for reducing mutual diffusion

To improve the thermal stability of multilayer mirrors, two strategies are used. The first, applied to short-period structures, is based on the choice of components in phase equilibrium with each other. For this purpose, pure components are often replaced by alloys or compounds. The second strategy uses antidiffusion barriers between layers to prevent

the solution and chemical reactions of components. This strategy looks preferable for long-period MISs [208].

7.1.1 Barrier layers. An improvement in multilayer stability and (or) a decrease in the diffusion layer thickness have been achieved for several combinations of materials by introducing a thin layer (the so-called barrier layer) at the interface, usually from 0.3 to 1 nm in thickness [50].

B_4C is a stable ceramic and also a common diffusion barrier layer. The efficiency of this barrier layer has been demonstrated for several multilayer structures. The B_4C diffusion barriers 0.3–1.0 nm in thickness increase the thermal stability from 150 to 400 °C for the Mo/Si MIS [209] and from 100 to 200 °C for the Sc/Si MIS [210].

The decrease in mutual diffusion caused by the introduction of a B_4C layer was experimentally proved in [211], where the mean thickness of the interphase region was estimated as 0.9 ± 0.2 nm for Mo/Si multilayers and 0.5 ± 0.1 nm for $Mo/B_4C/Si/B_4C$ multilayers.

Diffusion barriers consisting of C or B_4C favor the formation of compounds with MIS materials stable up to the maximal temperatures and duration of annealing [212]. The introduction of C and B_4C barrier layers reduces the formation of well-known $MoSi_x$ mixing zones [213] at interfaces and improves the optical contact between absorbing and separating layers. The use of these barriers resulted in an increase in the MIS reflectivity from 68.7% ($\lambda = 13.46$ nm, $90° - \theta = 1.5°$) for Mo/Si multilayers to 69.9% ($\lambda = 13.5$ nm, $90° - \theta = 1.5°$) for $Mo/B_4C/Si/C$ multilayers [214].

The influence of Be barrier layers on the reflection coefficient of multilayer Mo/Be/Si mirrors was reported in [215]. The reflection coefficients of samples were above 71% at $\lambda = 13.5$ nm and above 72% at $\lambda = 12.9$ nm for nearly normal incidence. Calculations showed that by optimizing the Be layer thickness, the reflection coefficient can be further increased by 0.5–1%. These results are of great interest for EUV lithography.

The main disadvantage of Sc/Si mirrors is their low thermal stability caused by the thermodynamic instability of such structures. According to the phase diagram, scandium and silicon form a number of intermediate compounds, silicides, which should appear already during the manufacturing of the mirror. If the mirror is subjected to thermal or radiative action during operation, a further formation of silicides occurs. The formation of silicides is accompanied by a significant change in the specific volume, resulting in a change in the period of the multilayer mirror and therefore a change in the resonance wavelength. As a result, the mirror becomes off-resonance, and the reflection coefficient at the operating wavelength drastically decreases [216].

For Sc/Si MISs, various barrier materials have been used [217]. It was shown in [208] that W layers 0.5–0.8 nm in thickness located at Sc/Si interfaces form efficient barriers preventing the diffusion of Si into Sc. Multilayer Sc/W/Si/W films with a period of 20.5 nm produced by magnetron spattering had a thermal stability up to 250 °C and the normal-incidence reflection coefficient 24% at wavelengths of about 40 nm. Although tungsten is an efficient diffusion barrier, its high absorption reduces the reflectivity. It was found in [218] that the use of B_4C increases the thermal stability of multilayer Sc/Si films, while the reflectivity decreases by only a few percent.

CrB_2 barrier layers can be promising for Sc/Si MISs. The CrB_2 material was chosen in [219] because of its high melting temperature (2473 K) and because chromium does not interact with scandium.

The ultrathin B_4C barrier layers have recently been successfully used to suppress the interdiffusion between Cr and V in the Cr/V MIS [220]. X-ray reflectometry showed that the width of multilayer interfaces considerably decreased to 0.21–0.31 nm after the introduction of B_4C barrier layers 0.1 nm in thickness in both interfaces [221].

The optical characteristics of the Mg/Co MIS remain stable if a multilayer stack is not annealed at temperatures above 200 °C [222]. To increase this temperature limit, B_4C, W, and SiN barrier layers were introduced into Mg/Co. The dependence of the reflectivity on the annealing temperature showed that B_4C is not suitable for the Mg/Co MIS, because interlayer diffusion can take place for Mg and B_4C. The introduction of Mo improves the thermal stability to 300 °C, but is accompanied by a loss of reflectivity. The introduction of Zr considerably improves the thermal stability of Mg/Co (up to 400 °C) without reducing the reflection coefficient. The use of a Zr barrier layer is an efficient method for improving the thermal stability of a multilayer Mg/Co material for applications in the EUV radiation region [134, 183, 222].

The authors of [61] have managed to suppress the formation of intermediate layers in the La/B_4C structure to a great extent by using ultrathin (~ 3 Å) barrier carbon layers to obtain the maximum reflection coefficient (58.6% at $\lambda = 66.6$ Å) for this periodic structure for normal incidence.

The reflection coefficients of an Si/Gd MIS suggest the possibility of silicide formation at the Si–Gd interfaces. B_4C, W, and SiN were used as interface barrier layers to improve the reflection coefficient of Si/Gd. The reflection coefficients of Si/W/Gd and $Si/B_4C/Gd$ MISs were observed to increase by more than 8% [114].

Figure 7 shows electron-microscope images of an Si/Gd film and an Si/Gd film with a W barrier layer after annealing for an hour at a temperature of 300 °C [223]. Although the structure of layers is still clear in Si/Gd film, 'pure' Si and Gd layers are considerably thinner and the contrast between the Si and Gd layers is weakened: the Si–Gd spacers actually expanded, probably consuming a greater part of the 'pure' Si and Gd layers during annealing. On the contrary, the annealed Si/W/Gd film barely changed. The barrier W layers in this film are 1.8 nm in thickness and are obviously quite efficient antidiffusion barriers for this structure, at least up to the annealing temperature of 300 °C.

However, the introduction of an additional layer changes the phase of waves reflected from different interfaces when the Bragg condition is satisfied, thereby producing a phase mismatch reducing the reflectivity. Therefore, to minimize the

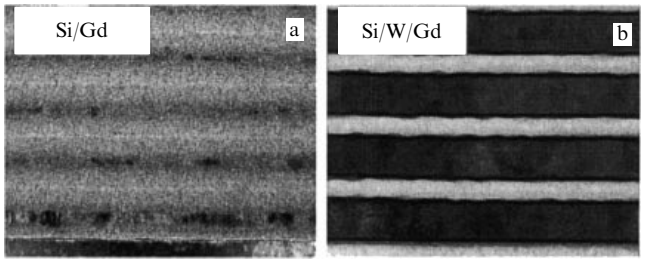

Figure 7. Electron-microscope images of the longitudinal sections of (a) Si/Gd and (b) Si/W/Gd MISs. Barrier W layers were 1.8 nm thick; the thickness of the Si and Gd layers in the Si/W/Gd film was ~ 11.1 and ~ 21.0 nm, respectively [223].

phase mismatch, the barrier layer should be ultrathin, which requires strict control of the deposition process [224].

7.1.2 Compounds and alloys. To avoid or at least suppress the mutual diffusion and formation of compounds, it is preferable to manufacture the MISs with one or even two layers (separating and absorbing) consisting of a stable compound.

Hard-melting metal (Mo, W, Nb) carbides have excellent physical properties, such as a high melting temperature, good electric conduction, and extreme hardness. Therefore, an MIS consisting of an absorbing metal carbide layer with an Si or SiC separating layer should have good reflectivity and thermal stability. For example, the Mo_2C/Si MIS demonstrated excellent thermal stability up to 400 °C [225] and even up to 600 °C with the maximal normal-incidence reflectivity of 61.8% at $\lambda = 13.0$ nm [226]. Good stability was also demonstrated by NbC/Si [227], WC/SiC [228], and Mo_2C/B_4C [229] MISs.

Compared with other conventional silicon-based multilayer systems like W/Si, WSi_2/Si not only has a lower density and lower absorption, but is also chemically more stable because WSi_2 is no longer a silicide. Thus, it is expected that the thermal stability of WSi_2/Si multilayers will be improved and they will have sharp interfaces [230].

Multilayer Mo_xSi_{1-x}/Si X-ray mirrors for soft X-rays demonstrate a high thermal stability up to 900 °C, whereas Mo/Si multilayers with the same periods are destroyed at 600 °C [231]. Thus, the $MoSi_2$/Si MIS with a high reflectivity proved to be much more stable because of the thermal equilibrium of the $MoSi_2$ and Si components at the interface [232].

The use of Mg for manufacturing MISs is restricted by two important properties of this material: the low melting temperature $T_m = 923$ K and the high chemical activity. Because of the high chemical activity, the interlayer interaction of Mg with most of the materials used in MISs occurs during their manufacturing and further operation, which reduces the reflectivity. A compromise variant may be the use of an Mg-based chemical compound. For example, the Mg_2Si compound is more hard-melting than Mg and is less chemically active. This pair of materials is also promising for manufacturing MISs, because it is a eutectic system in which interlayer interaction is absent. The theoretical calculation of the reflectivity of the Si/Mg_2Si MIS showed that despite structural phase transformations during heating, this system can provide a reflectivity of about 34% at a wavelength of 30.4 nm at normal incidence, even at 500 °C [233].

7.1.3 Nitrogenization. Reactive sputtering with nitrogen (nitrogenization) can considerably suppress interdiffusion between adjacent layers due to the formation of stable metal nitrides, as was shown for Cr/Sc [234], La/B [235], and Pd/Y [84]. If the optical constant of layers did not significantly change in this case, a higher reflectivity could be obtained compared with the MISs manufactured by the conventional method. The thermal stability of a nitrogenized multilayer material can also be improved, which is important for mirrors operating at high thermal loads [32]. Taking these advantages into account, reactive nitrogen sputtering can be promising for improving the efficiency and expanding the field of X-ray optics [236].

Several short-period Se-based MISs, including CrN_x/Sc and Cr/Sc with B_4C barrier layers, were experimentally compared in [237]. The best results were achieved for nitrogenization of Cr layers with added B_4C barrier layers. The reflectivity for 397-eV photons measured at nearly normal incidence reached 23%. The CrN_x/B_4C/Sc MIS model was proposed, which predicts a reflection coefficient exceeding 32%.

7.1.4 Annealing. Pulsed laser diffusion can be used to control manipulation of the structure of interfaces in MISs [238]. Depending on the miscibility or immiscibility of MIS materials, interfaces can be made blurred or sharp, which is explained by the inverse diffusion process. The inverse diffusion of two elements at interfaces was observed in Co/Au, Co/Ag, Co/C, and CoN/CN MISs annealed up to 250 °C [238, 239].

7.2 Methods for reducing interface roughness

The introduction of an antidiffusion barrier can sometimes also reduce the roughness of interfaces.

It is known that the reflection coefficient of the SiC/Al MIS decreases on heating up to 300 °C [240]. This occurs because of the development of roughness due to the nonuniform growth of aluminum grains. In this case, no significant interlayer diffusion is observed. The introduction of a thin Mo layer to the SiC-on-Al interface reduced the roughness and thereby improved the optical characteristics of this system: interfaces of Al/W/SiC and Al/Mo/SiC multilayers became sharper than those of the Al/SiC system [87, 89, 241].

Similar results were obtained in [220]. The $Cr/B_4C/V$ MIS with many bilayers ($N = 300$) has the same small width of the transition region as prior to the introduction of the B_4C buffer layer into the Cr/V MIS, whereas the roughness of the interfaces decreased. Electron-microscope measurements showed that the roughness decrease produced by barrier layers can be explained by the suppression of vanadium crystallization inside the MIS.

Incidentally, it was noted in [50] that the presence of boron carbide at the Mo/Si MIS interface suppresses the formation of silicides. As a result, interfaces become sharper.

7.2.1 Ion polishing (smoothing). Very smooth interfaces reducing the diffuse X-ray scattering to a minimum are usually obtained by ion deposition for polishing each layer. In this case, a separate ion gun is used [242] (with ion energies up to a few hundred electron-volts) either after or during ion deposition to help the deposited atoms to achieve local positions corresponding to the minimal energy of the system [28, 36, 243].

A strong smoothing of surfaces resulting in sharper interfaces was first demonstrated for the RhRu/C MIS [244] and W/C multilayers [245]. Shortly after that, ion-beam smoothing was performed for the Mo/Si short-period MIS [246] and for EUV radiation coatings [247]. At first, most of the smoothing experiments were performed with Ar^+ ions. However, small argon ions can deeply penetrate into layers and therefore can damage the interface under the layer. This effect can be reduced by using ions of larger sizes, such as Kr^+. The use of Ar^+ and Kr^+ was studied in [248, 249]. The authors of [250] showed that the sputtering of 400 eV Kr^+ ions (with the use of sputtered 10 eV Sc and Cr atoms) is the best compromise for the optimized growth of defect-free, dense, smooth layers with sharp interfaces [11].

7.2.2 Working pressure. It was found in [251] that the roughness of an Si/C MIS surface increased from 0.13 to

0.29 nm with increasing pressure from 0.13 to 0.52 Pa, while the reflectivity of samples with 20 bilayers gradually decreased from 2652 Pa and the reflectivity of samples with 20 bilayers gradually decreased from 26.3% to 18.9%. The maximum reflectivity, equal to 33.2%, was obtained for a sample with 50 bilayers prepared at a working pressure of 0.13 Pa.

An increase in the roughness with increasing the argon working pressure was also observed during the growth of Mo/Si [252], W/Si [253], and Nb/Si [254] MISs.

7.2.3 Substrate. The reflectivity and imaging properties of MISs substantially depend on the substrates on which they are deposited. Along with the general requirement of atomic smoothness, some specific requirements are imposed on substrates related to the specific features of problems solved with the help of MISs.

The simplest model assumes that the substrate roughness makes the same contribution to film roughness independently of the film thickness. At the same time, this simple model ignores the fact that the 'memory' of the substrate roughness gradually disappears during film growth [255]. In general, the contribution of the substrate roughness depends on time and decreases with film growth [256].

The specification of substrates, methods of their manufacturing, and metrology for lithography, synchrotron sources, FELs, solar physics, and astronomy are presented in review [257]. Materials for substrates with an ultralow expansion coefficient, silicon and silicon carbide substrates, are presented. Some new materials for substrates and their manufacturing technologies are also discussed.

7.2.4 Bias potential. In the absence of a bias potential applied to a substrate during the deposition of a silicon layer, the interface roughness tends to develop from the substrate to the surface of a multilayer stack, finally forming a columnar structure inside the Mo/Si MIS. If a negative bias potential (up to -200 V) is applied to the substrate during the deposition of a silicon layer, this favors the formation of smoother interfaces and improves the layer morphology [258]. When a negative potential is applied to the substrate during deposition, the width of the intermediate zone in the MIS can decrease, as was found in [259], because the intense bombardment of the growing film by Ar ions can efficiently increase the mobility of an adatom, reducing the roughness between layers [260].

7.2.5 Substrate temperature. Experiments on the optimization of Mo/Si MIS parameters [172, 181, 261, 262] revealed the dependence of the interface roughness on the substrate temperature, the minimal roughness being observed in the temperature range from 120 to 250 °C.

The dependence of the interface roughness on the substrate temperature (Fig. 8) has a sharp minimum with the value of 0.33 nm for a multilayer Mo/Si film deposited at 215 °C [262]. The authors explain this minimum by the competition of two processes. As the substrate temperature is increased, smoothing caused by surface diffusion occurs, which results in a decrease in the interface roughness. The second process — improved temperature mixing — increases the roughness and dominates at temperatures above 215 °C.

Cryogenic Mo/Si MIS cooling was performed in [252, 263, 264]. The temperature dependences of the roughness and

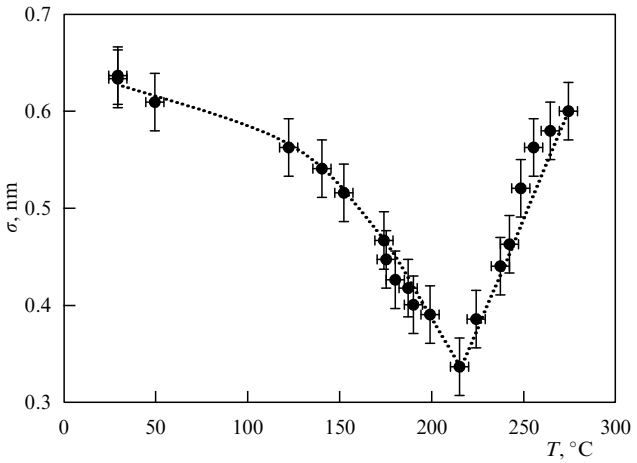

Figure 8. Interface roughness measured as a function of the substrate temperature during MIS deposition [262].

reflectivity of multilayer Mo/Si mirrors deposited by the electron-beam evaporation method were studied in [263] and [252]. The authors found that the roughness of mirrors deposited at the substrate temperature of -155 °C was lower than that of mirrors deposited at room temperature. This result can be explained by the fact that the nucleation rate at the initial film-growth stage is higher at the lower temperature, resulting in an increase in the number of nucleation centers and therefore leading to smoother interfaces. This mechanism is consistent with the smoothing effect observed at considerably higher temperatures [11].

7.3 Methods for reducing stress

Strict requirements for MIS optics in the soft X-ray and EUV regions demand the minimization of deformation caused by multilayer film stress. Such a deformation can produce substrate bending or film stratification. However, the stress should be diminished or compensated without decreasing the MIS reflectivity.

The compression stress of optimized Mo/Si MISs is usually -420 MPa, while the tensile stress of Mo/Be MISs is $+330$ MPa [56]. This stress level is high enough to deform, for example, the image of projection optics in a lithographic system.

Experimental studies of stresses showed that the stress in a film can be controlled by deposition conditions such as nitrogenization [265, 266], argon pressure [56, 251, 267], and even pressure in a vacuum system before deposition [267].

Other methods for reducing stresses in multilayer Mo/Si films include annealing after deposition [56, 225, 268–270], the introduction of anti-stress buffer layers [56, 271–273], and changing the fraction γ [56, 274–277].

A study of annealing upon the deposition of Mo/Si [56, 271] at 200 °C showed that the stress decreased by 70%, as for annealing after deposition. However, the reflectivity decreased by 3.9% compared to 1.3% for annealing after deposition. This means that, if annealing is performed on films, it should be done after the multilayer deposition.

The decrease in the residual stress of Mo/Si and Mo_2C/Si multilayers upon annealing was studied in [225]. Slow thermal annealing (1 °C min^{-1}) reduced the stress from -520 MPa to zero by heating Mo/Si samples to 310 °C. However, the reflectivity decreased by approximately 3–4%. On the other hand, the stress in the Mo_2C/Si MIS can be reduced from

−490 MPa to zero by annealing without a considerable decrease in the reflectivity.

Multilayer Mo/B_4C structures deposited at low sputtering pressures have a high compression stress. Zero stress can be achieved at 360−370 °C, but annealing at < 200 °C is sufficient for reducing stress by ∼ 40 % [270]. This stress relaxation is accompanied by an increase in the multilayer period by ∼ 0.02 nm and a decrease in the normal-incidence reflectivity by <0.5 %. The multilayer period remains stable up to ∼ 600 °C, while the internal stress changes sign.

Because the ability of substrates to withstand thermal annealing was unknown, the authors of [270] decided to develop a reliable nonthermal method to reduce stress so as not to produce irreversible deformation of the multilayer optics. For example, to reduce the stress by decreasing the reflection coefficient, each of the Mo layers in [272] was replaced by an Mo/Ru/Mo sandwich.

By using the technique of deposition of an amorphous silicon buffer layer for the Mo/Be MIS and an Mo/Be buffer layer for the Mo/Si MIS, multilayers with almost zero stress and the reflectivity decreased by less than 1% were obtained [271]. In this way, Mo/Be MISs with the reflection coefficient 68.7% at 1.4 nm and Mo/Si MISs with the reflection coefficient 66.5% at 13.3 nm with stresses of less than 30 MPa were manufactured.

The stress in MISs can change with time, even at room temperature. It is important that multilayer optical devices be stable with time. For Mo/Si with the Mo/Be buffer layer, the stress changed from −28 to +3 MPa and the reflection coefficient decreased by approximately 0.4% for more than 300 days. For Mo/Be with an amorphous Si buffer layer, the stress changed from −23 to −3 MPa and the reflection coefficient decreased by 12.8% for the same time [271].

If the stress in layers A is compressing and in layers B is tensile, then the stress in a multilayer stack can be either compressing or tensile (or zero) depending on the relative thickness of the layer.

In [275], W/Cr films obtained by magnetron sputtering in argon consisted of 20–50 nm thick W layers deposited on 5–10 nm thick Cr layers. The deposition conditions were controlled such that the W layers were compressed, while the CV layers were stretched such that for the specified selection of the layer thickness satisfying the requirement for optical contrast, the stress in the bilayer was minimized by balancing the stresses in two metal layers.

It was found in [276] that the stress increased almost linearly with increasing γ (Fig. 9). The stress sign changed at $\gamma \sim 0.5$. This value divides the γ range into two parts: the lower values lead to compression stress and the higher values give tensile stress.

It is known that the Mo/Si MIS reflectivity depends on the parameter $\gamma = d_{Mo}/d$ and reaches its maximum value in the spectral region 13–13.7 nm for $\gamma \approx 0.42-0.44$ [276]. A change in the ratio of thicknesses of the Mo and Si layers can be used to reduce stresses to almost zero levels for $\gamma \approx 0.6$ (see Fig. 9), but with a strongly reduced reflection ($R \approx 54-57$ %) [276]. A change in the molybdenum fraction in MISs obtained by electron-beam evaporation leads to a result similar to that for coatings produced by magnetron sputtering, although for different values of γ. In [277], the Mo/Si MIS with 30 periods, $d = 7$ nm, and $\gamma = 0.7$ was manufactured. The multilayer 'softened' stack with the high reflection coefficient (69%) demonstrates a lower stress equal to −33 MPa. It was also found that the number of periods of such an MIS does not affect the stress value in the range of N from 20 to 50, while a change in the d interval only slightly affects the residual stress.

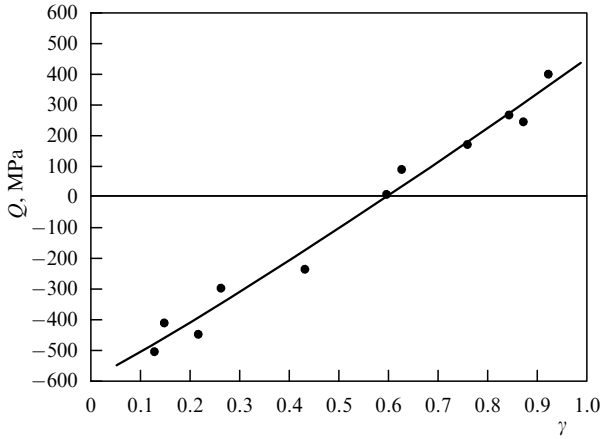

Figure 9. Stress Q in Mo/Si MISs obtained by magnetron sputtering depending on the Mo fraction γ at the fixed bilayer thickness of 6.8 nm [276].

7.4 Methods for increasing the radiative, temporal, and corrosion stability

The contamination of optical surfaces due to the interaction of X-rays with atoms of background vacuum gases decreases the lifetime of the optics and is one of the main problems with multilayer optical devices used with intense X-ray sources such as high-power lasers, synchrotron radiation sources, or plasma sources in EUV lithography instruments. The main problem in the development of commercial EUV lithography is increasing the lifetime of the Mo/Si MIS projection optics. The Mo/Si MIS should have a high radiative stability and the maximum possible reflectivity in the normal-incidence geometry. A serious problem with usual highly reflecting Mo/Si MISs with an upper silicon layer is the considerable deterioration of the reflectivity caused by carbonization and oxidation of the surface silicon layer under the action of radiation [278].

It was shown that molecular contamination is caused by secondary electrons induced by EUV radiation. The lifetime of projection optical devices is restricted by the precipitation of carbon and its oxidation. It was shown that carbon, for example, can be removed using radiofrequency purification by oxygen or hydrogen [279], atomic hydrogen [280, 281], or ozone [282, 283] with an insignificant decrease in the reflectivity. The best solution to this problem is to avoid carbon precipitation. This idea was proposed by the authors of [284], who showed that carbon precipitation was considerably suppressed in a medium containing a mixture of water vapor and ethanol. Oxidation is more problematic, because an oxide cannot be removed after its formation. Oxides also strongly absorb EUV and, for example, a small increase of 1.5 nm in the oxide-layer thickness reduces the reflection coefficient by 1.6%, which is the durability criterion for projection optics. Therefore, oxidation-stable protective layers are required for increasing the lifetime of multilayer optical devices. Various materials based on multilayer Mo/Si films with certain optical constants were proposed for protective layers in [285]. However, aside from the optical properties, these materials should form a continuous layer up to a few nanometers in thickness, stable against oxidation in the water vapor environment, and also a sharp smooth interface with the material under the layer. Moreover, the

protective layer should be stable not only against oxidation but also against the purification method for removing the carbon contamination and should not reduce the reflection coefficient [11].

The Ru, Rh, RuO_2, TiO_2, and ZrO_2 layers proposed for protecting the Mo/Si MIS surface were studied in [8, 286, 287]. Ru is widely used as an anticorrosion layer because it combines relatively high optical transparency with a sufficient stability against oxidation in the environment containing H_2O in large amounts [50, 278]. The microstructure, morphology, and stability of Ru and RuO_2 in oxidizing and reducing media were studied in detail in [288].

The growth of multilayer Pd/B_4C structures with small d intervals is accompanied by the appearance of extremely compressing stresses and the formation of defects. The stress, together with substrate surface defects, generates cracks and other defects in the layers. The presence of oxygen in the environment causes the depletion and oxidation of boron, which in turn results in considerable damage to the layered structure for several days. A protective SiO_x layer can decelerate the degradation process by orders of magnitude [74].

The stability of various nanostructure coatings for different applications irradiated by high-power X-rays has been studied by many authors [289–298].

The mechanism of Mo/Si MIS damage caused by 13.5 nm radiation from a plasma source generated by a table-top laser was studied in [291–293]. For multilayer Mo/Si mirrors, two damage regimes were observed upon irradiation by nanosecond pulses: for the 0.8 J cm^{-2} radiation density, 'spot-like' damage is observed, which transforms into a crater for the energy density of ~ 1.7 J cm^{-2} [291]. It was shown that the Mo/Si efficiency could be improved by adding a protective layer such as Pd or B_4C. Indeed, Pd and Mo have similar thermal and mechanical properties, which reduces stresses and improves the Mo/Si MIS stability. A protective B_4C layer also reduces damage due to its high hardness, low X-ray absorption, and the stable interface with a silicon layer under it [292].

The Mo/Si MIS damage mechanism caused by a single femtosecond pulse was studied in [294–298]. The damage mechanism in this case is different because the material has no time to melt under the action of a short femtosecond pulse. For the radiation energy densities Φ from 40 to 125 mJ cm^{-2}, two types of damage were observed. The first is characterized by the formation of a 'smooth' crater. The crater area exactly corresponds to the damage area and its depth varies from a few nanometers for Φ slightly higher than the damage threshold to more than 30 nm for $\Phi \approx 65$ mJ cm^{-2}. For $\Phi > 65$ mJ cm^{-2}, the second damage type is observed: the crater is much deeper and increases to 70 nm for $\Phi \sim 125$ mJ cm^{-2}. In addition, a mound forms in the middle of the crater [294]. For $\Phi < 17.5$ mJ cm^{-2}, no substantial changes are observed in the MIS character, even under irradiation for 60 s. For $\Phi \approx 42.5$ mJ cm^{-2}, considerable changes in reflection characteristics were always observed, even for a 10 ms exposition [298].

8. Methods providing spectral purity

Spectral contamination in the long-wavelength range is a common problem with many X-ray sources. Plasma sources produced by a laser discharge have a broad emission spectrum from the EUV to the visible range, sometimes extending to the IR range [299]. High-harmonic generation sources emit a harmonic train of waves beginning from the fundamental wave of a laser [206]. In astronomic observations in the EUV region, the longer-wavelength background is also present [300]. Thus, the spectra of these sources contain emission in the UV, visible, and even IR spectral ranges outside the transmission band of MISs. This radiation can be reflected even by a single layer, and therefore it is difficult to filter it with the help of a standard multilayer mirror. Outside the MIS transmission band, this radiation is also reflected by a multilayer mirror to the optical system, where it can decrease the spectral resolution, the detection sensitivity, and the image processing quality [301] or create a thermal load problem [302].

Undesirable long-wavelength radiation can be suppressed with transmission multilayer filters. However, such filters have a relatively low transmission coefficient in the EUV range and degrade under a thermal load or variable pressure [303, 304]. Several new schemes of spectral filters integrated with MISs developed recently [11, 305] demonstrate a high suppression of undesirable wavelengths along with a considerably higher efficiency.

The commonly accepted method for suppressing UV radiation is based on the use of an anti-reflection coating [306]. The method is based on the destructive interference of reflections from the upper and lower surfaces of the coating: if the two reflections have equal amplitudes and opposite phases, the undesired radiation is transferred into the substrate. The optical properties of Si_3N_4 in the wavelength range 100–200 nm are favorable for the design of a single-layer anti-reflection coating. In [307], a 7 nm thick Si_3N_4 film was deposited on an Mo/Si MIS. The relatively weak absorption in Si_3N_4 at 13.5 nm restricts the reflectivity loss by only 4%, the reflection coefficient for UV radiation decreasing fivefold. In the wavelength range above 200 nm, materials with a low reflectivity and high transparency in the EUV region are not available.

The authors of [308] manufactured a single-layer anti-reflection coating for multilayer Mo/Si mirrors. A thin $Si_{0.52}C_{0.16}N_{0.29}$ film 20 nm in thickness prepared by electron-beam combined deposition of silicon and carbon with N^+ ion implantation during growth suppresses the reflection of UV radiation in a broad band with the maximum coefficient of 195 at 285 nm.

As a rule, the MIS reflection band has a small but finite width, and this can be a serious disadvantage when several spectral lines fall into the transmission band. The design, realization, and characteristics of an innovative MIS with high reflectivity along with the suppression of one of the two adjacent spectral lines are presented in [86, 309]. A key optical element is an optimized multilayer anti-reflection coating deposited above the MIS, which preserves the reflection coefficient at the specified wavelength and at the same time suppresses reflection at a particular undesirable wavelength. Similarly to the MIS, the coating structure consists of a sequence of absorber and spacer layers, which can be made of the same materials as the MIS or different materials. A periodic MIS with a high reflectivity creates a standing wave in the structure for both wavelengths. If the coating layers are designed such that the standing wave antinodes for the undesired wavelength are very close to the absorbing layer, a considerable decrease in the intensity at the undesired wavelength can be achieved [72, 86, 309].

The authors of [72] demonstrated the possibility of using a Pd/B_4C coating to obtain a high peak reflection coefficient

for the third harmonic ($3\lambda \approx 20.1$ nm) and to suppress the fundamental harmonic in one configuration or, alternatively, using this coating in another configuration to provide a high peak reflection coefficient only for the fundamental harmonic. In the first case, the absorbing layer (the Pd layer) is always located near a node of the third harmonic of the standing wave and at the antinode of the fundamental harmonic with the subsequent appearance of a fundamental reflection. It was shown in [310] that the combination of a multilayer La/B_4C mirror and an additional multilayer anti-reflection coating of the same composition provides both a high third-harmonic suppression coefficient equal to 356 and a peak reflectivity of 53.4% at a wavelength of 6.7 nm.

Anti-reflection coatings for suppressing UV radiation are quite attractive; however, they cannot be used to suppress long-wavelength IR radiation because the large thickness of the coating required for this purpose would lead to unacceptable losses in EUV radiation intensity.

IR reflection by standard multilayer Mo/Si mirrors is mainly caused by scattering from metal Mo. The first step for reducing the IR reflection is the replacement of Mo by a different material, such that the multilayer stack, still reflecting EUV, would at the same time be transparent to IR radiation. This is nontrivial, because materials with a high electron density having reasonable reflection coefficients in the EUV range are usually metals or metal compounds such as Mo, Mo_2C, Ru, or Zr, which are opaque to IR radiation. A multilayer mirror for EUV radiation proposed in [311] has a low reflection coefficient in the IR region at a CO_2 laser wavelength of 10.6 μm. The mirror is based on a multilayer coating containing alternating layers of diamond-like carbon and silicon, for which the reflection coefficients were 42.5% and 4.4% in the respective EUV and IR ranges.

An elegant design of hybrid multilayer mirrors was developed in [45, 32, 313] (Fig. 10). Here, the MIS operates as a Bragg reflector for EUV radiation, and at the same time it forms an IR anti-reflection coating together with a metal layer located under it. The MIS is perceived by the incident IR radiation as a homogeneous medium. In this case, the wave intensity reflected from the whole structure is equal to the sum of intensities reflected from the MIS external surface (R_1) and the MIS/metal layer interface (R_2) [312] (Fig. 10a). If the total MIS thickness is optimized, a phase shift between R_1 and R_2 equal to 180° can be produced and therefore an IR reflectivity close to zero can be achieved. In [312], the authors used the B_4C/Si MIS as a reflector transparent to the IR radiation and a 10 nm thick Mo film between the Si substrate and the B_4C/Si stack. The maximal EUV reflectivity was measured to be 45% along with the IR radiation suppression by more than two orders of magnitude.

A similar (but more flexible) construction based on LaN/B was proposed for a possible lithographic system operating at a wavelength of about 6 nm [313] (Fig. 10b). The IR reflection from this structure is determined by the interference of waves reflected from the upper surface (R_1), the interface between the MIS and a phase-shifting layer (R_2), and the interface between the phase-shifting layer and substrate (R_3). Because the total width of the LaN/B MIS is fixed by the construction for optimal EUV reflectivity, the phase-shifting layer width should be adjusted to achieve destructive interference at $\lambda = 10.6$ μm for minimizing the reflectivity at this wavelength.

This design provides a certain freedom in the choice of materials for the phase-shifting layer, including amorphous

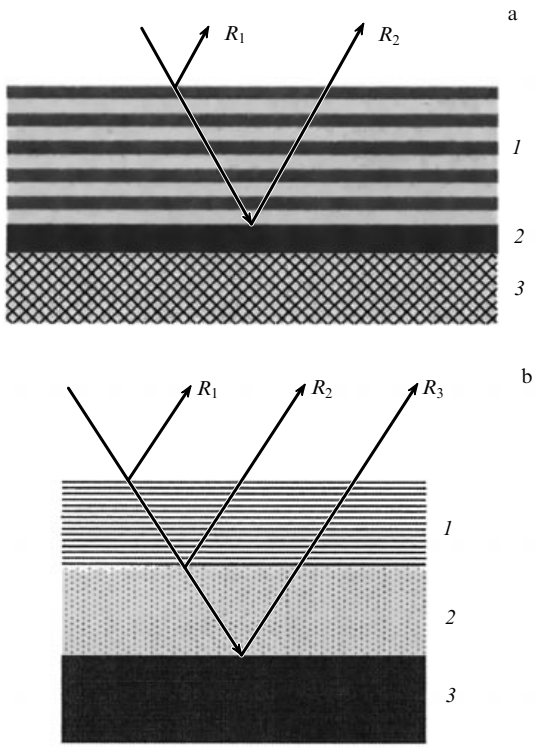

Figure 10. Sketches of hybrid multilayer mirrors: (a) *1* — B_4C/Si MIS, *2* — Mo film 10 nm in thickness, *3* — substrate [312]; (b) *1* — LaN/B MIS, *2* — phase-shifting SiO_2 layer, *3* — substrate [313].

Si, Ge, and SiO_2, which are compatible with the extremely smooth growth conditions required for efficient MIS applications. In this particular study, SiO_2 was chosen because of the commercial availability of ultrasmooth SiO_2 coatings.

SiC was proposed as a substrate material providing a high optical contrast at $\lambda = 10.6$ μm, with materials such as Si and SiO_2 proposed for a phase-shifting layer.

9. Applications of periodic MISs

9.1 Monochromators

Compared to crystal monochromators, multilayer monochromators offer certain advantages. First, a multilayer period (and hence the wavelength of a reflected photon) can be made arbitrary, in particular, for reflecting wavelengths above 1 nm, which is impossible for crystals. Second, the typical transmission bandwidth of MISs is one to two orders of magnitude larger than that of crystals. Thus, a multilayer monochromator reflects the greater part of the energy spectrum, resulting in an increase in the integrated intensity of diffracted X-rays. Third, some geometric shapes can be readily fabricated with the help of multilayer materials deposited on profiled (for example, bent) substrates. The fact that parameters of multilayer structures such as the bilayer period (the d interval), the ratio of thicknesses γ, the combination of materials, and the number of layers can be chosen arbitrarily allows somewhat adapting the spectral range of the transmission band to the requirements of a particular study [314]. Another advantage is that different MISs can be deposited in the form of several strips on one substrate to cover a broad spectral range with the optimal efficiency [315–319].

A high reflectivity in two spectral regions can be obtained with the help of so-called periodic two-stack multilayer coatings containing two MISs with different periods, deposited one on another [320, 321].

The number of multilayer monochromators used in synchrotrons all over the world is constantly increasing, although is still limited compared to the number of crystal monochromators. Optical systems are being developed or used for various industrial applications [314].

9.2 Focusing

In 1981, Henry, Spiller, and Weisskopf [322] reported the fabrication of the first multilayer device on a second-order surface. MISs are usually deposited on an ellipsoid for focusing or on a paraboloid for collimating a beam. For example, a parabolic multilayer mirror proved to be efficient for application in the powder diffraction method [15, 16, 323]. However, when the divergence of the incident beam is large and the size of the optical apparatus required for the beam interception becomes impractically large, the meridional focusing concept gives way to the sagittal focusing concept.

A sagittal focusing monochromator consisting of two multilayer structures producing a spatially broadened broadband X-ray beam from a synchrotron radiation source is described in [324]. This monochromator consists of two W/B_4C MISs with a period of 25 Å on an Si substrate. The second module is mounted on a sagittal bent device, which can dynamically change the bend radius of a multilayer mirror for beam focusing (Fig. 11a). This device provides the control of the X-ray beam size to obtain the best matching between the detection region and object sizes for efficient data collection. The broad energy band, along with the sagittal focusing, provides the best possible photon flux for time-resolved experiments. The authors of [325] state that sagittal focusing MISs with a fixed bent radius provide an additional ten-fold increase in the flux density.

The mirror in a Hamos spectrometer is a cylindrical mica crystal 20 mm in radius with W/B_4C or Cr/Sc MISs deposited on it (Fig. 11b). The radiation source and the recording plane lie on the cylinder axis. Different wavelengths diffract in different regions of the MIS surface and are focused at different points on the spectrometer axis. The first studies with MISs in a focusing Hamos spectrometer [326] have shown that they are promising for applications in the X-ray and EUV spectroscopy of low-intensity sources. In the range $8 \leqslant \lambda \leqslant 25$ Å, they can compete with crystals as dispersion elements of focusing spectrometers. In the EUV range, inaccessible to the application of crystals, focusing spectrometers based on MISs can be used instead of conventional grazing-incidence diffraction spectrometers [327].

In 1948, Kirkpatric and Baez [328] presented one of the first practical solutions to the X-ray optical visualization problem. They managed to overcome the absence of conventional refracting lenses and showed that a pair of cylindrical mirrors can provide the 'point-to-point' focusing required for imaging. The Kirkpatric–Baez microscope uses two cylindrical mirrors for the successive focusing of X-rays in two perpendicular planes (Fig. 12a) for a grazing incidence in the energy range 100 eV–10 keV. Compared to paraboloid and ellipsoid surfaces, the fabrication of cylindrical surfaces is much simpler [329]. When a multilayer coating is used, the microscope has a high spatial resolution and high X-ray focusing efficiency [330–333].

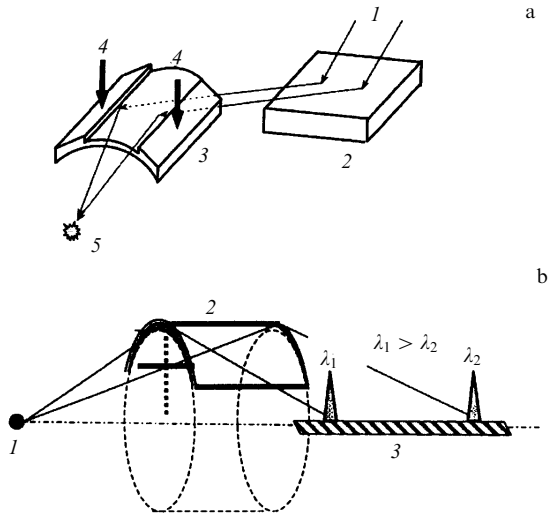

Figure 11. (a) Diagram of an MIS monochromator. The incident collimated X-ray beam *1* is reflected from a plane multilayer mirror *2* at the Bragg angle and focused on the spot *5* of a sagittally bent MIS *3*. Arrows *4* show the load applied for mechanically bending the MIS substrate [324]. (b) Schematic of a focusing X-ray Hamos spectrometer: *1* — X-ray source, *2* — sagittally bent mica crystal with the MIS deposited on it, *3* — linear detector [327].

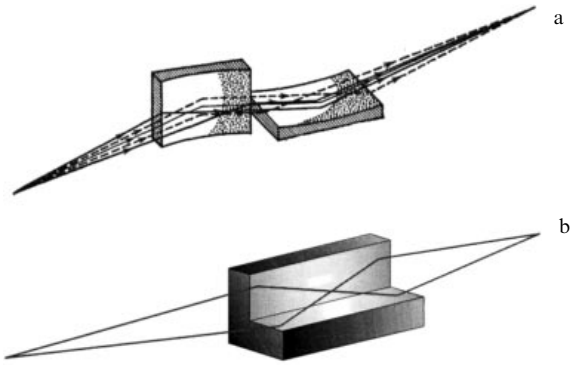

Figure 12. Kirkpatric–Baez 'point-to-point' focusing schemes: (a) classical and (b) confocal [125, 334].

An important particular case of the Kirkpatric–Baez optical device is a symmetric system with two 'side-to-side' mirrors (Fig. 12b), which is also called confocal. Such a system has an effective aperture four times larger than the classical Kirkpatric–Baez system, which is one of its advantages [320]. In addition, because the optical apparatus is much more compact than in the classical scheme, both mirrors can be preliminarily adjusted and connected, while the adjustment degrees of freedom can be independent of each other [15, 16, 334].

9.3 Normal-incidence optical instruments

As in visible light optics, the diffraction-limited resolution of an X-ray optical element is given by [335]

$$D_{\text{diff}} = \frac{0.44\lambda}{\text{NA}}\,, \tag{13}$$

where $\text{NA} = n \sin\eta$ is the numerical aperture, η is the aperture angle, n is the refractive index of a medium where radiation propagates, and λ is the radiation wavelength.

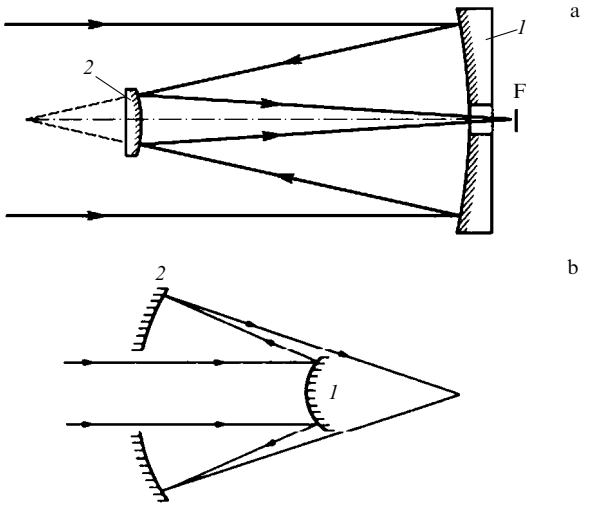

Figure 13. (a) Path of rays in a Cassegrain telescope: *1* — primary focusing mirror, *2* — secondary scattering mirror, (F) — focus. (b) Path of rays in a Schwarzschild objective: *1* — secondary focusing mirror, *2* — primary scattering mirror.

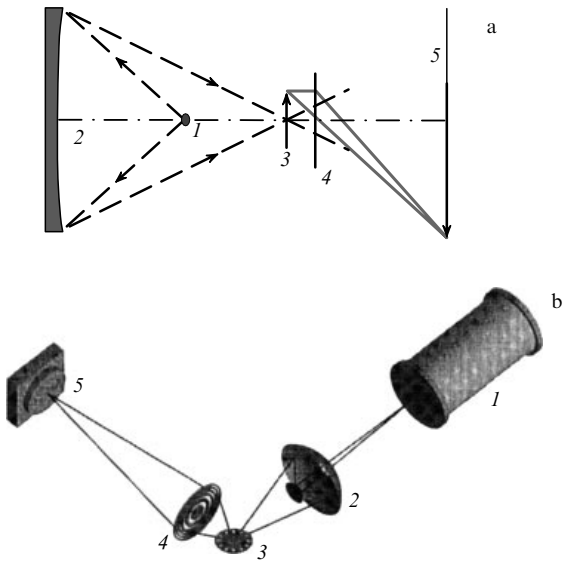

Figure 14. (a) Diagrams of X-ray microscopes: *1* — plasma laser source, *2* — condenser (multilayer spherical mirror), (b) Schwarzschild objective: *3* — sample, *4* — objective (Fresnel zone plate), *5* — magnified sample (a) image/(b) detector [342, 343].

Therefore, the advantages of normal-incidence multilayer optical instruments over grazing-incidence ones are the larger numerical aperture, i.e., an increased aperture ratio and improved spatial resolution, as well as the comparative simplicity of manufacturing, resulting in the high quality of produced images. The normal-incidence multilayer optical instruments have a smaller number of aberrations than the grazing-incidence ones, thereby providing a better angular resolution in a much broader field of view.

X-ray normal-incidence spherical mirrors are used in telescopes [100, 336–338], microscopes [2, 339–345], spectrometers [346–349], and EUV lithography [7, 11, 44, 350, 351].

Periodic multilayer coatings operating near the normal incidence can be deposited on superpolished mirror substrates, for example, in a Cassegrain telescope containing a large primary concave mirror and a small convex secondary mirror (Fig. 13a). The use of normal-incidence mirrors in optical instruments improved their spectral resolution to tenths of an angular second, reduced the exposure time by more than an order of magnitude, and diminished the size and weight of the instruments, which is very important for space experiments.

In the case of telescope mirrors for solar visualization, several EUV emission lines are imaged in one telescope, with each of the mirrors divided into several sectors, each tuned to one particular wavelength and covered with a suitably chosen pair of materials [100]. For example, the EIT instrument uses four separate multilayer structures deposited on the matched quadrants of primary and secondary telescope mirrors. A rotating mask makes it possible to use only one quadrant of the telescope for solar illumination at any time. All the multilayers are fabricated from alternating molybdenum and silicon layers [336]. The SUVI instrument is a generalized Cassegrain telescope having six different wavelength channels located on one mirror and tuned to six narrow spectral bands centered at 93.9, 131.2, 171.1, 195.1, 284.2, and 303.8 Å [338].

To produce magnified images of microobjects with a submicron spatial resolution in the soft X-ray and EUV spectral regions, microscopes using Fresnel zone plates [352] as an objective and a multilayer mirror as a condenser [343, 344] were developed and built (Fig. 14a). A normal-incidence multilayer condenser offers a number of advantages, including high data collection efficiency, distinct spectral selectivity, and a high numerical aperture.

To obtain the high resolution for a large field of view with the help of spherical mirrors, it is necessary to use two reflections, as in the Schwarzschild objective [2, 339–341, 345] (Fig. 13b). The advantage of such systems over single-reflection devices is also that the object and its image are located on different sides of the focusing system, which simplifies their use [2]. The Schwarzschild configuration also allows creating an optical instrument without spherical aberrations, astigmatism, or comas. The Schwarzschild objective offers all the advantages of normal-incidence mirrors based on MISs. It combines a large field of view with a submicron spatial resolution [339, 341]. The Schwarzschild system can be used in microscopes as an objective [341] and a condenser [342] (Fig. 14b).

Highly reflecting normal-incidence multilayer mirrors for the EUV spectral range attract considerable interest because the projection lithography is promising for the development of the next generation of lithographic instruments for manufacturing semiconductor structures with a resolution of 70 nm or better [44]. In lithography, the image of a mask is transferred onto the surface of a silicon plate by a system of normal-incidence multilayer mirrors. The mask is an Mo/Si MIS coated with an absorbing film with the pattern of an integrated circuit [353]. Most of constructions consist of a system of Bragg reflectors with a constant MIS thickness (Fig. 15). A relatively large number of mirrors in the projection part is necessary to obtain a high resolution along with a large enough field of view. MISs give the maximum theoretical reflectivity $R \sim 0.75$ for Mo/Be and $R \sim 0.73$ for Mo/Si. However, for optical systems with several reflectors, the output optical intensity sharply decreases and can decrease to 6–10% of the input intensity. Therefore, obviously, even an increase in the reflectivity of one mirror

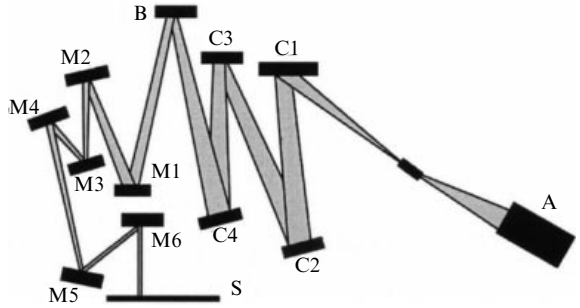

Figure 15. Diagram of an EUV lithographic instrument: (A) — radiation source, (B) — mask, (S) — silicon plate, (C) — condenser mirrors, (M) — projection mirrors [351].

by 1–2% would provide a considerable increase in the aperture ratio of the total optical system [11, 351]. This, in particular, explains the desire of researchers to increase the MIS reflectivity as much as possible.

9.4 Polarization properties

The polarization of X-rays is usually measured in a standard way by using two optical elements azimuthally turned about the radiation propagation direction: a polarizer for introducing a phase delay of 90° and a linear polarization analyzer. It is well known that because the refractive index is close to unity in the X-ray range, Brewster's angle at which a p-polarized wave is not reflected is in fact close to 45° (we note that this conclusion follows from (7)).

Theoretical and experimental investigations showed that multilayers can be used as efficient polarizers and analyzers in the soft X-ray region [181, 354–372]. There are two types of multilayer polarizers and analyzers. One of them operates in the reflection geometry and the other in the transmission geometry. Because the latter changes neither the propagation direction nor the spatial position of the beam, it can be easily introduced into any X-ray optical setup. Aside from polarization properties, these films also have phase-shifting properties. MISs can produce a phase shift between the s- and p-components of the field near the Bragg angle if this angle is close to Brewster's angle. The reason is the difference in the width of reflection curves for the s- and p-polarized radiation [3, 157].

Due to interference of the incident and reflected s-polarized field in MISs used in transmission, the field intensity is concentrated in separating layers for angles slightly smaller than the Bragg angle or in the absorbing material for angles slightly exceeding the Bragg angle [373]. This results in a large phase delay or phase advance for the s-component, whereas the p-component is not affected by this resonance because of the closeness to Brewster's angle [357, 371].

Thus, MISs can be used to obtain quarter-wavelength plates for soft X-rays and EUV radiation.

10. Aperiodic MISs

Periodic MISs have relatively narrow spectral transmission bands ($\Delta\lambda/\lambda \sim 0.01-0.1$), which makes them, first of all, an efficient tool for constructing quasi-monochromatic spectral images. Along with periodic multilayer structures, of interest are also aperiodic structures capable of satisfying criteria other than the achievement of a high reflection coefficient in a broad spectral range without changing the radiation incidence angle.

Beginning with the pivotal paper by Lee [374], it has become clear that changing the period of a multilayer structure over depth or along the surface, allows changing the reflection curve so as to impart unusual properties to multilayer mirrors, the properties not inherent in conventional periodic multilayer mirrors.

Aperiodic MISs have a huge potential inaccessible to periodic MISs. Aperiodic MISs can be optimized to obtain the maximum integrated reflectivity or the maximum uniform reflectivity in the specified wavelength range or specified incidence angle range to obtain the maximum reflectivity at the same or several wavelengths, for polarization in all broad wavelength ranges for a fixed grazing incidence angle, etc. [12, 14, 375–377].

10.1 Depth-gradient MISs

One of the methods for increasing MIS transmission is simply to decrease the number of reflecting bilayers.

This approach for the hard X-ray range faces the problem of a rapidly reducing reflectivity. The more efficient variant is a change in the d interval such that X-rays with different energies or different grazing angles are reflected into different depths of the MIS. The obvious possibility of broadening the transmission band is the creation of a multilayer structure with a period gradually changing over the MIS depth. In this case, shorter-wavelength X-rays are reflected from deeper layers of the structure, because they are usually absorbed more weakly (Fig. 16).

A well-known method for constructing aperiodic MISs uses the gradual decrease in the d interval by a power-law function [378]

$$d(j) = \frac{a}{(j+b)^c}\,, \tag{14}$$

where $j = 1, 2, \ldots$. The coefficients a, b, c, the number N of layers, and the thickness fraction γ should be optimized to obtain the desired reflectivity as a function of the photon energy. For gradient MISs, the parameter γ can be a constant or slowly varying quantity in order to optimize the reflection efficiency, i.e., to find the best compromise between the constructive interference and photoelectric absorption [138].

The solution of the inverse problem of projecting a multilayer mirror with a reflectivity $R_0(\varphi)$ between incidence angles $\varphi_{\max}$ and $\varphi_{\min}$ is usually based on the minimization of the merit function [379]:

$$\begin{aligned} &\mathrm{MF} = (\Delta\varphi)^{-1}\int_{\Delta\varphi}\left[R_0(\varphi) - R(\varphi)\right]^2 \mathrm{d}\varphi\,,\\ &\Delta\varphi = \varphi_{\max} - \varphi_{\min}\,, \end{aligned} \tag{15}$$

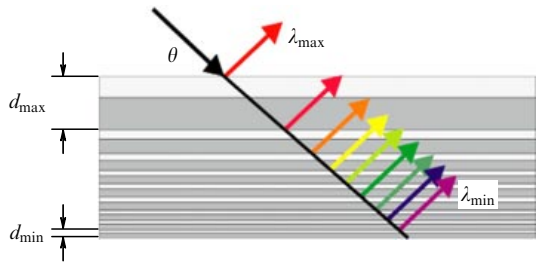

Figure 16. Principal setup of a depth-gradient MIS [116].

which characterizes the root-mean-square deviation of the calculated reflectivity profile $R(\varphi)$ from the assumed reflectivity. The thicknesses of deposited layers are assumed to be independent variables. If the energy interval is specified instead of the angular interval, $\Delta\varphi$ in (15) should be replaced by ΔE.

After the choice of $d_{\min}$ and $d_{\max}$ for a given MIS, the parameters of the power-law function are determined by minimizing the merit function via scanning the three-dimensional space of parameters: the number N of bilayers, the exponent c, and the ratio γ of the thickness of a heavy element to the d interval. This uniquely determines constants a, b, and c [119].

For example, the authors of [380] grew a gradient W/Si MIS containing 150 bilayers with layer thicknesses in the range $d = 3.33-29.6$ nm and $\gamma = 0.415$. The bilayer thickness distribution for this film was described by the expression

$$d_j = \frac{10.27}{(j-0.991)^{0.225}}\,, \qquad j = 1\,,\ldots,150\,, \tag{16}$$

where d_j is the thickness (in nm) of the jth bilayer, the uppermost layer corresponding to $j = 1$.

Requirements for the optical constants of elements of gradient MISs depend on the optimization criterion used and differ in general from those for periodic mirrors. Nevertheless, pairs of materials giving the best results for periodic MISs are typically also good for aperiodic structures. Gradient MISs with any desired reflectivity profile $R(\lambda)$ or $R(\varphi)$ were designed using several theoretical approaches (see, e.g., [144, 378, 381–388]). We note that all the approaches give a nonmonotonic oscillatory dependence of the layer thickness on depth, although the desired profile of the reflection curve is very simple (for example, constant) (Fig. 17). In fact, as shown theoretically in [144, 384], the monotonic dependence of the period on the depth always leads to a strongly oscillating reflection curve. The reverse is also true: an MIS providing a smooth reflection curve is always characterized by a nonmonotonic change in the period, which often oscillates with depth. As shown in [380, 386, 390], small deviations (by a fraction of an angstrom) of the layer thickness from the nominal value can explain the deformation of the reflection curve observed in experiments.

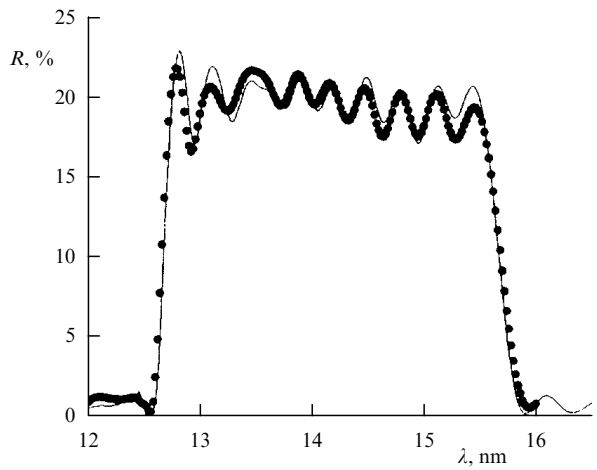

Figure 17. Calculated (solid curve) and measured (dots) reflection coefficients of an aperiodic multilayer polarizer consisting of 100 Mo/Si bilayers [389].

Variations in the layer thickness in broadband MISs should be minimized at the projecting stage. This is important not only for the ease of control of the layer thickness during manufacturing but also for preserving the invariable layer structure along the whole stack and thereby close to the desired design. This problem was solved by Kozhevnikov et al. by using a new merit function including a factor restricting the variation value of the layer thickness [391]. They designed MISs providing an almost constant reflectivity of 50% in the interval of incidence angles $0°-16°$ ($\lambda = 13.5$ nm), with the change in layer thickness being no more than 0.39 nm. However, the more practical solution of the problem would be the creation of a broadband MIS with the thickness of the layers varied as weakly as possible. Then the internal structure of layers could be expected to vary insignificantly. As a result, the deviation of the layer thickness from the calculated value would be smaller, even with the use of methods for controlling the deposited mass [391].

Broadband MISs are used as polarization elements [392–398] and in spectroscopy [375, 376, 399–402], astronomy [124, 403–406], and X-ray optics [317, 407–409].

The generation and measurements of ultrashort electromagnetic pulses are at the forefront of modern physics. The pulse duration restricts the temporal resolution of experimental studies of the time evolution of various processes. Attempts to generate laser pulses as short as possible are stimulated by the desire to investigate fast molecular processes [410]. Recently, we have witnessed great progress in the generation of single pulses a few hundred attoseconds in duration ($1\,\text{ac} = 10^{-18}$ s) [411, 412]. Such pulses can be obtained during the interaction of high-power femtosecond laser pulses with a gas jet; the ionization of atoms in a laser field generated the spectrum of laser harmonics extending to the X-ray region.

To filter out attosecond pulses from the high-harmonic spectrum and to direct and focus them, special equipment is required. Short pulses have a broad spectral range, and hence the transmission band of an optical element should be no less than the spectral range of the pulse. Therefore, broadband mirrors can be used to reflect attosecond pulses. It was shown that properly manufactured gradient MISs can be used to compress chirped pulses [29, 250, 347, 377, 413–421]. (A chirped pulse is one with the wavelength monotonically varying within the pulse [422]). The idea of using a depth-gradient MIS to compress a chirped pulse is based on the fact that different frequency components of the pulse are reflected at different depths in the MIS, where radiation locally satisfies the Bragg condition. Multilayers located at different depths produce a difference in the path length and therefore a phase difference between different spectral components of the pulse, allowing the pulse to be compressed.

Simulations in [413] showed that an optimized gradient MIS can reduce the pulse duration from 260 to 90 as. The possibility of generating short pulses with durations of 170–130 as were demonstrated in the energy range 75–130 eV using multilayer Mo/Si structures with the reflectivity of 5–10% [416, 417, 421].

The authors of [418] experimentally demonstrated the compression of chirped pulses to theoretical durations in the range 50–47 as. Moreover, their theoretical study showed that gradient MISs can provide efficient pulse compression in a very large range of incident angles.

10.2 Lateral-gradient MISs

If the reflection coating for X-ray optical elements is made of multilayer films (especially for a large receiving angle), the uniform layer thickness causes chromatic aberration. This aberration can be eliminated using a lateral gradient MIS [335, 423–426].

The Bragg law in such structures [formula (6)] holds at each point of their surface, and the numerical aperture increases compared to a periodic MIS, which in turn results in an increase in the aperture ratio and the diffraction resolution limit [335]:

$$D_{\text{diff}} \approx 0.88\left(\frac{1}{d_{\min}}-\frac{1}{d_{\max}}\right)^{-1}. \qquad (17)$$

In the case of the parabolic or elliptic curvature of a lateral gradient MIS, the initially diverging quasimonochromatic X-ray beam can be transformed into a parallel or focused beam. The replacement of a periodic structure by a lateral gradient structure widens the possibilities of efficiently using optical elements such as a condenser [427], a Schwarzschild objective [42], and Kirkpatric–Baez mirrors [9, 425, 428–433].

Parabolically bent gradient MISs, so-called Goebel mirrors, opened new applications as X-ray optical devices. A Goebel mirror is a gradient MIS on a parabolically bent substrate transforming a diverging beam into a parallel quasimonochromatic beam using the linear focus of an X-ray tube (Fig. 18a). The Goebel mirror can be considered the most successful among different types of gradient MISs because it is the most flexible and has many applications [67, 423, 434–436]. For example, a parallel beam can be connected with other X-ray optical elements such as a monochromator [434] or fulfill the functions of a collimator in a diffractometer [435] (Fig. 18b).

In the case of a primary polychromatic beam with a small angular divergence, a planar lateral gradient MIS can be used as a monochromator [437] or a linear polarizer [438] with the possibility of energy detuning by directing the X-ray beam to different parts of the surface with different d intervals (Fig. 19).

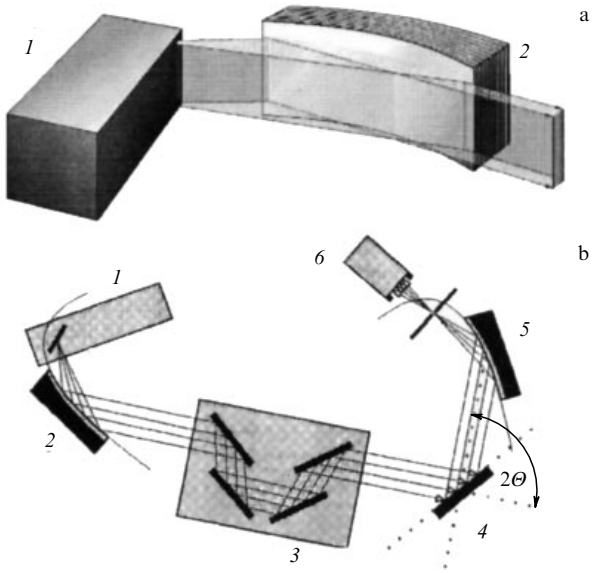

Figure 18. (a) Goebel mirror *2* combined with an X-ray tube with a linear focus *1* [67]. (b) Setup of a 'moderate resolution' diffractometer [435]: *1* — X-ray tube, *2* — collimator (Goebel mirror), *3* — crystal monochromator, *4* — sample, *5* — analyzer (lateral-gradient cylindrical multilayer mirror, *6* — detector.

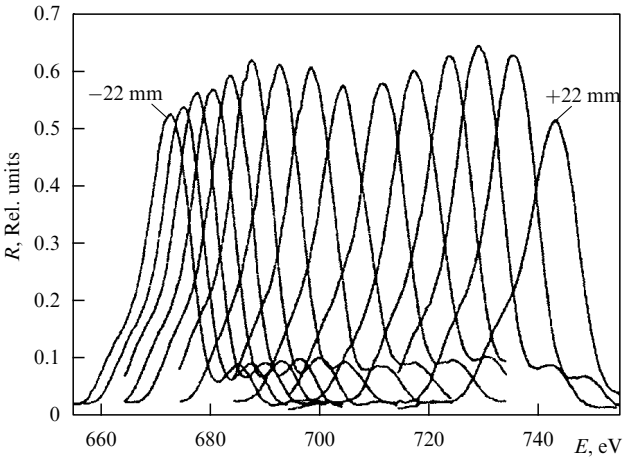

Figure 19. Differential reflection curves obtained by moving an X-ray beam over the Fe/Cr MIS surface with an interval of 3.1 mm along the gradient direction [438].

10.3 γ-gradient MISs

It is known [2] that for general MIS models with absorbing layers, the gradual change in the distribution ratio over the mirror depth from $\gamma = 0.3-0.4$ on the surface to $\gamma = 0.5$ near the surface can increase the peak reflectivity. The authors of [439] showed that if the ratio γ is corrected for each bilayer to provide the maximum increase in the reflectivity, a gradual transition occurs from the ideal quarter-wavelength structure near the substrate to thinner absorbing layers near the surface. Their optimized design has demonstrated a much higher reflectivity than the periodic structure.

The Mo/Si MIS was optimized in [350] by gradually changing the layer thickness through the stack, whereas the period width remained nominally constant at 6.8–7.0 nm. The value of d_{Mo} near the substrate was $d_{\text{Si}} \approx 3.5$ nm, changing to $d_{\text{Mo}} \approx 2.7$ nm and $d_{\text{Si}} \approx 4.2$ nm near the surface. The important feature of the layer profile is that the value of γ equal 0.4 is preserved over the first 20 periods near the surface and then gradually increases to 0.5 near the substrate, the last value being close to the ideal value of $\lambda/4$.

The optimized Cr/Sc/Mo MIS proposed in [440] had a gradient distribution of the layer thickness over depth within the nominal optical period: the components of the first three-layer stack had the widths Sc (3.3 nm)/Mo (2.7 nm)/Cr (3.7 nm). 'Transparent' Sc and absorbing Mo layers in the next three-layer stacks became thinner. Beginning with the fifth three-layer stack, the layer thickness became constant. The last six three-layer stacks were Cr (3.6 nm)/Sc (4.3 nm)/Mo (1.4 nm), while the upper chromium layer was 3.3 nm in thickness. This MIS had a constant periodic thickness of 9.8 nm for reflecting soft 310 eV X-rays at the grazing angle of 77.2°. The peak height and spectral width of the measured reflectivity were 27.4% and 35 eV, which are suitable for the condenser optical instruments of broadband high-intensity soft X-ray sources.

For gradient layers, γ can also be made a slowly varying quantity to optimize the reflection efficiency, i.e., to find the best compromise between constructive interference and photoelectric absorption [138].

11. Narrowband multilayer optical devices

In the development of new methods for increasing the sensitivity and the signal-to-noise ratio, aside from the necessity of increasing the reflectivity of mirrors, the problem appears of how to synthesize coatings with extremely narrow transmission bands. Such MISs should provide a spectral resolution between those of 'conventional' MISs ($\Delta\lambda/\lambda \approx 2\,\%$) and crystals ($\Delta\lambda/\lambda \approx 0.01\,\%$) to perform investigations in the fields of microimaging, fluorescence analysis, and crystallography with much higher photon fluxes and adequate resolution.

The transmission band of a semi-finite MIS can be described by the very simple expression [18, 235]

$$\frac{\Delta\lambda}{\lambda} = \left|\mathrm{Re}\,(\chi_A - \chi_B)\right| \frac{\sin(\pi m\gamma)/\pi m}{\sin^2\theta}\,, \qquad (18)$$

which is, of course, approximate because it does not contain absorption effects and is valid only when the extinction depth is considerably shorter than the mean free path of soft X-rays restricted by absorption in the MIS material. Nevertheless, this expression clearly points to methods that can be used to increase the spectral resolution of MISs.

First, because expression (18) contains the Bragg reflection order m, the spectral resolution can be improved by increasing the diffraction order. Higher orders in the EUV range were used in [441], where the authors demonstrated a narrow transition band 0.077 nm wide at $\lambda = 13.5$ nm.

The second way to improve the spectral resolution is to replace the absorbing material with some light, weakly absorbing material to decrease the permittivity jump at the interface affecting the resolution. One solution is the deposition of carbon/carbon coatings. This means that both components of the structure are carbon, but its density in alternating layers should be different [7, 442].

A carbon/carbon material system is of special interest due to its low absorption coefficient in a broad spectral range and the possibility of depositing C layers with different modifications, i.e., different optical properties. Simulations of C/C multilayers [443] showed that the reflection coefficient R (Cu Kα radiation) exceeding 80% and the resolving power $\lambda/\Delta\lambda \approx 600$ can be achieved for a C/C MIS with $d = 3$ nm and $N = 1000$. Experimentally, the resolving power $\lambda/\Delta\lambda \approx 91$ was obtained for the period thickness of 1 nm and the number of periods up to 500.

The authors of [444] used low-contrast Al_2O_3 and B_4C for $E = 8$ keV to measure the transmission band equal to 0.27% with the reflectivity of 40% of an Al_2O_3/B_4C multilayer with $N = 800$ and $d = 26$ Å.

Another approach to improve the spectral resolution consists in decreasing the thickness of layers of a strongly absorbing material. As γ is decreased, the transmission band width decreased to the minimal possible value $(\Delta\lambda/\lambda)_{\min} = (\mathrm{Im}\chi_B/\sin^2\theta)$ determined by the maximum possible penetration depth of the wave in the MIS and restricted by the absorption of radiation in a weakly absorbing material of the structure [19].

By simulating variations in γ, the authors of [445] have found that multilayer mirrors consisting of 30 Mo and Si bilayers with the interval $d = 9.1-9.5$ nm give a transmission band width $\leqslant 3$ eV for the energy $E = 70$ eV if γ decreases to 0.2 or less. The peak reflectivity decreases from 54% for $\gamma = 0.3$ to 50% for $\gamma = 0.2$ (in the absence of interface roughness). It was pointed out that the peak reflectivity considerably decreased for γ below 0.2.

By combining expressions (9) and (10), the authors of [18] obtained expressions for the s-polarization showing that the increase in the resolving power is inevitably related to a decrease in the peak reflectivity and vice versa:

$$\frac{\lambda}{\Delta\lambda} = K\left(\frac{\sin^2\theta}{\mathrm{Im}\,\chi}\right)\frac{1-R}{1+R}\,, \quad \gamma < \gamma^*\,, \quad R_0 = 0.1-0.4\,. \qquad (19)$$

Here, K ranges from 0.4 to 0.7 for MISs with $|\mathrm{Re}\,(\chi_A - \chi_B)/\mathrm{Im}(\Delta\chi)| \leqslant 1$ and from 0.7 to 1 for $|\mathrm{Re}\,(\chi_A - \chi_B)/\mathrm{Im}(\Delta\chi)| \gg 1$.

One of the methods for reducing the transmission bandwidth without a noticeable decrease in the reflectivity is based on the formation of a lamellar multilayer diffraction grating (lamella is a thin plate) in a common MIS because, in this case, the penetration depth of soft X-rays can increase [446, 447] simply due to removing part of the MIS material [255].

12. Multilayer reflection diffraction gratings (MDGs)

Diffraction gratings are the most popular tool used in soft X-ray spectroscopy for obtaining monochromatic soft X-rays, because natural crystals cannot be used in this spectral region. Before 1980, diffraction gratings were used only in the grazing incidence geometry because a very weak polarizability of all materials results in a vanishingly low reflectivity for an almost normal incidence. These gratings are characterized by a small entrance aperture and a narrow transmission band, as well as by considerable aberrations that significantly restrict the spectral resolution in the case of focusing gratings. The situation drastically changed after the advent of MISs, which efficiently reflect soft X-rays at any angle up to the normal incidence. The first tests of multilayer diffraction gratings (MDGs) were described in [448, 449].

The use of MDGs often does not have an alternative for obtaining high spectral resolution and a high aperture ratio. For soft X-rays, MDGs are the alternative to crystals traditionally used in this X-ray range. Moreover, unlike crystals, which are 'monochromatic' elements, MDGs are 'polychromatic' elements. This MDG feature is related to the dispersion properties of a common grating and allows using or recording the entire broadband spectrum of incident X-rays, which is useful in studying nonstationary processes.

Another advantage of multilayer gratings is the possibility of controlling their transmission band to optimize the flux and resolution in accordance with experimental requirements. This makes their applications in spectroscopy and X-ray monochromatization very broad.

Thus, the creation and study of new X-ray optical elements, such as MDGs providing a high spectral resolution along with a large aperture ratio, not only broaden the spectral range and choice of study objects but also allow using new approaches in X-ray investigations, which are not feasible with conventional X-ray elements [450–454].

There are several types of amplitude reflection (Bragg) MDGs, which are shown schematically in Fig. 20.

A diagram of a lamellar MDG is shown in Fig. 21. X-rays are incident on the grating at an angle θ_0 and are reflected at an angle θ_p to the pth diffraction order. The grating has the period D and consists of A/S MIS lamellas with the period d and width L.

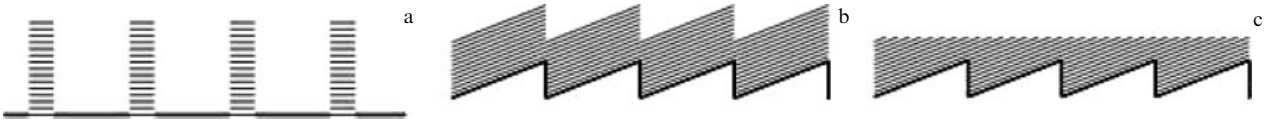

Figure 20. Different types of reflection MDGs: (a) lamellar, (b) profiled, (c) truncated [452].

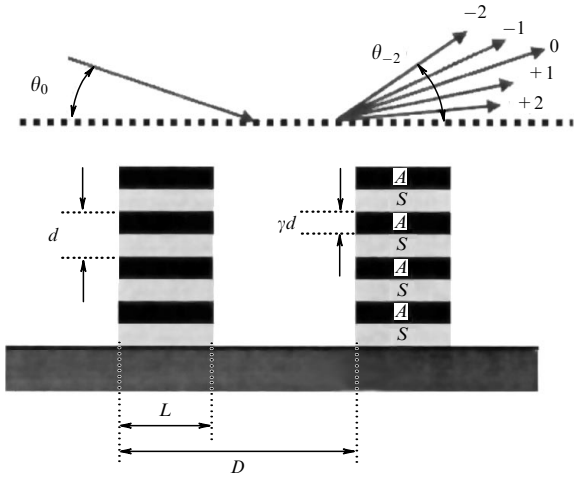

Figure 21. Schematic presentation of a lamellar MDG [451].

In the hard and soft X-ray ranges (small incidence angles and the extinction length greatly exceeding the grating period D), multilayer lamellas become semi-transparent to X-rays. As a result, each X-ray photon is reflected not from one but from a few dozen multilayer lamellas simultaneously. In this case, diffraction conditions for the reflection of X-rays from the MIS layers and the diffraction grating are satisfied simultaneously [457]:

$$\frac{\lambda m}{d} = \sin\theta_0 + \sin\theta_p\,, \tag{20}$$

$$\frac{\lambda p}{D} = \cos\theta_0 - \cos\theta_p\,, \tag{21}$$

where $p = 0\,,\ \pm1\,,\ \pm2\,,\ldots$ and $m = 1\,,2\,,3\,,\ldots$ are diffraction orders for the grating and the MIS.

The simultaneous satisfaction of conditions (20) and (21) for two of three variables ($\theta_0\,,\theta_p$, and λ) determines the diffraction maxima of the MIS. These conditions are similar to the Bragg conditions for radiation diffraction in crystals.

12.1 Lamellar MDGs

It was shown theoretically and experimentally in pioneering paper [456] that the spectral resolution can be improved by MIS etching, because the penetration depth of X-rays can be increased after removing part of the absorbing material from the MIS by etching, which leads to a so-called lamellar MDG [451, 457–463]. An improvement in the MDG resolution in the soft X-ray range is typically accompanied by a decrease in the reflectance caused by undesired diffraction from the grating. In a simple MIS, the total output X-ray intensity is concentrated in one zeroth-order beam. However, the primary monochromatic plane wave diffracts from the MDG to different diffraction orders (see Fig. 21), thereby reducing the efficiency for each individual order [458, 464]. To reduce these diffraction losses, based on the developed rigorous theory of X-ray diffraction from lamellar MDGs, a single-mode MDG operation regime was proposed in which the incident wave efficiently excites a single wave of a certain diffraction order [20, 255, 451, 465, 466]. The necessary condition for MDG operation in the single-order regime is quite obvious: the angular width $\Gamma\Delta\theta$ of the Bragg peak of the MDG (where Γ is the ratio of the lamella width to the grating period and $\Delta\theta$ is the Bragg peak width for the MIS) must be small compared to the angular distance d/D between adjacent diffraction peaks:

$$\Gamma D\Delta\theta \ll d\,. \tag{22}$$

Then the higher diffraction orders 'fall out' from the receiving angle $\Delta\theta$ of the Bragg reflection from the MIS, and the incident beam efficiently excites only one diffraction order, substantially improving the MDG reflectance. In the semi-infinite and strictly periodic MIS approximation, the single-mode regime improves the spectral resolution by $1/\Gamma$ times, while the peak reflectance is preserved at the level of usual MISs because the etched structure operates not as a diffraction grating but simply as an MIS in the grazing incidence geometry (Fig. 22). On the contrary, the depth H of penetration into the structure and hence the MDG resolution increase because of the inverse proportionality to Γ [20, 255]:

$$H = \frac{\lambda\sin\theta}{\pi\Gamma\chi}\left\{\left(1-y^2\right)\left[1+y^2\left(\frac{\mathrm{Re}\,\Delta\chi}{\mathrm{Im}\,\Delta\chi}\right)^2\right]\right\}^{1/2},$$
$$y = \frac{\sin(\pi\gamma)}{\pi[\gamma + \mathrm{Im}\,\chi_B/\mathrm{Im}\,\Delta\chi]}\,. \tag{23}$$

A comparison of expressions (10) and (23) shows that the use of a single-mode MDR provides a considerable improvement in spectral resolution compared to common MISs without reducing the peak reflection coefficient (Fig. 23). Therefore, lamellar MDGs can be used to produce monochromatic soft X-rays. They have been applied in spectroscopy [461, 463, 467–471] and for producing monochromatic X-rays [458, 464, 472, 473].

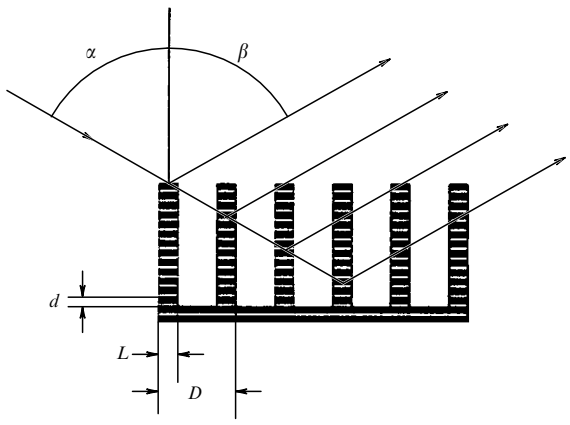

Figure 22. X-ray diffraction from an MDG in the single-mode regime [450].

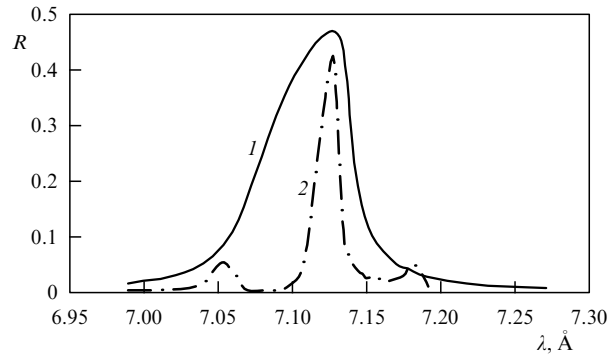

Figure 23. Calculated reflectance for the Mo/C MIS with a period of 2.5 nm (*1*) and an MDG with $\Gamma = 1/3$ and 500 Mo/C MIS bilayers (*2*) [435].

12.2 Profiled MDGs

A further increase in the resolving power and efficiency of multilayer X-ray optical devices is based on the use of a profiled grating. As a rule, a sawtooth profile is used. In the domestic literature, such an MDG is called a multilayer blazed grating. Because a sawtooth profile resembles stairs, we here use the term 'MDG echelette' (echelette (French) from echelle, stairs). An MDG echelette is manufactured by the deposition of an MIS on a sawtooth substrate [474–485] (Fig. 20b). A sawtooth relief is usually produced by moist anisotropic etching [479, 483] or by multilevel electron-beam lithography [486].

Grating equation (20) shows that diffraction-order angles depend only on the period of grooves but not on their shape. The diffraction pattern intensity can be changed if the reflecting parts (step surfaces) are inclined in the diffraction plane at an angle of φ_p to the grating generatrix in order to scatter the greater part of radiation in the preferred direction (and to a particular diffraction order p). In this case, the beam diffracted from the grating and the beam reflected from the steps are reflected in the same direction (Fig. 24).

The grating equation can be rewritten in the form [474]

$$p\lambda = 2D \sin\varphi_p \sin\theta\,, \tag{24}$$

where $2\varphi_p$ is the angle of deviation of the diffracted X-ray beam from the zeroth order ($2\varphi_p = \theta_p - \theta_0$). The combination of Eqn (24) and the Bragg formula $\lambda m = 2d\sin\theta$ for the MIS gives the correspondence equation for the MIS and grating:

$$pd = mD \sin\varphi_p\,. \tag{25}$$

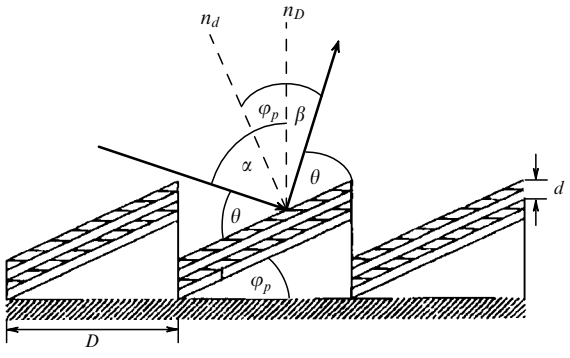

Figure 24. Diffraction geometry of an MDG echelette. α: incidence angle, β: diffraction angle for the m-th order, φ_p: blaze angle, θ: Bragg angle, D: grating period, d: interval of multilayer coating, n_D: normal to the grating plane, n_d: normal to the MIS plane [480].

The angle φ_p is an important characteristic of the echelette grating and is called the blaze angle. This is the angle at which the grating seems to blaze, i.e., specular reflection from the working sides of the steps is observed.

The main disadvantage of echelette gratings is the low diffraction efficiency caused by screening: each tooth of the 'saw' overshadows the adjacent one, such that only some of the reflecting strips are illuminated.

It was shown by numerical and experimental methods [450, 482] that the efficiency limit (the Maystre–Petit factor [487]) for classical diffraction can be exceeded by 2–2.5 times in higher orders when the MDG period is shorter than the X-ray decay length: the dense multilayer periods become semi-transparent to soft X-rays, thereby reducing the overshadowing effect. In addition, the relative diffraction efficiency decreases with increasing the asymmetry $b = \cos\alpha/\cos\beta$ and therefore with increasing the blaze angle φ_p relating the incidence angle α to the diffraction angle β: $\alpha = \beta + 2\varphi_p$.

The geometrical parameters of MDG echelettes can be chosen to provide operation in one order, when only one diffracted wave is excited, whereas waves in all other orders are suppressed. As a result, the grating efficiency can reach the reflectance of a usual MIS. This conclusion is also valid for broadband MDG echelettes based on gradient MISs [488].

For photons with energies from 1 to 5 keV, echelette gratings with multilayer coatings are perfectly suitable for suppressing higher diffraction orders. For this purpose the authors of [485] used a 2000 l/mm echelette grating with a blaze angle of 0.84° coated with a 20-layer Cr/C MIS with the d interval of 7.3 nm. The efficiency of the MDG echelette was 35% and 55% at 2 and 4 keV, respectively.

In [476], a 3000 l/mm echelette grating with a blaze angle of 2.78° had a multilayer Mo_2C/Si coating. The efficiency peak measured at the second negative diffraction order for an incidence angle of 5.6° at a wavelength of 15.79 nm was 29.9%. The echelette grating with a multilayer Mo/Si coating and a blaze angle of 1.9° manufactured in [489] had the diffraction efficiency of 36.2% in the second negative order for the incidence angle of 10° at the wavelength 13.62 nm.

An echelette grating coated with 20 Mo/Si bilayers had a diffraction efficiency up to 33% in the third order for the incidence angle 11° and the wavelength 14.18 nm [478]. A new record of the diffraction efficiency was achieved for a 2525 l/mm MDG echelette optimized for the second diffraction order [481]. Its absolute efficiency at a wavelength of 13.4 nm reached 52.0%.

Thus, MDG echelettes with high groove densities and high diffraction orders can provide good spectral resolution at a high enough reflectance, which is of special interest for modern spectroscopic methods [490, 491].

12.3 Truncated MDGs

There are two main methods for achieving ultrahigh spectral resolution in the soft X-ray range. The first is the use of high-order diffraction with low groove density MDGs (for example, with an MDG echelette), and the other is the use of the first diffraction order in ultrahigh groove density gratings. MDGs of the second type can be fabricated by cutting and polishing an MIS with a large number of periods

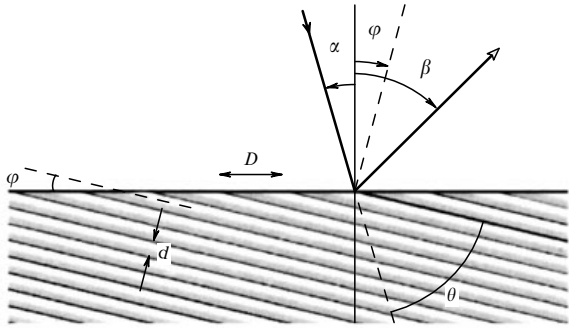

Figure 25. Geometry of diffraction from a truncated MDG. α: incidence angle, β: diffraction angle, φ: truncation angle, θ: Bragg angle, D: grating period, d: interval of the multilayer coating.

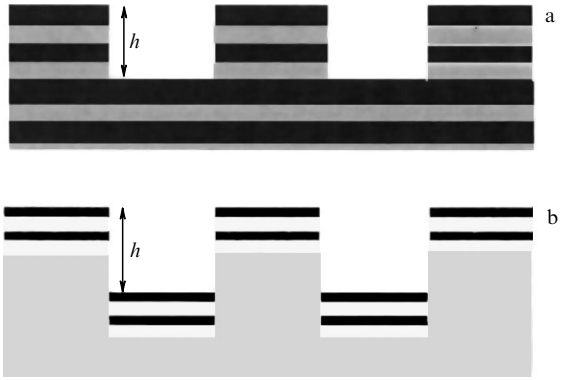

Figure 26. Phase lamellar MDGs fabricated (a) by MIS etching and (b) by MIS deposition on a diffraction grating.

$N = 1000-2000$ truncated at a small angle φ to its plane (Fig. 25). In this case, a grating with the period $D = d/\sin\varphi$ is formed on the cut, and the MDG equation takes the form [422, 492]

$$m\lambda = D(\sin\beta - \sin\alpha) = 2D\sin\varphi\sin\theta\,. \qquad (26)$$

We note that such a structure and an asymmetrically truncated crystal monochromator have similar dispersion properties. Moreover, there is an obvious similarity between an MDG echelette and a truncated MDG [493]. Indeed, the truncated MDG is in fact a first-order MDG echelette. This is confirmed by calculations of the efficiency, which show that like the MDG echelettes, truncated MDGs demonstrate a very high efficiency approaching the MIS reflectance [494].

Compared to the MDG echelette, the truncated MDG should have higher reflectance because of the decrease in the overshadowing effect. In addition, the truncated grating should provide a more accurate diffraction pattern without overlapping diffraction orders, which would be typical of an MDG echelette with diffraction in a very high order. The properties of the truncated MDG were considered in detail in [422, 453, 494]. The first truncated MDGs based on the Mo/Si MIS were fabricated a few years ago and used to study laser plasma spectra in the wavelength range 12–30 nm [493, 495]. The high efficiency of such MDGs in the EUV range was demonstrated in experiments [422, 494]. However, the maximum number of periods of a grating produced by the truncation of an MIS deposited on a plane substrate is equal to the number of deposited layers, which restricts both the spectral resolution and the MDG size due to limitations of the deposition technique. These restrictions were eliminated by the deposition of an MIS on a substrate echelette followed by polishing, removing part of the coating, and forming an inclined cut [496] (Fig. 20c). For example, the authors of [492] reported the fabrication of a truncated MDG with an efficiency of $\sim 30\,\%$ at a wavelength of 13.2 nm, with an echelette grating with the period 36.95 nm and the blaze angle 10.5°, coated by an Mo/Si MIS consisting of 3200 bilayers with a period of 6.7 nm and $\gamma = 0.5$.

12.4 Phase MDGs

To increase the efficiency of lamellar MDGs, phase gratings have been developed [495, 497–500]. Unlike 'classical' lamellar MDGs, they use the reflection of X-rays from the upper part of a lamella and from the 'bottom' of a groove. For this purpose, an MDG is fabricated by etching to a certain depth h or, alternatively, a lamellar grating is covered by an MIS with the groove depth h (Fig. 26).

Radiation reflected from the bottom and surface of a lamella interferes constructively if $h = q\lambda/2(\cos\alpha + \cos\beta)$, where q is an odd integer, α is the incidence angle, and β is the diffraction angle. In the ideal case of normal incidence, the zeroth and even orders are completely suppressed if this condition is satisfied and if grooves and lamellas have the same width (i.e., $\Gamma = 0.5$). Then 40.5% of the primary X-ray radiation diffracts to each of $+1$ and -1 orders, while intensities in higher odd orders decrease as m^{-2}, where m is the diffraction order number [501].

The authors of [497] reported the first attempt to fabricate a lamellar phase MDG operating near normal incidence in the EUV region. In [499], an Mo/Si MIS was deposited on an ion-etched lamellar grating with 1200 grooves per 1 mm. The groove depth was 61 Å and $\Gamma = 0.41$. For the incidence angle of 46° and s-polarized radiation at 13.6 nm, the respective efficiency in the $+1$ and -1 diffraction orders was 11% and 9%. In [500], a phase MDG consisting of a lamellar grating coated with an Mo/Si MIS is described. The grating had 2400 grooves per mm, and the groove depth and width were 40 Å and 2080 Å. The multilayer coating was optimized to have the normal reflection peak at a wavelength of about 15 nm. The peak efficiency of the grating for the incidence angle was 16.3% in the $+1$ order and 15.0% in the -1 order. The zeroth-order efficiency was 1/40 due to the excellent choice of groove depth and width.

12.5 Alternative MDG

Among all types of multilayer gratings, an alternating version of MDG, shown schematically in Fig. 27, can be fabricated quite easily by the deposition of a periodic multilayer structure on a lamellar substrate with a lamella depth d, which is part of the multilayer period of the structure [502]. An alternating MDG is a grating with a double periodicity on the nanometer scale. The grating period on the surface plane is the step p of the lamellar grating, in the vertical direction, and the MIS period is $2d$. Therefore, alternative MDGs have properties similar to a crystal, with the advantage of the free choice of periodicity. In the ideal case shown in Fig. 27, the lamellar profile is covered by an ideal MIS, and all the layers have a thickness equal to the grating groove depth. The two materials of the MIS in the cross section are checkered [503].

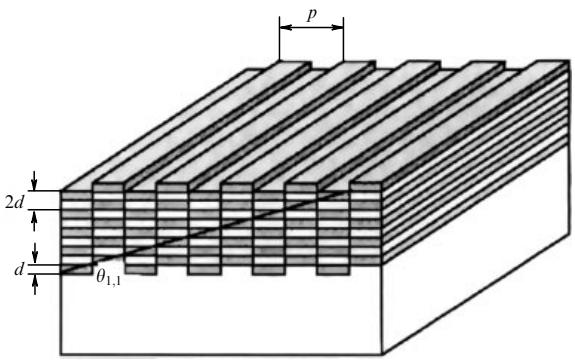

Figure 27. Model of an alternative MDG. The inclined straight line shows the orientation of the Bragg plane (1, 1) [505].

The diffraction efficiency of the alternating MDG reaches its maximum if the groove width is equal to half the grating period ($\Gamma = 0.5$) and the MIS parameters, first and foremost the parameter γ, are chosen to provide the maximum reflectance of usual MISs. Among the advantages of alternating MDGs are the relatively simple fabrication of the lamella relief on the grating substrate compared to the sawtooth relief of the echelette substrate and the possibility of considerably decreasing the diffraction efficiency of the zeroth and all even orders [504].

Alternating MDGs were recently designed and fabricated for applications in X-ray equipment [502–506].

12.6 Spectral purity function MDG

Phase lamellar MDGs can be used to filter undesired radiation (for example, IR radiation) [14, 507–509].

Because the angular separation of diffraction orders is proportional to λ/D, when a grating with a large period of tens of micrometers is used, the out-of-range long-wavelength radiation from the specular direction diffracts at a large angle to higher orders and can be blocked with an aperture. In this case, EUV radiation is concentrated around the zeroth order, providing high efficiency. However, the zeroth order of undesired radiation propagates in the same direction. The zeroth-order diffraction efficiency is [508]

$$R_0 = R_{\text{tot}}\left(1 + 2\Gamma\left(\Gamma - 1\right)\right)\left(1 - \cos\left(\frac{4\pi h}{\lambda}\right)\right), \qquad (27)$$

where R_{tot} is the total reflected intensity. It follows from (27) that the zeroth-order intensity vanishes only for $\Gamma = 0.5$ and $h = \lambda/4 + m\lambda/2$, where $m = 0, 1, 2, \ldots$. Thus, the reflection of undesired radiation from the upper and lower surfaces of a groove leads to destructive interference. The maximum suppression wavelength can be tuned by varying the grating height h.

A phase MDG of this type was used in [510] to suppress the reflection of UV radiation. A multilayer grating with a reflection coefficient of 64% operating at a wavelength of 70 nm provided a 30-fold suppression of radiation at 280 nm.

The phase lamellar MDG with a period of 100 μm operated at a wavelength of 10.6 nm in [508] provided a 70-fold suppression of IR radiation, with a reflectance of 61%. This method for suppressing undesired radiation was used in a condenser mirror for EUV lithography [507, 511].

Although the lamellar phase shift grating and antireflection coatings considered above provided efficient suppression of radiation outside the band, the suppression efficiency is still limited by destructive interference.

UV radiation can be reflected from one Si layer a few nanometers in thickness. Si also weakly absorbs in the EUV region. Therefore, the broadband absorption of UV radiation can be realized by replacing the rectangular shape of grating grooves by a profiled shape. Various structures can be used, such as an echelette grating [512, 513] or a pyramid. In this case, the undesired radiation is scattered into higher diffraction orders from inclined faces in a broad wavelength range, while EUV radiation is still reflected by the MIS.

The complete suppression of the 100–400 nm UV radiation band along with the reflection coefficient of 56.2% in the EUV region was demonstrated by using silicon pyramids deposited on a multilayer Mo/Si structure [514] (Fig. 28a). Because absorption in all materials, including silicon, cannot be ignored in the EUV range, part of the EUV radiation intensity is lost due to absorption in pyramids. However, if a pyramid consists, for example, of an Mo/Si MIS, the UV radiation is still suppressed, but the EUV radiation is reflected by pyramids and the lower layers of the MIS. A multilayer pyramidal structure demonstrated almost the same UV suppression as silicon pyramids and provided a high EUV radiation efficiency of 64.7% [305].

UV radiation suppression is mainly caused by diffraction from periodic faces of pyramids and destructive interference between reflection from the upper plane region and from the valley between pyramids, with most of the UV power scattered into higher orders. The structure can be optimized by selecting structural parameters, including the height h, period p, bottom width a, and upper plane width w. The influence of various structural parameters and detailed optimization of the structure were discussed in a paper describing silicon pyramids [514].

We note that the intensity of radiation reflected from pyramids is distributed around the direction of specular reflection from facets in a broader angular region (within a few orders) than in the case of an echelette grating. This is

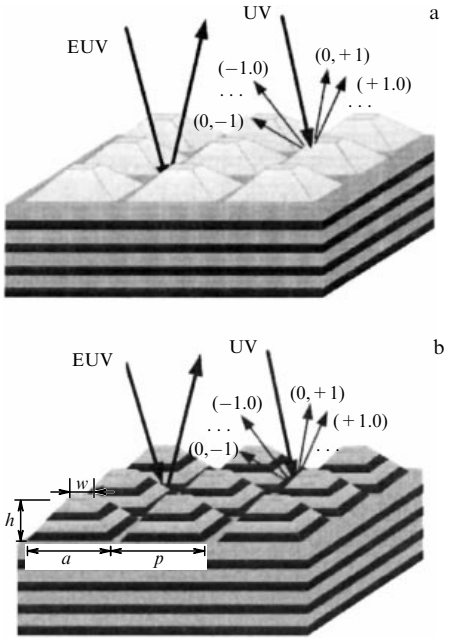

Figure 28. Diagram (a) of a silicon pyramidal structure deposited on an MIS and (b) of a pyramidal structure continuing the MIS [305].

related to the two-dimensional symmetry of the pyramid shape (Fig. 28b).

Pyramidal structures can be used in different wavelength ranges for different applications, including imaging of the Sun and filtration of radiation from high-harmonic sources [14].

13. Multilayer transmission diffraction gratings

Modern X-ray optical devices require elements with better dispersion possibilities. In the case of transmission diffraction gratings, this requirement reduces to the fabrication of structures with a large aspect ratio (the ratio of the relief depth to the transverse size of the grating line) and a high density of lines, i.e., with a very small period. An MDG satisfying these requirements can be obtained by MIS slicing and improvement [515, 516]. By selecting the relief depth (line length) and optical constants of the MIS, a phase MDG can be created.

However, large-area transmission gratings that are required, for example, for X-ray visualization experiments cannot be fabricated by slicing. The authors of [517, 518] proposed a method of fabricating transmission gratings with sub-micrometer periods and a centimeter size by the multilayer coating of a substrate shaped as an echelette. The advantage of this method is the high aspect ratio of the multilayer coating and the large substrate area. Several layers are deposited on the horizontal surfaces of a 'flight of stairs' by magnetron sputtering per passage. A silicon layer is then deposited on the upper part of the grating and is polished to equal the X-ray propagation path in the structure (Fig. 29a). Each step of the substrate forms a micro-grating with a width equal to the step height, and the array of microgratings represents a unit large-area grating with the continuity conditions satisfied. In this case, the grating period can be potentially shorter than 100 nm.

The phase-contrast sensitivity can be increased by using a far-field interferometer consisting of phase gratings compatible with a polychromatic radiation source.

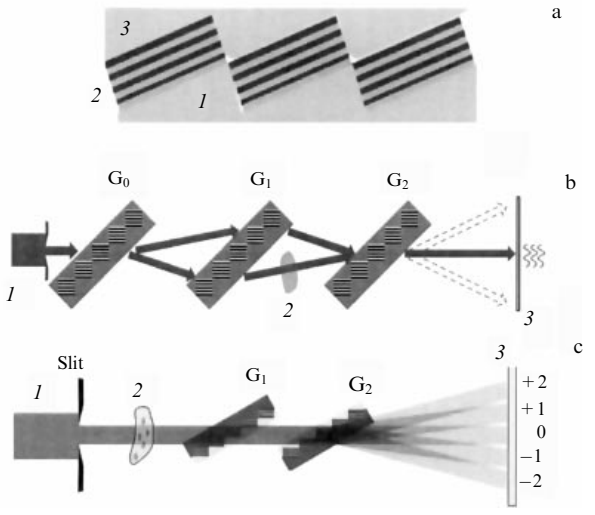

Figure 29. (a) Transmission MDG structure: *1*: Si echelette substrate, *2*: MIS, *3*: upper Si layer [517]. Phase-contrast imaging using transmission MDGs: with (b) Bonse–Hart [521] and (c) Talbot [520] interferometers *1*: primary X-ray beam, *2*: sample, *3*: detector; gratings G_0, G_1, and G_2 are splitter, mirror, and analyzer, respectively.

A classical X-ray Bonse–Hart interferometer [519] consists of three crystals cut out from a silicon monoblock and located at equal distances from each other. The authors of [520, 521] replaced crystals by identical nanometer phase gratings (Fig. 29b). The first grating G_0 (splitter) forms two coherent beams and the second grating G_1 (mirror) combines them on the third grating G_2 (analyzer). If a sample transparent enough to X-rays is then placed into one of the beams, the phase changes and a detector located behind the third grating record an interference pattern characterizing the sample.

An X-ray Talbot interferometer [522, 523] is fundamentally only slightly different from a crystal interferometer. In the setup described in [520], it consists of two diffraction gratings G_1 and G_2 [524] (Fig. 29c). The first (phase) grating G_1 produces a periodic modulation of the wave front, similar to a standing wave produced by the beamsplitter and mirror of the Bonse–Hart interferometer. The period of the obtained Fresnel interference pattern is of the order of a few micrometers and is typically much smaller than the detector resolution. The spatial and amplitude characteristics of the interference pattern are determined with the help of a grating G_2 mounted on one of the maximum-contrast planes and playing the role of an analyzer. While the grating analyzer G_2 should be an amplitude grating because it plays the role of a mask, the beamsplitter G_2 can be a phase or absorption grating. The interferometer 'decomposes' the beam into several diffraction orders, each of which contains the sample image. The distance between the interferometer and detector provides the separation of diffraction orders and prevents the overlap of images.

13.1 Multilayer Fresnel zone plate

A Fresnel zone plate has found applications in X-ray microscopy, holography, and interferometry as a compact focusing X-ray optics element.

The Fresnel zone plate consists of a series of concentric circular zones with alternating X-ray absorption and transmission [2, 252]. Its structure is determined by the formula [525]

$$r_n^2 = n\lambda f + \frac{n^2\lambda^2}{4}\,, \tag{28}$$

where λ is the X-ray wavelength, f is the focal distance for the first diffraction order, and r_n is the nth zone position. The second term can be omitted if $n\lambda \ll f$, which gives the interzone distance $d(r_n) = (r_n - r_{n-2}) \approx f\lambda/r_n$. The maximum possible resolution of the Fresnel zone is determined by the far field size Δr:

$$D_{\mathrm{m}} = 1.22\,\frac{\Delta r}{m}\,. \tag{29}$$

To overcome restrictions inherent in 'classical' amplitude Fresnel zone plates (in particular, with the low aspect ratio), the sputter-sliced method was developed [526–529], which is sometimes called the 'roll' method. In this method, two different materials with different X-ray absorption or different phase shift properties are in turn deposited on a rotating cylindrical gold or glass wire core by the method of multilayer atomic deposition. Then the required number of MDRs of the desired thickness can be obtained by slicing the obtained structure with the help of a focused ion beam to produce a concentric multilayer structure of the required thickness (10–200 μm) (Fig. 30). The important advantage of this method is the ability to cut out MDGs with different

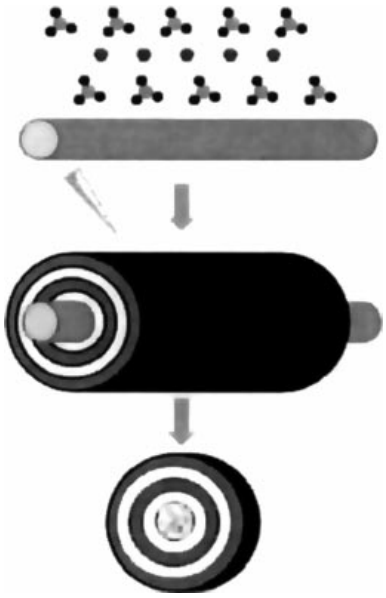

Figure 30. Schematic for obtaining a focusing MDG by the 'roll' method [529].

thicknesses, adapted to different X-ray energies, from one 'roll': In principle, the width of zones can be several atomic layers and, in addition, no restrictions are here imposed on the aspect ratio.

The difference between decrements $\Delta\delta$ of the refractive index of the materials used determines the relative phase shift of X-rays escaping from the MDG. Due to interference in the focal plane, maximum efficiency is reached at the thickness t_π corresponding to the phase shift by π: $t_\pi = \lambda/2\Delta\delta$ [526].

To fabricate MDGs by this method, researchers have studied many pairs of 'contrast' materials with a high thermal stability and low diffusion coefficients [528]. The authors of [527] have achieved a focusing efficiency in the first diffraction order amounting to 27% for an MDG consisting of $MoSi_2/Si$ layers with an external zone width of 40.4 nm, thickness of 32 μm, and aspect ratio of 792 for 20 keV X-rays.

13.2 Multilayer Laue lens

The 'roll' method is potentially suitable for the production of X-ray optical elements providing a sub-10-nm resolution. Nevertheless, the theoretical resolution limit can be unachievable due to aberrations introduced by zone positioning errors affecting the focal spot size. The layer deposition accuracy for MDGs with a focal distance suitable for practical applications is a serious problem. However, practical difficulties related to the core shape (the core is neither ideally round nor smooth), the roughness of interfaces in the multilayer structure, and deformations produced during its slicing complicate the production of high-resolution focusing MDGs.

A new approach to the production of diffraction optical instruments with a high numerical aperture and efficiency is a multilayer Laue lens (MLL) [10, 530]. It is produced by multilayer deposition on a flat substrate and consists of two (or more) materials deposited in turn with periods following the Fresnel zone plate law (28). It can be treated as a special type of zone plate.

The important advantage of the MLL over 'roll' MDGs is that the number of structural defects produced during the deposition of thin films on commercially manufactured silicon plates (chips) is considerably smaller, because the quality of the chip surface and its homogeneity significantly surpass the surface quality and the radial homogeneity of the core in the roll method.

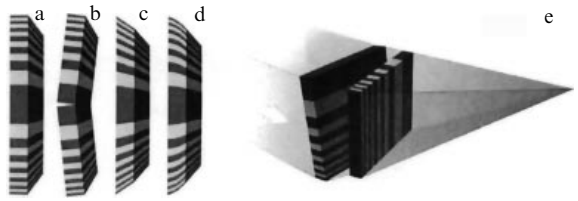

Figure 31. Four types of MLLs: (a) planar, (b) inclined, (c) wedge-like, and (d) bent. Diagram of 2D focusing using two crossed MLLs [530].

Various materials and deposition methods have been tested for manufacturing MLLs [531, 532], and several experiments using them have been performed [533–536], which demonstrates the 'maturity' of MLLs for scientific applications.

Up to now, most of the known X-ray experiments have been performed with MLLs consisting of planar zones. A planar MLL (Fig. 31a) is functionally identical to a linear Fresnel zone plate: zones are parallel to each and focus radiation normally incident on the lens. Although planar MLLs are rather simple to manufacture, they cannot efficiently focus X-rays to sizes below 10 nm because of dynamic diffraction effects [537].

To increase the focusing quality and efficiency, the two halves of the MLL can be inclined to the optical axis to satisfy the Bragg condition for external layers (Fig. 31b). The inclined MLL described in [538] ($\Delta r = 4$ nm, $f = 4.2$ mm) focused 12 keV X-rays onto a line 11.2 nm in width with 15% efficiency, while the MLL fabricated in [539] focused 19.5 keV X-rays onto a line 30 nm in width with a diffraction efficiency exceeding 40%. By the way, zones outside the optical axis are typically omitted, resulting in the formation of half the lens.

However, high efficiency is produced only by a small region of the inclined MLL. To obtain a focal spot 1 nm in diameter with an efficiency above 50%, it is necessary to create an MLL with a monotonically changing slope of zones with respect to the incident beam, with the Bragg law satisfied locally. Such a structure is called a wedge-like MLL [540–542] (Fig. 31c). Wedge-like MLLs can have a very high efficiency (up to 74%) [543].

The wedge-like MLL described in [544] had an efficiency of 27% and a 26 nm focal size for 14.6 keV X-rays, in good agreement with theoretical calculations.

High-resolution X-ray optical instruments require the creation of an MLL with bent spatial zones consisting of confocal parabolic layers for the incident plane wave or confocal ellipsoidal layers for a spherical wave [537] (Fig. 31d). However, the fabrication of such MLLs involves great difficulties. One way to overcome them is based on the simulation of the diffraction of X-rays in a bulk circular zone plate: the optimized profile of its zones is given by their multilevel construction with a radial increase in slopes and a decrease in the height of the levels [545].

The four types of MLLs described above have different focusing properties due to their different dependences on dynamic effects [537]. As a linearly focusing optical element, the MLL focuses X-rays only in one plane, irrespective of its

type. Two-dimensional focusing can be achieved with the help of crossed MLLs [533–536, 542, 543] (Fig. 31d). It was reported in [546] that crossed MLLs consisting of WC/SiC MISs focused 16.3 keV X-rays on an 8.4×6.8 nm spot.

14. Conclusions and outlook

It follows from the foregoing that considerable progress has been achieved in developing the MISs and MDGs in recent years [14]. They provide the required reflectance, transmission band, spectral purity, and other parameters, although not all of these can be achieved simultaneously. The new optical elements have greatly enhanced the possibilities of various scientific applications. Nevertheless, new possibilities exist and problems related to high-brightness sources appear. New generations of EUV sources have been developed or are appearing, including diffraction-limited sources [547], FELs, higher-harmonic generators, and high-power EUV radiation sources for lithography [548]. New fourth-generation synchrotron radiation sources [549] will provide a higher brightness with much better coherence than for the existing generation of storage rings. To completely realize the advantages of these new sources, it is necessary to preserve the increased photon flux and to improve the methods of controlling X-ray pulses for providing the required spectral/temporal and polarization properties of radiation for various applications [14].

It is necessary to develop methods for creating multilayer coatings with an extremely high accuracy, lateral homogeneity of periods, and the quality of interfaces for increasing the efficiency of optical devices and maintaining the coherence of radiation sources. Highly efficient multilayer gratings with ultrahigh spectral resolution are required for studying various processes in matter. Pulse formation methods used in the EUV region should be developed to control all the characteristics of femto- or secondary attosecond pulses. The development of some of these optical instruments has already been initiated, but many problems require innovative solutions and improvement in deposition and nanoprocessing technologies [14]. The development of high-accuracy optics will improve a number of related methods such as resonance inelastic X-ray scattering [550], nanoscale spectroscopy [551], ultrafast dynamic studies [552], and quantum control [553]. On the other hand, extremely bright EUV sources will also create other problems in optics, such as a limited lifetime.

The surface contamination and degradation caused by carbon and oxygen can be intensified at high irradiation energies. The thermal load on mirrors will accelerate the interdiffusion and phase changes in materials, while the extremely high brightness of ultrashort femtosecond pulses emitted by FELs can produce structural modifications or even the melting of layers. Therefore, a search for new MISs with enhanced thermal stability and stability against damage and oxidation is required. Temperature variations can produce strong distortions (aberrations) of the reflected wavefront, which impair optical characteristics. These distortions, as a rule, are nonuniform over the wavefront due to nonuniform illumination and can be on a scale comparable to the wavelength. To obtain the required optical characteristics, it is necessary to correct the wavefront distortions. This can be achieved by using adaptive optics, for example, based on deformable mirrors [554, 555].

In the EUV lithography field, it is desirable to pass to wavelengths shorter than 11 nm (for example, 6.7 nm) [53].

The strict requirements underlying the concept of an X-ray telescope require the fabrication of MISs with periods from 1.5 to 25 nm and a great number of bilayers to provide high refection efficiency at energies up to 600 keV. Increasing interest in operations with higher-energy X-rays and obtaining greater zones for data collection will lead to more complex multilayer constructions and therefore to increased requirements for simulation accuracy. Although it is unlikely that future missions will be able to avoid empirical corrections to determine the response of an X-ray telescope, the goal should be to minimize their use by controlling the most significant sources of simulation uncertainty. Manufacturing details become especially important for complex optical schemes of telescopes required for X-ray astronomy [556].

Solving the inverse problem of extracting structural data from reflectance measurements involves certain difficulties caused by the necessity of performing a fitting procedure requiring hundreds or even thousands of simulations. Thus, the calculation time is an important aspect in the attempt to determine the optical properties of a multilayer structure [454]. The great number of MIS parameters complicates the optimization of the MIS structure, but, on the other hand, imparts an unusual flexibility to it. Without a doubt, we will witness further advances in the development and use of multilayer X-ray interference structures in the coming years.

This study was supported by the Ministry of Science and Higher Education in the framework of the Crystallography and Photonics State Program of the Russian Academy of Sciences.

References

1. Spiller E *Exp. Meth. Phys. Sci.* **31** 271 (1998)
2. Michette A G *Optical Systems for Soft X-Rays* (New York: Plenum Press, 1986); Translated into Russian: *Optika Myagkogo Rentgenovskogo Izlucheniya* (Moscow: Mir, 1989)
3. Vinogradov A V et al. *Zerkal'naya Rentgenovskaya Optika* (Specular X-Ray Optics) (Exec. Ed. A V Vinogradov) (Leningrad: Mashinostroenie, 1989)
4. Dhez P *J. Phys. Colloq.* **47** C6-267 (1986)
5. Barbee T W *Opt. Eng.* **25** 258898 (1986)
6. Bruijn M P et al. *Proc. SPIE* **984** 54 (1988)
7. Vinogradov A V *Quantum Electron.* **32** 1113 (2002); *Kvantovaya Elektron.* **32** 1113 (2002)
8. Bajt S, Edwards N V, Madey T E *Surf. Sci. Rep.* **63** 73 (2008)
9. Morawe Ch, Osterhoff M *X-Ray Opt. Instrum.* **2010** 479631 (2010)
10. Yan H et al. *X-Ray Opt. Instrum.* **2010** 401854 (2010)
11. Louis E et al. *Prog. Surf. Sci.* **86** 255 (2011)
12. Vishnyakov E A et al. *Quantum Electron.* **42** 143 (2012); *Kvantovaya Elektron.* **42** 143 (2012)
13. Barysheva M M et al. *Phys. Usp.* **55** 681 (2012); *Usp. Fiz. Nauk* **182** 727 (2012)
14. Huang Q et al. *Appl. Phys. Rev.* **4** 011104 (2017)
15. Jiang L, Al-Mosheky Z, Grupido N *Powder Diffract.* **17** (2) 81 (2002)
16. Shimizu K, Omote K *The Rigaku J.* **24** 1 (2008)
17. Blokhin M A *Fizika Rentgenovskikh Luchei* (Physics of X-Rays) 2nd ed. (Moscow: GITTL, 1957)
18. Kozhevnikov I V, Vinogradov A V *Phys. Scripta* **1987** (T17) 137 (1987)
19. Underwood J H, Barbee T W *Appl. Opt.* **20** 3027 (1981)
20. Kozhevnikov I V et al. *Opt. Express* **19** 9172 (2011)
21. Vinogradov A V, Zeldovich B Ya *Appl. Opt.* **16** 89 (1977)
22. Medvedev V V et al. *Opt. Mater. Express* **5** 1450 (2015)
23. Andreev S S et al. *Nucl. Instrum. Meth. Phys. Res. A* **448** 133 (2000)
24. Andreev S S et al. *Proc. SPIE* **1800** 195 (1992)
25. Salashchenko N N et al. *Proc. SPIE* **2011** 402 (1994)

26. Salashchenko N N, Shamov E A *Opt. Commun.* **134** 7 (1997)
27. Schäfers F et al. *Appl. Opt.* **37** 719 (1998)
28. Kuhlmann T et al. *Appl. Opt.* **41** 2048 (2002)
29. Guggenmos A et al. *Opt. Express* **22** 26526 (2014)
30. Haase A et al. *J. Appl. Cryst.* **49** 2161 (2016)
31. Eriksson F et al. *Opt. Lett.* **28** 2494 (2003)
32. Eriksson F et al. *J. Appl. Phys.* **104** 063516 (2008)
33. Huang Q et al. *Sci. Rep.* **7** 12929 (2017)
34. Mertins H-C et al. *Appl. Opt.* **37** 1873 (1998)
35. Prokhorov K A et al. *Poverkhnost Rentgen. Sinchrotron. Neitron. Issled.* (1) 166 (1999)
36. Eriksson F et al. *Thin Solid Films* **500** 84 (2006)
37. Ghafoor N et al. *Appl. Opt.* **45** 137 (2006)
38. Artyukov I A et al. *Proc. SPIE* **5919** 59190E (2005)
39. Artyukov I A et al. *Micron* **41** 722 (2010)
40. Akhsakhalyan A D et al. *Phys. Scripta* **43** 516 (1993)
41. Niibe M et al. *Proc. SPIE* **1720** 208 (1992)
42. Artyukov et al. *Opt. Lett.* **34** 2930 (2009)
43. Stearns D G, Rosen R S, Vernon S P *Appl. Opt.* **32** 6952 (1993)
44. Wu B, Kumar A *Appl. Phys. Rev.* **1** 011104 (2014)
45. Medvedev V "Tailoring spectral properties of extreme UV multilayer optics", Dissertation (Enschede: Univ. Twente, 2015)
46. Stearns D G, Rosen R S, Vernon S P *J. Vac. Sci. Technol. A* **9** 2662 (1991)
47. Folta J A et al. *Pros. SPIE* **3676** 702 (1999)
48. Stuik R et al. *J. Vac. Sci. Technol. B* **17** 2998 (1999)
49. Louis E et al. *Pros. SPIE* **3997** 406 (2000)
50. Bajt S et al. *Opt. Eng.* **41** 1797 (2002)
51. Andreev S S et al. *Thin Solid Films* **415** 123 (2002)
52. Hiruma K et al. *Thin Solid Films* **516** 2050 (2008)
53. Chkhalo N I, Salashchenko N N *AIP Adv.* **3** 082130 (2013)
54. Stearns D G et al. *Mater. Res. Soc. Symp. Proc.* **382** 329 (1995)
55. Skulina K M et al. *Appl. Opt.* **34** 3727 (1995)
56. Mirkarimi P B, Montcalm C *Proc. SPIE* **3331** 133 (1998)
57. Tsarfati T et al. *Thin Solid Films* **518** 1365 (2009)
58. Montcalm C et al. *Appl. Opt.* **35** 5134 (1996)
59. Andreev S S et al. *Tech. Phys.* **55** 1168 (2010); *Zh. Tekh. Fiz.* **80** (8) 93 (2010)
60. Platonov Yu et al. *Proc. SPIE* **8076** 80760N (2011)
61. Chkhalo N I et al. *Appl. Phys. Lett.* **102** 011602 (2013)
62. Makhotkin I A et al. *Opt. Express* **21** 29894 (2013)
63. Ricardo P et al. *Appl. Opt.* **40** 2747 (2001)
64. Michaelsen C et al. *Opt. Lett.* **26** 792 (2001)
65. Michaelsen C et al. *Proc. SPIE* **4501** 135 (2001)
66. André J-M et al. *X-Ray Spectrom.* **34** 203 (2005)
67. Michaelsen C et al. *Proc. SPIE* **4782** 143 (2002)
68. Makhotkin I A et al. *Phys. Status Solidi A* **208** 2597 (2011)
69. Henke B L, Gullikson E M, Davis J C *Data Nucl. Data Tables* **54** 181 (1993)
70. Vishnyakov E A et al. *Quantum Electron.* **43** 666 (2013); *Kvantovaya Elektron.* **43** 666 (2013)
71. Kopylets I A et al. *Appl. Surf. Sci.* **307** 360 (2014)
72. Corso A J et al. *Opt. Express* **20** 8006 (2012)
73. Kastner S O, Neupert W M, Swartz M *Astrophys. J.* **191** 261 (1974)
74. Morawe Ch, Supruangnet R, Peffen J-Ch *Thin Solid Films* **588** 1 (2015)
75. Xu D et al. *Opt. Express* **23** 33018 (2015)
76. Wu M-Y et al. *Proc. SPIE* **10235** 102350F (2017)
77. Windt D L et al. *Proc. SPIE* **5168** 1 (2003)
78. Stearns D G, Rosen R S, Vernon S P *Opt. Lett.* **16** 1283 (1991)
79. Kjornrattanawanich B, Bajt S *Appl. Opt.* **43** 5955 (2004)
80. Montcalm C et al. *Opt. Lett.* **19** 1173 (1994)
81. Montcalm C et al. *Opt. Lett.* **20** 1450 (1995)
82. Sae-Lao B, Montcalm C *Opt. Lett.* **26** 468 (2001)
83. Huber S P et al. *Opt. Mater. Express* **6** 3946 (2016)
84. Xu D et al. *Opt. Express* **23** 33018 (2015)
85. Lemen J R et al. *Solar Phys.* **275** 17 (2012)
86. Suman M et al. *Appl. Opt.* **48** 5432 (2009)
87. Meltchakov E et al. *Appl. Phys. A* **98** 111 (2010)
88. Windt D L, Bellotti J A *Appl. Opt.* **48** 4932 (2009)
89. Hu M-H et al. *Opt. Express* **18** 20019 (2010)
90. Zuev S Yu et al. *Bull. Russ. Acad. Sci. Phys.* **74** 50 (2010); *Izv. Ross. Akad. Nauk Fiz.* **74** 58 (2010)
91. Zhong Q et al. *Opt. Express* **20** 10692 (2012)
92. Zhong Q et al. *J. Phys. Conf. Ser.* **425** 152010 (2013)
93. Windt D L *Proc. SPIE* **9604** 96040P (2015)
94. Nii H et al. *J. Synchrotron Radiat.* **5** 702 (1998)
95. Zhu J et al. *Proc. SPIE* **8168** 81681C (2012)
96. Zhu J et al. *Front. Optoelectron. China* **1** 305 (2008)
97. Zhu J et al. *Appl. Opt.* **49** 3922 (2010)
98. Yoshikawa I et al. *Rev. Sci. Instrum.* **76** 066109 (2005)
99. Takenaka H et al. *J. Electron Spectrosc. Relat. Phenom.* **144 – 147** 1047 (2005)
100. Soufli R et al. *Proc. SPIE* **5901** 59010M (2005)
101. Maury H et al. *Eur. Phys. J. B* **64** 193 (2008)
102. Soufli R et al. *Proc. SPIE* **8443** 84433R (2012)
103. Li H C et al. *Proc. SPIE* **8501** 85010G (2012)
104. Le Guen K et al. *J. Phys. Chem. C* **114** 6484 (2010)
105. Li H et al. *Appl. Phys. Lett.* **102** 111103 (2013)
106. Uspenskii Yu A et al. *Proc. SPIE* **3156** 288 (1997)
107. Schaefers F et al. *Proc. SPIE* **5188** 138 (2003)
108. Uspenskii Yu A et al. *Opt. Lett.* **23** 771 (1998)
109. Uspenskii Yu A et al. *Nucl. Instrum. Meth. Phys. Res. A* **448** 147 (2000)
110. Vidal-Dasilva M, Fernández-Perea M, Larruquert J I *Proc. SPIE* **7448** 74480N (2009)
111. Windt D L et al. *Opt. Lett.* **30** 3186 (2005)
112. Kjornrattanawanich B et al. *Appl. Opt.* **45** 1765 (2006)
113. Kjornrattanawanich B et al. *Proc. SPIE* **6317** 63170U (2006)
114. Kjornrattanawanich B, Windt D L, Seely J F *Opt. Lett.* **33** 965 (2008)
115. Seely J F et al. *Proc. SPIE* **6317** 63170T (2006)
116. Windt D L *Proc. SPIE* **9603** 96031C (2015)
117. Paul A, Lodha G S *Phys. Rev. B* **65** 245416 (2002)
118. Windt D L et al. *Proc. SPIE* **4012** 442 (2000)
119. Mao P H *Appl. Opt.* **38** 4766 (1999)
120. Jankowski A F, Makowiecki D M *Opt. Eng.* **30** 2003 (1991)
121. Pradhan P C et al. *J. Phys. D* **49** 135305 (2016)
122. Andreev S S et al. *J. Synchrotron Rad.* **10** 358 (2003)
123. Platonov Yu Ya, Gomez L, Broadway D *Proc. SPIE* **4782** 152 (2002)
124. Jensen C P, Madsen K K, Christensen F E *Proc. SPIE* **6266** 626612 (2006)
125. Windt D L et al. *Appl. Opt.* **42** 2415 (2003)
126. Spiga D et al. *Proc. SPIE* **5488** 813 (2004)
127. Dietsch R et al. *Proc. SPIE* **4144** 137 (2000)
128. Windt D L *App. Phys. Lett.* **74** 2890 (1999)
129. Boher P, Hennet L, Houdy Ph *Pros. SPIE* **1345** 198 (1990)
130. Larruquert J I *J. Opt. Soc. Am. A* **18** 2617 (2001)
131. Larruquert J I *J. Opt. Soc. Am. A* **19** 391 (2002)
132. Larruquert J I *Opt. Commun.* **206** 259 (2002)
133. Gautier J et al. *Appl. Opt.* **44** 384 (2005)
134. Le Guen K et al. *Appl. Phys. A* **102** 69 (2011)
135. Jiang H, in *Optimization Algorithms. Methods and Applications* (Ed. O Baskan) (London: InTech, 2016) p. 221
136. Press W H et al. *Numerical Recipes in C++: The Art of Scientific Computing* 2nd ed. (Cambridge: Cambridge Univ. Press, 2002) pp. 394 – 455
137. Singh M, Braat J J M *Proc. SPIE* **3997** 412 (2000)
138. Parratt L G *Phys. Rev.* **95** 359 (1954)
139. Spiga D, in *Modern Developments in X-Ray and Neutron Optics* (Eds A Erko et al.) (New York: Springer-Verlag, 2008) p. 233
140. Chen L, Deng N Y, Zhang J Z *Comput. Optimizat. Appl.* **35** 5 (2006)
141. Amini K, Ghorbani Rizi A *J. Comput. Appl. Math.* **234** 805 (2010)
142. Petrova S S, Solov'ev A D *Historia Math.* **24** 361 (1997)
143. Levenberg K *Quart. Appl. Math.* **2** 164 (1944)
144. Marquardt D W *SIAM J. Appl. Math.* **11** 431 (1963)
145. Kozhevnikov I V, Bukreeva I N, Ziegler E *Nucl. Instrum. Meth. Phys. Res. A* **460** 424 (2001)
146. Ziegler E et al. *Proc. SPIE* **4782** 169 (2002)
147. Nelder J A, Mead R *Comput. J.* **7** 308 (1965)
148. Martin S, Rivory J, Schoenauer M *Appl. Opt.* **34** 2247 (1995)
149. Wormington M et al. *Phil. Trans. R. Soc. London A* **357** 2827 (1999)
150. Sanchez del Rio M, Pareschi G *Proc. SPIE* **4145** 88 (2001)
151. Kirkpatrick S, Gelatt C D (Jr.), Vecchi M P *Science* **220** 671 (1983)
152. Dekkers A, Aarts E *Math. Program.* **50** 367 (1991)

153. Ziegler E et al. *Adv. X-Ray Anal.* **45** 345 (2002)
154. Ali M M, Storey C *Int. J. Comput. Math.* **53** 229 (1994)
155. Törn A, Viitanen S *J. Global Optimizat.* **5** 267 (1994)
156. Poli R, Kennedy J, Blackwell T *Swarm Intell.* **1** 33 (2007)
157. Dorigo M, Blum C *Theor. Comput. Sci.* **344** 243 (2005)
158. Spiga D et al. *Proc. SPIE* **5536** 71 (2004)
159. Spiga D et al. *Proc. SPIE* **6266** 626616 (2006)
160. Windt D L *Comput. Phys.* **12** 360 (1998)
161. Spiller E et al. *Appl. Phys. Lett.* **37** 1048 (1980)
162. Bajt S et al. *Proc. SPIE* **6586** 65860J (2007)
163. Barbee T W, Mrowka S, Hettrick M C *Appl. Opt.* **24** 883 (1985)
164. Danilin B S, Syrchin V K *Magnetronnye Raspylitel'nye Sistemy* (Magnetron Sputtering Systems) (Moscow: Radio i Svyaz, 1982)
165. Kuz'michev A I *Magnetronnye Raspylitel'nye Sistemy* Book 1 *Vvedenie v Fiziku i Tekhniku Magnetronnogo Raspyleniya* (Magnetron Sputtering Systems. Book 1. Introduction to the Physics and Technology of Magnetron Sputtering) (Kiev: Avers, 2008)
166. Putero-Vuaroqueaux M, Vidal B *J. Phys. Condens. Matter* **13** 3969 (2001)
167. Paret V et al. *Microelectron. Eng.* **61 – 62** 145 (2002)
168. Meltchakov E et al. *J. Phys. Condens. Matter* **18** 3355 (2006)
169. Morawe Ch et al. *AIP Conf. Proc.* **1234** 720 (2010)
170. Spiller E et al. *Appl. Opt.* **42** 4049 (2003)
171. Gawlitza P et al. *Proc. SPIE* **6317** 63170G (2006)
172. Kloidt A et al. *Appl. Phys. Lett.* **58** 2601 (1991)
173. Nedelcu I et al. *Thin Solid Films* **515** 434 (2006)
174. Gaponov S V et al. *Nucl. Instrum. Meth. Phys. Res.* **208** 227 (1983)
175. Braun St et al. *Microelectron. Eng.* **57 – 58** 9 (2001)
176. Dietsch R et al. *Appl. Surf. Sci.* **197 – 198** 169 (2002)
177. Andreev S S et al. *Gentr. Eur. J. Phys.* **1** 191 (2003)
178. Artyukov I A et al. *Proc. SPIE* **5919** 59190E (2005)
179. Andreev S S et al. *Nucl. Instrum. Meth. Phys. Res. A* **603** 80 (2009)
180. Montcalm C et al. *Proc. SPIE* **3331** 42 (1998)
181. Vainer Yu A et al. *Poverkhnost Rentgen. Sinchrotron. Neitron. Issled.* (1) 10 (2007)
182. Névot L, Croce P *Rev. Phys. Appl.* **15** 761 (1980)
183. Jonnard P et al. *Proc. SPIE* **7360** 73600O (2009)
184. Le Guen K et al. *X-Ray Spectrom.* **40** 338 (2011)
185. Valkovskiy G A et al. *Phys. Status Solidi A* **208** 2623 (2011)
186. Yuan Y et al. *Appl. Surf. Sci.* **331** 8 (2015)
187. Sinha M, Modi M H *J. Laser Opt. Photon.* **3** 138 (2016)
188. Nevot L, Pardo B, Corno J *Rev. Phys. Appl.* **23** 1675 (1988)
189. Kojima I, Li B *Rigaku J.* **16** 31 (1999)
190. Borovskii I B et al. *Sov. Phys. Usp.* **29** 539 (1986); *Usp. Fiz. Nauk* **149** 275 (1986)
191. Günther H *NMR-Spectroskopie* (Stuttgart: Georg Thieme Verlag, 1983); Translated into English: *NMR Spectroscopy. An Introduction* (Chichester: Wiley, 1980); Translated into Russian: *Vvedenie v Kurs Spektroskopii YaMR* (Moscow: Mir, 1984)
192. Krämer M et al. *J. Analyt. Atom. Spectrom.* **21** 1136 (2006)
193. Sinha S K *J. Phys. III France* **4** 1543 (1994)
194. Holý V *Appl. Phys. A* **58** 173 (1994)
195. Binnig G, Quate C F, Gerber C *Phys. Rev. Lett.* **56** 930 (1986)
196. Mironov V L *Osnovy Skaniruyushchei Zondovoi Mikroskopii* (Fundamentals of Scanning Probe Microscopy) (Moscow: Tekhnosfera, 2004)
197. Briggs D, Seah M P (Eds) *Practical Surface Analysis*: *by Auger and X-ray Photoelectron Spectroscopy* (Chichester: Wiley, 1983); Translated into Russian: *Analiz Poverkhnosti Metodami Ozhe- i Rentgenovskoi Fotoelektronnoi Spektroskopii* (Moscow: Mir, 1987)
198. Nefedov V I, Cherepin V T *Fizicheskie Metody Issledovaniya Poverkhosti Tverdyhkh Tel* (Physical Method for Studying Solid Surfaces) (Moscow: Nauka, 1983) p. 150
199. Walls M G, Chevalier J-P, Hytch M J *J. Phys. IV France* **6** C7-213 (1996)
200. Yulin S et al. *J. Appl. Phys.* **92** 1216 (2002)
201. Spiller E *Proc. SPIE* **563** 367 (1985)
202. Spiller E et al. *Appl. Phys. Lett.* **61** 1481 (1992)
203. Panissod P, Mény C *Appl. Magn. Reson.* **19** 447 (2000)
204. Assoufid L, Graafsma H *MRS Bull.* **42** 418 (2017)
205. Ragozin E N, Sobel'man I I *Phys. Usp.* **48** 1249 (2005); *Usp. Fiz. Nauk* **175** 1339 (2005)
206. Brandi F, Neshev D, Ubachs W *Phys. Rev. Lett.* **91** 163901 (2003)
207. Ritucci A et al. *Appl. Phys. Lett.* **86** 101106 (2005)
208. Vinogradov A V et al. *Proc. SPIE* **4505** 230 (2001)
209. Böttger T et al. *Thin Solid Films* **444** 165 (2003)
210. Jonnard P et al. *Surf. Sci.* **604** 1015 (2010)
211. Maury H et al. *Thin Solid Films* **514** 278 (2006)
212. de Rooij-Lohmann V I T A et al. *J. Appl. Phys.* **108** 094314 (2010)
213. Pershyn Yu P et al. *Opt. Eng.* **52** 095104 (2013)
214. Braun S et al. *Proc. SPIE* **4782** 185 (2002)
215. Chkhalo N I et al. *Opt. Lett.* **42** 5070 (2017)
216. Voronov D L et al. *Poverkhnost Rentgen. Sinchrotron. Neitron. Issled.* (5) 13 (2007)
217. Voronov D L et al. *AIP Conf. Proc.* **641** 575 (2002)
218. Jankowski A F et al. *Thin Solid Films* **469 – 470** 372 (2004)
219. Pershyn Y P et al. *Appl. Phys. A* **103** 1021 (2011)
220. Huang Q et al. *Opt. Lett.* **41** 701 (2016)
221. Li P et al. *Vacuum* **128** 85 (2016)
222. Zhu J et al. *Opt. Express* **19** 21849 (2011)
223. Windt D L et al. *Appl. Opt.* **48** 5502 (2009)
224. Modi M H et al. *Opt. Express* **20** 15114 (2012)
225. Feigl T et al. *Proc. SPIE* **4506** 121 (2001)
226. Kaiser N, Yulin S A, Feigl T *Proc. SPIE* **4146** 91 (2000)
227. Modi M H et al. *Opt. Express* **20** 15114 (2012)
228. Fernández-Perea M et al. *Nucl. Instrum. Meth. Phys. Res. A* **710** 114 (2013)
229. Choueikani F et al. *Appl. Phys. A* **111** 191 (2013)
230. Liu Ch et al. *Proc. SPIE* **5537** 154 (2004)
231. Kleineber U et al. *Phys. Status Solidi A* **145** 539 (1994)
232. Kondratenko V V et al. *Appl. Opt.* **32** 1811 (1993)
233. Konotopskii L E *Metallofiz. Noveish. Tekhol.* **38** 825 (2016)
234. Ghafoor N et al. *Appl. Phys. Lett.* **92** 091913 (2008)
235. Kuznetsov D S et al. *Opt. Lett.* **40** 3778 (2015)
236. Wang Y et al. *Opt. Express* **25** 7749 (2017)
237. Burcklen C et al. *Opt. Lett.* **42** 1927 (2017)
238. Luby S, Majkova E *Appl. Surf. Sci.* **248** 316 (2005)
239. Bai H L et al. *J. Phys. Condens. Matter* **8** 8763 (1996)
240. Jonnard P et al. *Proc. SPIE* **7360** 73600O (2009)
241. Galtayries A et al. *Surf. Interface Analys.* **42** 653 (2010)
242. Voorma H-J et al. *J. Appl. Phys.* **82** 1876 (1997)
243. Birch J et al. *Vacuum* **68** 275 (2002)
244. Spiller E *Appl. Phys. Lett.* **54** 2293 (1989)
245. Puik E J et al. *Thin Solid Films* **193 – 194** 782 (1990)
246. Kloidt A et al. *Thin Solid Films* **228** 154 (1993)
247. Louis E et al. *Microelectron. Eng.* **23** 215 (1994)
248. Schlatmann R et al. *Appl. Surf. Sci.* **78** 147 (1994)
249. Louis E et al. *Proc. SPIE* **2515** 194 (1995)
250. Guggenmos A et al. *Opt. Express* **22** 26526 (2014)
251. Yi Q et al. *Appl Opt.* **56** C145 (2017)
252. Niibe M et al. *Proc. SPIE* **1343** 2 (1990)
253. Wang F-F et al. *Chinese Phys. C* **36** 909 (2012)
254. Fullerton E E et al. *Phys. Rev. B* **48** 17432 (1993)
255. Kozhevnikov I V "Teoriya difraktsii rentgenovskogo izlucheniya ot neodnorodnykh sloistykh sred" ("Theory of X-ray diffraction from inhomogeneous layered media"), Dissertation, Dr. Phys.-Math. Sciences (Moscow: Shubnikov Institute of Cristallography Russian Academy of Sciences, 2013)
256. Majaniemi S, Ala-Nissila T, Krug J *Phys. Rev. B* **53** 8071 (1996)
257. Soufli R et al. *Proc. SPIE* **8501** 850102 (2012)
258. Zubarev E N et al. *Appl. Phys. A* **90** 705 (2008)
259. Eriksson F et al. *Proc. SPIE* **4506** 14 (2001)
260. Windt D L, Gullikson E M, Walton Ch C *Opt. Lett.* **27** 2212 (2002)
261. Stearns M B, Chang C-H, Stearns D G *J. Appl. Phys.* **71** 187 (1992)
262. Voorma H-J et al. *J. Appl. Phys.* **83** 4700 (1998)
263. Ogura S et al. *Proc. SPIE* **984** 140 (1988)
264. de Rooij-Lohmann V I T A et al. *Appl. Surf. Sci.* **257** 6251 (2011)
265. Bellotti J A, Windt D L *Proc. SPIE* **7437** 743715 (2009)
266. Windt D L *Proc. SPIE* **6688** 66880R (2007)
267. Windt D L et al. *J. Appl. Phys.* **78** 2423 (1995)
268. Kola R R et al. *Appl. Phys. Lett.* **60** 3120 (1992)
269. Kassner M E et al. *J. Mater. Sci.* **31** 2291 (1996)
270. Barthelmess M, Bajt S *Appl. Opt.* **50** 1610 (2011)
271. Mirkarimi P B *Opt. Eng.* **38** 1246 (1999)
272. Shiraishi M et al. *Jpn. J. App. Phys.* **39** 6810 (2000)
273. Leisegang T et al. *Appl. Phys. A* **77** 965 (2003)

274. Windt D L *Proc. SPIE* **3448** 280 (1998)
275. Windt D L *J. Vac. Sci. Technol. B* **17** 1385 (1999)
276. Andreev S S et al. *Nucl. Instrum. Meth. Phys. Res. A* **470** 162 (2001)
277. Zoethout E et al. *Proc. SPIE* **5037** 872 (2003)
278. Bajt S et al. *Appl. Opt.* **42** 5750 (2003)
279. Graham S et al. *J. Vac. Sci. Technol. B* **20** 2393 (2002)
280. Graham S (Jr.) et al. *Proc. SPIE* **5037** 460 (2003)
281. Oizumi H et al. *Pros. SPIE* **5751** 1147 (2005)
282. Wedowski M et al. *Proc. SPIE* **3767** 217 (1999)
283. Oestreich S et al. *Pros. SPIE* **4146** 64 (2000)
284. Klebanoff L E et al. *J. Vac. Sci. Technol. B* **20** 696 (2002)
285. Singh M, Braat J J M *Opt. Lett.* **26** 259 (2001)
286. Yulin S et al. *Proc. SPIE* **6921** 692118 (2008)
287. Corso A J et al. *Opt. Express* **19** 13963 (2011)
288. Over H, Muhler M *Prog. Surf. Sci.* **72** 3 (2003)
289. Grisham M et al. *Opt. Lett.* **29** 620 (2004)
290. Hau-Riege S P et al. *Phys. Rev. Lett.* **98** 145502 (2007)
291. Barkusky F et al. *Opt. Express* **18** 4346 (2010)
292. Corso A J et al. *J. Appl. Phys.* **113** 203106 (2013)
293. Müller M et al. *Appl. Phys. A* **108** 263 (2012)
294. Louis E et al. *Proc. SPIE* **7361** 73610I (2009)
295. Khorsand A R et al. *Opt. Express* **18** 700 (2010)
296. Sobierajski R et al. *Opt. Express* **19** 193 (2011)
297. Giglia A et al. *Nucl. Instrum. Meth. Phys. Res. A* **635** S30 (2011)
298. Suman M et al. *Thin Solid Films* **520** 2301 (2012)
299. Fomenkov I V et al. *Proc. SPIE* **8679** 86792I (2013)
300. Lilensten J et al. *Ann. Geophys.* **26** 269 (2008)
301. Artyukov I A et al. *Opt. Commun.* **102** 401 (1993)
302. Fujimoto J et al. *Proc. SPIE* **8332** 83220F (2012)
303. Volodin B A et al. *Bull. Russ. Acad. Sci. Phys.* **74** 46 (2010); *Izv. Ross. Akad. Nauk. Fiz.* **74** 53 (2010)
304. Chkhalo N I et al. *Appl. Opt.* **55** 4683 (2016)
305. Huang Q et al. *Opt. Express* **22** 19365 (2014)
306. Huang Q et al. *Proc. SPIE* **9048** 90480G (2014)
307. van Herpen M M J W et al. *Opt. Lett.* **33** 560 (2008)
308. Huber S P et al. *Proc. SPIE* **8848** 884814 (2013)
309. Suman M et al. *Proc. SPIE* **7360** 73600T (2009)
310. Naujok P et al. *Opt. Express* **23** 4289 (2015)
311. Soer W A et al. *Opt. Lett.* **34** 3680 (2009)
312. Medvedev V V et al. *Opt. Lett.* **37** 1169 (2012)
313. Medvedev V V et al. *Appl. Phys. Lett.* **103** 221114 (2013)
314. Rack A et al. *J. Synchrotron Rad.* **17** 496 (2010)
315. Chu Y S et al. *Rev. Sci. Instrum.* **73** 1485 (2002)
316. Platonov Yu Y et al. *Proc. SPIE* **5537** 161 (2004)
317. Feng R et al. *Proc. SPIE* **7077** 70771Y (2008)
318. Oberta P, Platonov Y, Flechsig U *J. Synchrotron Rad.* **19** 675 (2012)
319. Khounsary A et al. *Proc. SPIE* **9963** 99630W (2016)
320. Gautier J et al. *Opt. Commun.* **281** 3032 (2008)
321. Roling S et al. *Opt. Lett.* **39** 2782 (2014)
322. Henry J P, Spiller E, Weisskopf M *Proc. SPIE* **316** 166 (1982)
323. Misture S T *X-Ray Opt. Instrum.* **2008** 408702 (2008)
324. Wang Y et al. *J. Synchrotron Rad.* **14** 138 (2007)
325. Kazimirov A et al. *J. Synchrotron Rad.* **13** 204 (2006)
326. Borozdin Yu E et al. *JETP Lett.* **87** 27 (2008); *Pis'ma Zh. Eksp. Teor. Fiz.* **87** 33 (2008)
327. Lopatin A Ya et al. *Tech. Phys.* **55** 1018 (2010); *Zh. Tekh. Fiz.* **80** (7) 105 (2010)
328. Kirkpatric P, Baez A V *J. Opt. Soc. Am.* **38** 766 (1948)
329. Akhsakhalyan A A et al. *Centr. Eur. J. Phys.* **3** 163 (2005)
330. Pardini T et al. *Proc. SPIE* **8850** 88500E (2013)
331. Yi Sh et al. *Chinese Opt. Lett.* **12** 083401 (2014)
332. An N et al. *Proc. SPIE* **9211** 92110I (2014)
333. Brejnholt N F et al. *Proc. SPIE* **9591** 95910J (2015)
334. Verman B et al. *Adv. X-Ray Anal.* **42** 321 (2000)
335. Morawe Ch, Osterhoff M *Nucl. Instrum. Meth. Phys. Res. A* **616** 98 (2010)
336. Delaboudiniére J-P et al. *Solar Phys.* **162** 291 (1995)
337. Zhitnik I A, Kuzin S V, Slemzin V A *Poverkhnost Rentgen. Sinchrotron. Neitron. Issled.* (1) 19 (1999)
338. Martínez-Galarce D S et al. *Opt. Eng.* **52** 095102 (2013)
339. DiCicco D S et al. *Opt. Lett.* **17** 157 (1992)
340. Murakami K et al. *Appl. Opt.* **32** 7057 (1993)
341. Artioukov I A et al. *Opt. Lett.* **20** 2451 (1995)
342. Brizuela F et al. *Opt. Express* **13** 3984 (2005)
343. Stollberg H et al. *Rev. Sci. Instrum.* **77** 123101 (2006)
344. Hertz H M et al. *J. Struct. Biol.* **177** 267 (2012)
345. Zastrau U et al. *Rev. Sci. Instrum.* **89** 023703 (2018)
346. Beigman I L, Pokrovskii Yu Yu, Ragozin E N *JETP* **83** 981 (1996); *Zh. Eksp. Teor. Fiz.* **110** 1783 (1996)
347. Beigman I L, Pirozhkov A S, Ragozin E N *JETP Lett.* **74** 149 (2001); *Pis'ma Zh. Eksp. Teor. Fiz.* **74** 167 (2001)
348. Fischer D A et al. *Rev. Sci. Instrum.* **73** 1469 (2002)
349. Artyukov I A et al. *Micron* **41** 722 (2010)
350. Singh M, Braat J J M *Appl. Opt.* **39** 2189 (2000)
351. Wu B, Kumar A *Appl. Phys. Rev.* **1** 011104 (2014)
352. Lider V V *J. Surf. Invest. X-Ray Synchr. Neutron Tech.* **11** 1113 (2017); *Poverkhnost Rentgen. Sinchrotron. Neitron. Issled.* (11) 7 (2017)
353. Vernon S P et al. *Proc. SPIE* **3546** 184 (1998)
354. Khandar A, Dhez P *Proc. SPIE* **563** 158 (1985)
355. Gluskin E S et al. *Nucl. Instrum. Meth. Phys. Res. A* **246** 394 (1986)
356. Gaupp A, Mast M *Rev. Sci. Instrum.* **60** 2213 (1989)
357. Kortright J B, Underwood J H *Nucl. Instrum. Meth. Phys. Res. A* **291** 272 (1990)
358. Kortright J B et al. *Appl. Phys. Lett.* **60** 2963 (1992)
359. Yamamoto M et al. *Rev. Sci. Instrum.* **63** 1510 (1992)
360. Di Fonzo S et al. *Appl. Opt.* **33** 2624 (1994)
361. Di Fonzo S et al. *Rev. Sci. Instrum.* **66** 1513 (1995)
362. Hu W et al. *J. Synchrotron Rad.* **5** 732 (1998)
363. Grimmer H et al. *Proc. SPIE* **3773** 224 (1999)
364. Schäfers F et al. *Appl. Opt.* **38** 4074 (1999)
365. Tan M Y et al. *Opt. Express* **17** 586 (2009)
366. Imazono T et al. *Rev. Sci. Instrum.* **80** 085109 (2009)
367. MacDonald M A, Schäfers F, Gaupp A *Opt. Express* **17** 23290 (2009)
368. Wagner U H et al. *AIP Conf. Proc.* **1234** 781 (2010)
369. Cui M et al. *AIP Conf. Proc.* **1234** 641 (2010)
370. Guo Z-Y et al. *Chinese Phys. C* **37** 18001 (2013)
371. Schmidt J et al. *Opt. Express* **23** 33564 (2015)
372. Grizolli W et al. *Rev. Sci. Instrum.* **87** 025102 (2016)
373. Kortright J B, Fischer-Colbrie A *J. Appl. Phys.* **61** 1130 (1987)
374. Lee P *Appl. Opt.* **22** 1241 (1983)
375. Ragozin E N et al. *Proc. SPIE* **4782** 176 (2002)
376. Levashov V E et al. *Radiat. Phys. Chem.* **75** 1819 (2006)
377. Pirozhkov A S, Ragozin E N *Phys. Usp.* **58** 1095 (2015); *Usp. Fiz. Nauk* **185** 1203 (2015)
378. Joensen K D et al. *Appl. Opt.* **34** 7935 (1995)
379. Windt D L et al. *J. Appl. Phys.* **88** 460 (2000)
380. Yakshin A E et al. *Opt. Express* **18** 6957 (2010)
381. van Loevezijn P et al. *Appl. Opt.* **35** 3614 (1996)
382. Protopopov V V, Kalnov V A *Opt. Commun.* **158** 127 (1998)
383. Wang Z, Michette A G *J. Opt. A* **2** 452 (2000)
384. Vinogradov A V, Faschenko R M *Nucl. Instrum. Meth. Phys. Res. A* **448** 142 (2000)
385. Powell K, Tait J M, Michette A G *Proc. SPIE* **4145** 254 (2001)
386. Morawe Ch et al. *Nucl. Instrum. Meth. Phys. Res. A* **493** 189 (2002)
387. Cheng X et al. *Opt. Commun.* **265** 197 (2006)
388. Yao Y, Kunieda H, Wang Zh *Opt. Express* **21** 8638 (2013)
389. Aquila A L et al. *Opt. Express* **14** 10073 (2006)
390. Kozhevnikov I V et al. *Crystallogr. Rep.* **51** 1075 (2006); *Kristallogr.* **51** 1146 (2006)
391. Kozhevnikov I V, Yakshin A E, Bijkerk F *Opt. Express* **23** 9276 (2015)
392. Wang Z et al. *Appl. Phys. Lett.* **89** 241120 (2006)
393. Wang H et al. *Thin Solid Films* **515** 2523 (2006)
394. Wang Z et al. *J. Appl. Phys.* **99** 056108 (2006)
395. Wang Z et al. *Appl. Phys. Lett.* **90** 031901 (2007)
396. Tan M Y et al. *Nucl. Instrum. Meth. Phys. Res. A* **654** 588 (2011)
397. Morawe Ch, Peffen J-Ch, Supruangnet R *Proc. SPIE* **9207** 92070J (2014)
398. Tang X et al. *Opt. Express* **25** 22537 (2017)
399. Kapralov V G et al. *Quantum Electron.* **32** 149 (2002); *Kvantovaya Elektron.* **32** 149 (2002)
400. Beigman I L et al. *Quantum Electron.* **37** 1060 (2007); *Kvantovaya Elektron.* **37** 1060 (2007)

401. Champeaux J-Ph et al. *Nucl. Instrum. Meth. Phys. Res. A* **581** 687 (2007)
402. Vishnyakov E A, Shatokhin A N, Ragozin E N *Quantum Electron.* **45** 371 (2015); *Kvantovaya Elektron.* **45** 371 (2015)
403. Yamashita K et al. *Appl. Opt.* **37** 8067 (1998)
404. Okajima T et al. *Appl. Opt.* **41** 5417 (2002)
405. Harrison F A et al. *Astrophys. J.* **770** 103 (2013)
406. Awaki H et al. *Appl. Opt.* **53** 7664 (2014)
407. Wang F L et al., in *X-Ray Lasers 2006. Proc. of the 10th Intern. Conf., August 20 – 25, 2006, Berlin, Germany* (Springer Proc. in Physics, Vol. 115, Eds P V Nickles, K A Janulewicz) (Dordrecht: Springer, 2007) p. 555
408. Ichimaru S et al. *Rev. Sci. Instrum.* **86** 093106 (2015)
409. Pardini T et al. *Opt. Express* **24** 18642 (2016)
410. Krausz F, Ivanov M *Rev. Mod. Phys.* **81** 163 (2009)
411. Hentschel M et al. *Nature* **414** 509 (2001)
412. Krausz F, Stockman M I *Nature Photon.* **8** 205 (2014)
413. Morlens A-S et al. *Opt. Lett.* **30** 1554 (2005)
414. Beigman I L, Pirozhkov A S, Ragozin E N *J. Opt. A* **4** 433 (2002)
415. Wonisch A et al. *Appl. Opt.* **45** 4147 (2006)
416. Suman M et al. *Opt. Express* **17** 7922 (2009)
417. Hofstetter M et al. *New J. Phys.* **13** 063038 (2011)
418. Bourassin-Bouchet C et al. *New J. Phys.* **14** 023040 (2012)
419. Lin C-Y, Liu D-H *Chinese Phys. B* **21** 094216 (2012)
420. Garakhin S A et al. *Quantum Electron.* **47** 378 (2017); *Kvantovaya Elektron.* **47** 378 (2017)
421. Schultze M et al. *New J. Phys.* **9** 243 (2007)
422. Bajt S et al. *J. Opt. Soc. Am. A* **29** 216 (2012)
423. Schuster M et al. *Proc. SPIE* **3767** 183 (1999)
424. Morawe Ch et al. *Rev. Sci. Instrum.* **70** 3227 (1999)
425. Morawe Ch *AIP Conf. Proc.* **879** 764 (2007)
426. Michaelsen C et al. *Adv. X-Ray Anal.* **42** 308 (2000)
427. Akhsakhalyan A A et al. *Nucl. Instrum. Meth. Phys. Res. A* **543** 346 (2005)
428. Morawe C et al. *Proc. SPIE* **5537** 115 (2004)
429. Hignette O et al. *Rev. Sci. Instrum.* **76** 063709 (2005)
430. Morawe Ch et al. *Proc. SPIE* **6317** 63170F (2006)
431. Hignette O et al. *AIP Conf. Proc.* **879** 792 (2007)
432. Liu W et al. *J. Synchrotron Rad.* **18** 575 (2011)
433. Morawe Ch et al. *Proc. SPIE* **9588** 958803 (2015)
434. Schuster M, Gobel H *J. Phys. D* **28** A270 (1995)
435. Stömmer R et al. *Adv. X-Ray Anal.* **41** 336 (1999)
436. Holz T et al. *Adv. X-Ray Anal.* **43** 212 (2000)
437. Liu Ch et al. *J. Vac. Sci. Technol. A* **19** 1421 (2001)
438. Wang Z S et al. *Opt. Express* **14** 2533 (2006)
439. Carniglia C K, Apfel J H *J. Opt. Soc. Am.* **70** 523 (1980)
440. Hatano T, Ejima T, Tsuruba T *J. Electron. Spectrosc. Relat. Phenom.* **220** 14 (2017)
441. Yulin S A et al. *Proc. SPIE* **5645** 289 (2005)
442. Arkadiev V A et al. *Proc. SPIE* **3773** 122 (1999)
443. Menzel M et al. *Appl. Phys. A* **79** 1039 (2004)
444. Martynov V V et al. *AIP Conf. Proc.* **705** 697 (2004)
445. Lim Y C et al. *Appl. Phys. A* **72** 121 (2001)
446. Sammar A, André J-M, Pardo B *Opt. Commun.* **86** 245 (1991)
447. Erko A I et al. *Nucl. Instrum. Meth. Phys. Res. A* **333** 599 (1993)
448. Keski-Kuha R A *M Appl. Opt.* **23** 3534 (1984)
449. Jark W *Opt. Commun.* **65** 201 (1986)
450. Voronov D L et al. *Proc. SPIE* **6705** 67050E (2007)
451. van der Meer R et al. *Opt. Express* **21** 13105 (2013)
452. Voronov D L et al. *AIP Conf. Proc.* **1234** 891 (2010)
453. Yang X et al. *J. Opt. Soc. Am. B* **32** 506 (2015)
454. Chernov V A et al. *Nucl. Instrum. Meth. Phys. Res. A* **405** 310 (1998)
455. Martynov V V, Platonov Yu *Adv. X-Ray Anal.* **45** 402 (2002)
456. Berrouane H et al. *Opt. Commun.* **76** 111 (1990)
457. Sammar A et al. *J. Opt.* **24** 37 (1993)
458. Benbalagh R et al. *Nucl. Instrum. Meth. Phys. Res. A* **541** 590 (2005)
459. Ishino M et al. *Appl. Opt.* **45** 6741 (2006)
460. Störmer M et al. *J. Phys. D* **40** 4253 (2007)
461. Jonnard P, Le Guen K, André J-M *X-Ray Spectrom.* **38** 117 (2009)
462. van der Meer R et al. *Proc. SPIE* **8139** 81390Q (2011)
463. Le Guen K et al. *Eur. Phys. J. Appl. Phys.* **78** 20702 (2017)
464. André J-M et al. *Appl. Opt.* **41** 239 (2002)
465. Kozhevnikov I V et al. *Opt. Express* **18** 16234 (2010)
466. van der Meer R et al. *AIP Adv.* **3** 012103 (2013)
467. Fialin M et al. *X-Ray Spectrom.* **25** 60 (1996)
468. Yoshioka T et al. *Astron. Nachr.* **320** 384 (1999)
469. Seely J F *Proc. SPIE* **4138** 174 (2000)
470. Imazono T et al. *Appl. Opt.* **46** 7054 (2007)
471. Jonnard P et al. *X-Ray Spectrom.* **41** 308 (2012)
472. André J-M et al. *X-Ray Spectrom.* **30** 12 (2001)
473. André J-M, Jonnard P, Benbalagh R *X-Ray Spectrom.* **36** 62 (2007)
474. Rife J C et al. *Phys. Scripta* **41** 418 (1990)
475. Underwood J H et al. *Rev. Sci. Instrum.* **66** 2147 (1995)
476. Kowalski M P et al. *Opt. Lett.* **29** 2914 (2004)
477. Lin H, Li L *Appl. Opt.* **47** 6212 (2008)
478. Voronov D L et al. *Proc. SPIE* **7448** 74480J (2009)
479. Voronov D L et al. *Proc. SPIE* **7802** 780207 (2010)
480. Sae-Lao B et al. *Appl. Opt.* **41** 2394 (2002)
481. Voronov D L et al. *Opt. Lett.* **39** 3157 (2014)
482. Voronov D L et al. *Opt. Express* **23** 4771 (2015)
483. Voronov D L et al. *Appl. Phys. Lett.* **109** 043112 (2016)
484. Goray L I, Egorov A Yu *Appl. Phys. Lett.* **109** 103502 (2016)
485. Senf F et al. *Opt. Express* **24** 13220 (2016)
486. Naulleau P P et al. *Opt. Commun.* **200** 27 (2001)
487. Maystre D, Petit R *Nouvelle Revue d'Optique* **7** 165 (1976)
488. Yang X et al. *Opt. Express* **24** 15079 (2016)
489. Lin H et al. *Opt. Lett.* **33** 485 (2008)
490. Warwick T et al. *AIP Conf. Proc.* **1234** 776 (2010)
491. Yang X et al. *J. Synchrotron Rad.* **24** 168 (2017)
492. Prasciolu M et al. *Opt. Express* **23** 15195 (2015)
493. Levashov V E et al. *Opt. Commun.* **109** 1 (1994)
494. Fechtchenko R M, Vinogradov A V, Voronov D L *Opt. Commun.* **210** 179 (2002)
495. Levashov V E, Vinogradov A V *Appl. Opt.* **32** 1130 (1993)
496. Voronov D L et al. *Proc. SPIE* **7077** 707708 (2008)
497. Cruddace R G et al. *Phys. Scripta* **41** 396 (1990)
498. Lixiang Y et al. *Phys. Scripta* **51** 680 (1995)
499. Kleineberg U et al. *J. Electron Spectrosc. Related Phenom.* **80** 389 (1996)
500. Seely J F et al. *Appl. Opt.* **36** 8206 (1997)
501. Hellwege K-H *Z. Phys.* **106** 588 (1937)
502. Polack F et al. *AIP Conf. Proc.* **879** 489 (2007)
503. Choueikani F et al. *Opt. Lett.* **39** 2141 (2014)
504. Yang X et al. *Opt. Express* **25** 15988 (2017)
505. Choueikani F et al. *J. Phys. Conf. Ser.* **425** 152007 (2013)
506. Lagarde B et al. *J. Phys. Conf. Ser.* **425** 152012 (2013)
507. Trost M et al. *Opt. Express* **21** 27852 (2013)
508. Medvedev V V et al. *Opt. Express* **21** 16964 (2013)
509. Pradhan P C et al. *Proc. SPIE* **10386** 1038605 (2017)
510. van den Boogaard A J R et al. *Opt. Lett.* **37** 160 (2012)
511. Kriese M et al. *Proc. SPIE* **9048** 90483C (2014)
512. Liddle J A et al. *J. Vac. Sci. Technol. B* **21** 2980 (2003)
513. van den Boogaard A J R et al. *Proc. SPIE* **7271** 72713B (2009)
514. Huang Q et al. *Opt. Lett.* **39** 1185 (2014)
515. Kang H C et al. *Appl. Phys. Lett.* **86** 151109 (2005)
516. Huang Q et al. *Chinese Opt. Lett.* **10** 090501(2012)
517. Lynch S K, Liu C, Assoufid L *Proc. SPIE* **8076** 80760F (2011)
518. Lynch S K et al. *J. Micromech. Microeng.* **22** 105007 (2012)
519. Bonse U, Hart M *Appl. Phys. Lett.* **6** 155 (1965)
520. Wen H et al. *Nature Commun.* **4** 2659 (2013)
521. Wen H et al. *Philos. Trans. R. Soc. A* **372** 20130028 (2014)
522. Momose A et al. *Jpn. J. Appl. Phys.* **42** L866 (2003)
523. Weitkamp T et al. *Opt. Express* **13** 6296 (2005)
524. Kim J M et al. *Opt. Express* **18** 24975 (2010)
525. Kirz J *J. Opt. Soc. Am.* **64** 301 (1974)
526. Bionta R M, Skulina K M, Weinberg J *Appl. Phys. Lett.* **64** 945 (1994)
527. Koyama T et al. *Rev. Sci. Instrum.* **83** 013705 (2012)
528. Sanli U T et al. *Proc. SPIE* **9592** 95920F (2015)
529. Mayer M et al. *Ultramicroscopy* **111** 1706 (2011)
530. Yan H et al. *J. Phys. D* **47** 263001 (2014)
531. Liese T et al. *Appl. Surf. Sci.* **257** 5138 (2011)
532. Braun S et al. *J. Phys. Conf. Ser.* **425** 052019 (2013)
533. Niese S et al. *Opt. Express* **22** 20008 (2014)
534. Yan H et al. *Sci. Rep.* **3** 1307 (2013)
535. Nazaretski E et al. *Rev. Sci. Instrum.* **84** 033701 (2013)

536. Kubec A et al. *J. Synchrotron Rad.* **21** 1122 (2014)
537. Yan H et al. *Phys. Rev. B* **76** 115438 (2007)
538. Huang X et al. *Sci. Rep.* **3** 3562 (2013)
539. Kang H C et al. *Phys. Rev. Lett.* **96** 127401 (2006)
540. Conley R et al. *Rev. Sci. Instrum.* **79** 053104 (2008)
541. Morgan A J et al. *Sci. Rep.* **5** 9892 (2015)
542. Kubec A et al. *J. Synchrotron Rad.* **24** 413 (2017)
543. Koyama T et al. *AIP Conf. Proc.* **1365** 24 (2011)
544. Huang X et al. *Opt. Express* **23** 12496 (2015)
545. Werner S et al. *Nano Res.* **7** 528 (2014)
546. Bajt S et al. *Light Sci. Appl.* **7** 17162 (2017)
547. Eriksson M, van der Veen J F, Quitmann C *J. Synchrotron Rad.* **21** 837 (2014)
548. Weckert E *IUCrJ* **2** 230 (2015)
549. Couprie M E *J. Electron Spectrosc. Relat. Phenom.* **196** 3 (2014)
550. Ament L J P et al. *Rev. Mod. Phys.* **83** 705 (2011)
551. Ade H, Stoll H *Nature Mater.* **8** 281 (2009)
552. Barty A, Küpper J, Chapman H N *Annu. Rev. Phys. Chem.* **64** 415 (2013)
553. Brif C, Chakrabarti R, Rabitz H *New J. Phys.* **12** 075008 (2010)
554. Bayraktar M et al. *J. Phys. D* **45** 494001 (2012)
555. Bayraktar M et al. *Opt. Express* **22** 30623 (2014)
556. Brejnholt N F et al. *Proc. SPIE* **9144** 914419 (2014)